The Application of Superacidic Materials for the Oxidation of Methane

A thesis submitted in partial fulfilment for the requirements of the Nottingham Trent University for the degree of Doctor of Philosophy

February 2000

Adrian St.Clair Brown

Abstract

In recent years so called "superacidic" metal oxides have attracted a lot of attention, primarily because of their ability to catalyse hydrocarbon isomerisation reactions at low temperatures. In this study, two particular classes of "superacidic" metal oxides-sulfated haematite and molybdated zirconia, have been examined for their efficacy in methane oxidation. To date, there have been few studies, which have aimed at investigating the potential of this class of oxides for hydrocarbon oxidation reactions, which is surprising in view of their well known ability to activate paraffins.

Sulfation has been employed for iron oxide catalysts prepared from a number of oxyhydroxide and hydroxide precursors. Although, as has been shown, iron oxide catalysts prepared by different routes exhibit different reaction pathways during methane oxidation, sulfation has been found to produce a number of general effects such as increased surface area, suppression of low temperature total oxidation and the enhancement of oxidation activity at higher temperatures producing low levels of selective partial oxidation products. TEM examination demonstrates that the morphology of the different iron oxide samples are related to that of their precursors and is little effected by sulfation, except in the case of iron oxide samples prepared from a goethite precursor where the influence of sulfation on porosity is evidenced. Powder x-ray diffraction indicates that all the materials are in the haematite polymorph following calcination and that the sulfation again produces little effect, except for modifying the particle size and crystallinity in some cases. However, in the case of haematite produced from goethite, sulfation causes an anisotropic effect on the width of powder diffraction reflections. Further investigation has demonstrated that this is highly calcination temperature dependent, and whilst Mossbauer spectroscopy indicates that cationic disorder contributes to this effect HRTEM has shown it to be primarily due to the presence of mesoporous dimension voids running axially along the acicular Fe_2O_3 crystallites. It is proposed that sulfation causes this effect by hindering the Fe^{3+} cation migration during the transformation of goethite to haematite and this is associated with bridging C_{2v} complexation of SO_4^{2-} as evidenced in the sulfated goethite precursor.

The catalytic activity of a series of zirconia-supported molybdenum catalysts with different loadings in the range 2, 5 and 10wt% were evaluated for both the partial and complete oxidation of methane. The catalytic performance of these materials has been shown to depend markedly on molybdenum content and it has tentatively been suggested that the formation of a monolayer species over the zirconia support is of importance in the reaction. Molybdation increases surface area and quantitative powder X-ray diffraction has indicated that this is associated with an increasing proportion of the metastable tetragonal phase of zirconia with increasing MoO_3 content. Hydrogen TPR studies indicate that molybdate undergoes a two stage reduction process and that Mo species on monoclinic zirconia are more susceptible to reduction. Laser Raman spectroscopy studies have indicated that the nature of the molybdenum oxo species is a function of loading, with polymolybdate species being replaced by XRD invisible molybdenum trioxide crystallites as MoO_3 content is increased. No direct relationship between MoO_3 formation or ZrO_2 polymorph on catalytic performance could be discerned and it is proposed that at reaction temperatures, which are significantly above the Tamman temperature of MoO_3 molybdenum oxospecies are highly mobile forming monolayer type entities. Consistent with this, a catalyst with close monolayer MoO_3 content is found to possess a much higher efficacy than catalysts with sub- and super- monolayer contents.

Finally, "superacidic" metal oxides have been screened for efficacy in methane combustion and the results determined under differential reaction conditions have been compared with those of materials reported to have high efficacy in the literature. It is found that, consistent with their potential enhancement of methane activation, modification of catalysts by literature methods so as to introduce "superacidity" generally promotes methane oxidation performance. However, supporting low levels of platinum on "Superacidic" oxides generally suppresses their performance, which is the opposite effect to that observed on their base oxides, which may imply a direct interaction of platinum with the active sites of reaction.

Acknowledgements

I wish to gratefully acknowledge the following for their efforts and contributions, Bas Rijniersce, and Adam Baker (two final year undergraduate students) also Prof. C.Kiely and Dr M.Edwards (University of Liverpool) for their excellent microscopy which combined with the Mossbauer spectroscopy kindly performed by Dr. Q.A Pankhurst (University College London) enabled the comprehensive characterisation of the goethite and goethite derived iron oxide materials. Many thanks also to Dr. S. Taylor (University of Wales at Cardiff) for Raman spectroscopy. Warmest gratitude's also for Drs. M.Crapper and D.Williams (University of Loughborough) for allowing me to use their x-ray diffractometer on more than one occasion, and Mr.D Lacey (Nottingham Trent University) for transmission electron microscopy.

I would also like to thank Dr. M.Stockenhuber (Nottingham Trent University) and Prof. R.W.Joyner (Nottingham Trent University) for their useful discussions. Lastly, I would like to thank Dr. J.S.J. Hargreaves (PhD supervisor, Nottingham Trent University), for his friendship and guidance throughout.

I would also like to thank my friends particularly Ana, Ellis, Gary and Reena for their help and support, and my family my father Valentine Brown my sister Marcia Brown and her partner Paul Hamilton and baby Ayisha.

This thesis is dedicated to Theresa Majorie Brown
Wife and Mother
1949-1991

The effect of sulfation on the activity of iron oxides catalysts for methane oxidation
A.S.C. Brown, J.S.J. Hargreaves and B. Rijniersce
To appear in Topics in Catalysis

A structural study of haematite samples prepared from sulfated goethite precursors-the generation of axial mesoporous voids
A.S.J. Baker, A.S.C. Brown, M.A. Edwards, J.S.J. Hargreaves, C.J. Kiely
A. Meagher and Q.A. Pankhurst
Journal of Materials Chemistry 10 (761-766) 2000.

The application of "superacidic" metal oxides and their platinum doped counterparts to methane combustion
A.S.C. Brown, J.S.J. Hargreaves and S.H.Taylor
Catalysis Today 59 3-4 (403-409) 2000

Observations of nanoporous haematite derived from the thermal decomposition of sulfated goethite
A.S.J. Baker, A.S.C. Brown, M.A. Edwards J.S.J. Hargreaves and C.J. Kiely
Institute of Physics Conference Series 161 (549-552) 1999.

A study of superacidic MoO_3/ZrO_2 catalysts for methane oxidation
A.S.C. Brown, J.S.J. Hargreaves and S.H. Taylor
Catalysis Letters 57 (109-113) 1999.

Sulfated metal oxide catalysts-superactivity through superacidity ?
A.S.C. Brown and J.S.J. Hargreaves
Green Chemistry 1 (17-20) 1999.

A study of structural and catalytic effects of sulfation on iron oxide catalysts prepared from goethite and ferrihydrite precursors for methane oxidation
A.S.C. Brown, J.S.J. Hargreaves and B.Rijniersce
Catalysis Letters 53 (7-13) 1998.

A study of the effect of sulfation on iron oxide catalysts for methane oxidation
A.S.C. Brown, J.S.J. Hargreaves and B.Rijniersce
Catalysis Today 45 (47-54) 1998.

1.0: SUPERACIDS

1.1: General Introduction

In 1968 Gillespie[1,2] defined superacidity as any liquid which had a Hammett acidity function less than 100% sulfuric acid i.e. $H_o \leq -12$. Traditionally, the term superacid was applied to liquid media such as "Magic Acid", discovered by Olah and co-workers[3], in the 1960's. Olah's discovery of "Magic Acid", formed between fluorosulfonic acid and antimony pentaflouride, led to numerous discoveries of carbocation intermediates, which are stable in superacidic media. The stability of carbocation intermediates in superacidic liquid media enabled their identification by nuclear magnetic resonance spectroscopy (NMR), and led to the discovery of the classical trivalent carbenium ion and non-classical penta- and higher coordinated carbocations. In recognition for his work, Olah was awarded the Nobel Prize for chemistry in 1994. To date "Magic Acid", 90% antimony pentaflouride (SbF_5) and 10% flourosulfonic acid (HSO_3F), still remains the strongest superacidic medium known with $H_o \leq -26.5$[3]. The value of the Hammett acidity function, for "Magic Acid" varies depending upon the ratio between the two reagents due to the complex equilibrium, which has been well studied using Raman and NMR spectroscopies. However, the acidity is generally considered to be due to the formation of the $H_2SO_3F^+$ ion. Numerous superacidic media have been developed with the general principle of combining a strong Lewis or Bronsted acid with an already strongly acidic medium, e.g. concentrated sulfuric acid or hydrogen fluoride, thus increasing the ionisation ability.

E.g.:

$$HA + HB \longrightarrow H_2A^+ + B^-$$

Where HA=strong Bronsted acid medium, HB= strong Lewis acid/Bronsted acid, H_2A^+ = protonated Bronsted acid medium, B^- = Lewis/Bronsted anion

1.2: Sulfated metal oxides

In 1979 Arata and co-workers demonstrated the addition of small amounts of sulfate from either ammonium sulfate or sulfuric acid to the precursors of a range of metal oxides, promoted the catalytic activity of a series of strongly acid catalysed reactions under mild reaction conditions[4]. Previously in 1962 Holm and Bailey[5], found that

platinum containing sulfated zirconia exhibited superior catalytic performance for the alkylation and isomerisation of hydrocarbons, compared to commercial platinum chloride catalyst. However, it was the more recent work by Arata studying a range of sulfated metal oxides (SMO) coupled with more stringent environmental considerations, which stimulated further research interest in these types of materials. Arata and co-workers measured the acid strength of Zr, Hf, Fe, Sn, Ti and Al SMO using weak self indicating bases, e.g. trinitrotoluene (pK_a = -16.04), called Hammett indicators, discussed further in section 1.2.2.1[6,7]. They found that the addition of sulfate to the amorphous hydroxides produced Hammett values less than or equal to $H_o \leq -12$, with the exception of sulfated aluminium oxide, (SAl), where sulfation of the crystalline oxide, as opposed to the hydroxide, generated strong acidity. This then led the authors to describe these types of SMO systems as "superacids". Therefore the term superacid, now has a wider implication and is not confined just to liquid media but also to solid heterogeneous materials. In the field of catalysis, there are numerous solid acids, e.g. zeolites and heteropoly acids. However, it is still debated whether or not SMO are superacids or simply solid acids of comparable acidity to traditional solid acids.

During the 1990's many articles on SMO materials have appeared both in the open and patent literature[6-10]. This is due to the potential of these materials to replace environmentally unfriendly acid catalysts, e.g. $AlCl_3$, HF, and H_2SO_4 and also, as a result of their apparent strong acidity, their potential use in a range of acid catalysed reactions where milder conditions may be employed[11]. A great deal of the literature pertaining to SMO centres around sulfated zirconia and this system has been extensively studied[12]. In the following sections of this introduction an overview of the current status of sulfated materials is given in terms of their preparation, acid characteristics and some novel applications of solid superacids.

1.2.1: Preparation

The early work of Arata et al. on the preparation of SMO showed several important features.

1. Sulfation can be performed using a wide range of sulfur containing reagents such H_2SO_4, $(NH_4)_2SO_4$, H_2S, SO_2, SO_3 and $SOCl_2$.

2. With the exception of aluminium oxide, sulfation must be performed on the amorphous hydroxide/oxyhydroxide to produce strong acidity.
3. Sulfate is still present even at calcination temperatures as high as ca. 650C.
4. The addition of sulfate stabilises the resultant surface area of the metal oxide.

In general there are two different methods for the preparation of SMO, a one-step and a two-step method. The two step method is the most common method of preparation and in general requires the formation of the metal hydroxide by precipitation at a suitable pH, followed by drying ca.100C for a period of time before sulfation. The sulfation process as given by Arata et al. involved placing the dried hydroxide onto filter paper and then adding either sulfuric acid or ammonium sulfate solution. Recent procedures simply immerse the dried hydroxide powder in the sulfating solution. After sulfation, the sulfate is once again dried and then calcined either in- or ex-situ. The following factors have all been shown to affect the final properties and hence activity of the final product.

1:Precursors		**Ref.**
Zirconia:	$ZrOCl$, $ZrCl_4$, $ZrO(NO_3)_2$	4,13-17
Titania:	Ti (IV)(isopropoxide), $TiCl_4$	18
Iron oxide:	$Fe_2(SO_4)_3$, $FeCl_3$, $Fe(NO_3)_3 \cdot 9H_2O$	4
Tin oxide	$SnCl_4 \cdot xH_2O$	19,20

2: Precipitating reagents		
NH_3 (most common)		21
H_2O		22

3: Final pH		
Zirconia:	pH 7-10	23-25
Tin oxide:	pH 7, 10	19,20

3: **Final pH cont.**		**Ref.**
Iron oxide:	pH 7-9	7,26
Titania	pH 8-9	11,27

4: **Sulfating reagents**	
Sulfuric acid	
Ammonium sulfate	28
Sulfur dioxide	22
Sufuryl chloride	29
Hydrogen sulfide	16
Carbon disulfide	30

With only one exception, the generation of superacidity was derived from amorphous precursors. However, a wide range of starting precursors has been used as outlined above. The use of chloride containing precursors or reagents may be discouraged since residual chloride ions, which can be difficult to remove during preparation, may affect the adsorption of sulfate ions during the sulfation process. Further residual chloride ions may actually take part in the reaction, thus generating misleading catalytic results. In general the most common precipitating reagent is ammonia solution. The addition rate of base, as well as the reagent type has also been demonstrated to affect the final product[21]. The final pH of the solution is reported to have a significant effect on crystallite size as well as on catalytic activity. Wang et al[20] and Arata et al[27] prepared similarly sulfated tin oxide, (SSn), at pH 8-9 and at pH 10 respectively. Their measured Hammett acidity values were $H_o \leq -8.2$ and $H_o \leq -16.04$, indicating the effect of pH on acid strength. However, both materials were active for the isomerisation of cyclopropane and the isomerisation of pentane respectively[19,20]. It was also noted by several authors, either by direct activity testing or by characterisation methods, that using ammonium sulfate for sulfation led to a less active material in comparison to using sulfuric acid[6]. However the reproducibility of catalytic data appeared better with ammonium sulfate than with sulfuric acid for the dehydration of 1-propanol[6]. Alternative sulfating reagents have

been investigated, as shown above, and it is generally believed that the sulfur is converted to sulfate (SO_4^{2-}), where low temperature, ca. 300C, calcination in air or oxygen is usually sufficient for the conversion into sulfate[6].

The calcination temperature for optimum activity is a function of the above preparation variables and is not necessarily the same for all SMO. Calcination temperatures in the range 400-600C are reported in the literature. Arata et al. noted that a calcination temperature of ca. 550C in air for 2-3 hours was sufficient for optimum catalytic activity for sulfated iron oxide. Sulfate decomposes above ca.600C, therefore above this temperature, sulfate begins to decompose and the sulfate content decreases as a function of temperature. However, at high calcination temperatures above ca.650C, a small percentage of sulfate may still be retained[23]. Sulfate content may therefore be reduced during a reaction, but also under net reducing conditions sulfate may be reduced to sulfur oxides or to elemental sulfur[11]. Arata et al. also noted the importance of preventing moisture from adsorbing onto the surface. In several studies samples were stored in sealed ampules prior to calcination and/or activity testing to prevent the adsorption of moisture.

The one step method has evolved from sol-gel technology, and affords good control over physiochemical properties such as surface area and porosity as well as requiring fewer reagents. Generally, this method involves the simultaneous production of the amorphous precursor with the sulfating reagent present in the solution or alternatively the decomposition of a sulfate containing metal such as iron sulfate. Indeed, Arata et al first used this route in developing SMO materials[6].

1.2.2: Strength and number of acid sites

In order to evaluate the acid nature of SMO materials, a wide variety of test reactions and characterisation techniques are reported in the literature[31,32]. The first and most common technique, which was used not only to determine the acid strength but also it was hoped, to provide a common scale to rank the materials, was the use of Hammett indicators. This technique, as discussed later, has been criticised by several research groups in terms of both the experimental procedure and the underlying theory. Hence, alternative methods based on those used for characterising other solid acid materials, i.e. zeolites, have since been used as well as characteristic acid catalysed test reactions.

1.2.2.1: Hammett acidity functions

In 1932 Hammett and Deyrup developed a method for measuring the acidity of concentrated acidic media[33]. They studied various mixtures of sulfuric acid and water for their ability to protonate primary anilines, weak bases used as acid-base indicators. These indicators were known as Hammett acidity Indicators. In 1957 Bensi used these indicators to determine the acid strength and acid site number of heterogeneous surfaces using butylamine[34].

Table 1: Basic indicators used for the measurement of acid strength[35]

Indicators	Colour		pK_a	Equivalent (H_2SO_4) %
	Base Form	Acid Form		
Neutral red	Yellow	Red	+6.8	$8x10^{-8}$
Methyl red	Yellow	Red	+4.8	
Phenylazonaphthylamine	Yellow	Red	+4.0	$5x10^{-5}$
p-(dimethylamino)azobenzene	Yellow	Red	+3.3	$3x10^{-4}$
2-amino-5-azotoluene	Yellow	Red	+2.0	$5x10^{-3}$
Benzeneazodiphenylamine	Yellow	Purple	+1.5	$2x10^{-2}$
Crystal violet	Blue	Yellow	+0.8	0.1
p-nitrobenzeeneazo(p-nitrodiphenylamine)	Orange	Purple	+0.43	
Dicinnamalacetone	Colourless	Red	-3.0	48
Benzalacetophenone	Colourless	Yellow	-5.6	71
Anthraquinone	Colourless	Yellow	-8.2	90
2,4,6-tritroaniline	Colourless	Yellow	-10.10	
p-nitrotoluene	Colourless	Yellow	-11.35	
m-nitrotoluene	Colourless	Yellow	-11.99	
p-nitrofluorobenzene	Colourless	Yellow	-12.44	
m-nitrochlorobenzene	Colourless	Yellow	-13.16	100
2,4-dinitrotoluene	Colourless	Yellow	-13.75	
2,4-dinitroflurobenzene	Colourless	Yellow	-14.52	
1,3,5-trinitrotoluene	Colourless	Yellow	-16.04	

The acid strength of a solid surface is determined by its ability to protonate an adsorbed base to produce the conjugate acid form. By using the Hammett bases it is possible to observe the formation of the conjugate acid by a colour change, see Table 1. Each base has an associated pK_a value. Therefore the pKa value for the solid acid

lies between two successive bases in the series, as given in Table 1, one which displays the colour change due to protonation and the other which the solid acid is unable to protonate, and therefore no colour change is observed.

In practice a series of Hammett indicators are diluted in a suitable inert organic solvent e.g. benzene, sulfuryl chloride or cyclohexane, and added to separate samples of the dried solid acid. The resulting colour change is observed and the approximate Hammett acidity value determined. Experimental variables such as titration time, volume of indicator added, pore size and moisture should be carefully controlled[35]. Using this method Hammett values for SMO such as sulfated zirconia (SZ), sulfated titania (STi), and sulfated tin oxide (SSn) have been reported as $H_o \leq -16$[36], -14.5[6], and –16.04[19] respectively.

Several criticisms of this method have emerged from the literature, and these may be summarised below:

1. The formation of the conjugate acid is associated with a colour change. This is difficult to observe with coloured samples.
2. Equilibrium between the base and the solid sample must be established and this may take along time.
3. There are potential interactions between the solvent molecules or the adsorbate, which can generate misleading results[37].
4. The inherent heterogeneity of metal oxides means that there is a distribution of acid strengths (Lewis and Bronsted).

The problems outlined above, limit the use of this technique for measuring acid strength. In attempts to alleviate some of the problems involved in this technique bases other than Hammett bases have been employed with spectroscopic techniques.

1.2.2.2: *Ultraviolet-Visible spectroscopy*

Hall et al. developed an ultraviolet-visible (UV-Vis), spectophotometric method to measure the acidity of some solid acids[38]. Hammett indicators were used to calibrate the acidity of a series of solid acids to those of sulfuric acid solutions having the same H_o values. These authors pointed out that due to the red shifts of bands of

unprotonated indicators, the visual observation of a yellow colour on adsorption can be misleading, and the spectroscopic determination of peak maxima is essential for the correct estimation of acid strength using adsorbed Hammett indicators. Their data showed that SZ has an acid strength about equivalent to 100% sulfuric acid H_o= -12. This was the first indication in the literature that sulfated zirconia is not a superacid. The strongest acidic zeolite, HM, was found to be a mild superacid H_o= -12.4. For the catalysts tested other than SZ the order of their strengths obtained from the spectrophotometric measurements correlated well with their relative activities and selectivities for n-butane conversion, but catalytic data for SZ were not presented by Hall et al[38]. Using the same test reaction, Frenkel reported that the acidity of SZ is much higher than any of the solid acids reported in the above study and corresponds to $H_o \leq$ -17, in agreement with the value obtained from direct Hammett indicator measurements[12], indicating that SZ is indeed a solid superacid.

1.2.2.3*: Infrared spectroscopy.*

The use of probe molecules, such as ammonia and pyridine with infrared spectroscopy to investigate both acid strength and acid number is now well established, particularly on zeolitic type catalysts[39-42]. Consequently, ammonia and pyridine, adsorption infrared spectroscopy has been applied by several authors on SMO materials. Jin et al. studied a range of ammonium sulfate treated (AS) metal oxides samples, Zr, Ti, Fe, Al, Sn, Si and Bi for the isomerisation of cylcopropane[18]. All materials except AS/Si and AS/Bi displayed activity for the reaction at 150C. Ammonia and pyridine adsorption spectroscopy was used to determine the number of accessible acid sites. Table 2 shows the results obtained by the authors. The authors reported that although there was a rough correlation between acid site number and surface area there was no correlation between these values and those of catalytic activity.

It may be envisaged that acid site density may play a role in determining the order of catalytic activity between the samples. Based on the amount of pyridine and ammonia adsorbed, the acid site density, i.e. the amount of gas adsorbed divided by the surface area of the sample, is in the range 0-2.7 $\mu molm^{-2}$ and 0.6-2.8 $\mu mol\ m^{-2}$ respectively. The order of acid site density generally decreases with decreasing rate of reaction. However, for tin and bismuth, acid site densities based on the amount of

ammonia gas adsorbed are similar to that of AS/Zr while their reaction rates are much lower. Similarly, AS/Ti has a much higher acid site density but a slightly lower reaction rate value than AS/Zr. Therefore acid site density also does not correlate with catalytic activity. Further, it is interesting to note that by dividing the reaction rate by the surface area to obtain a specific activity for the samples, AS/Fe displays the highest value.

Table 2: Reaction and gas adsorption data on a range of ammonium sulfated metal oxides[18]

Oxide sample	Reaction rate μmol min^{-1} g^{-1}	Surface area m^2 g^{-1}	Gas adsorbed mmol g^{-1}		Acid site density μmol m^{-2}		Specific activity μmol min^{-1} m^{-2}
			PY	Am	PY	Am	
AS/Zr	243	120	0.21	0.26	1.8	2.2	2.03
AS/Ti	226	60	0.16	0.17	2.7	2.8	3.77
AS/Fe	202	40	0.06	0.07	1.5	1.8	5.05
AS/Al	69	230	0.26	0.36	1.1	1.6	0.30
AS/Sn	49	80	0.10	0.18	1.3	2.3	0.61
AS/Si	0	250	0.02	0.14	0.1	0.6	-
AS/Bi	0	4	0.00	0.01	0.0	2.5	-

PY= pyridine, Am= ammonia gas and AS = ammonium sulfated.

However, the acid site density for this sample is intermediate between all the samples investigated. Therefore, as the authors concluded, the acid strength must play a role in determining the order of activity between the samples examined. Infrared pyridine absorption studies by Lee et al on sulfated iron oxide (SFe), also observed shifts in the S=O bond as had been reported by Jin et al[43]. However two models for pyridine absorption were given, one in accordance with Jin et al and the other a high temperature model, where pyridine interacts with sulfate directly. This may explain the shoulder on the infrared spectra by Jin et al since the difference in wavenumber observed by Lee et al ca. 45cm^{-1} is similar to that observed in the work by Jin et al.[18]. Further and more significantly, Lee and co-workers also observed the

simultaneous decomposition of the sulfate group and pyridine on adsorption of the base molecule, which is discussed further in section 1.2.2.6.

Several authors have observed only Lewis acid sites on SMO, which are believed by some authors to be responsible for the enhanced catalytic performance[18]. Kustov et al observed both Lewis and Bronsted acid sites on SZ samples using benzene adsorption with infrared spectroscopy[44]. These authors assigned two types of Bronsted sites due to bridging and terminal hydroxyl groups. On absorption of benzene the bands were shifted by ca. 200cm^{-1} to lower wavenumbers. In comparison with the shifts experienced by acidic zeolites e.g. H-ZSM-5, the SZ samples were lower. As a result, the authors concluded SZ was not a superacid, but a strong solid acid of comparable acid strength to that of zeolites. Lee and co-workers mentioned that exposure of the SFe to moist air generated Bronsted acid sites observable in the infrared spectrum[45]. Further, the authors noted that exposure of the SMO materials to atmosphere also effected the performance of the material, and suggested that the SMO should be stored in sealed ampules.

The findings of Kustov et al found agreement with several research groups for example, Adeeva et al[46] and Bensitel et al[22], both of which compared the acidity of SZ with zeolites using adsorption infrared spectroscopy. Further Sachtler et al. investigated Lewis acid sites on SZ and sulfated iron manganese sulfated zirconia (FeMnSZ), using CO adsorption infrared spectroscopy[47]. The authors found the same band at 2200 cm^{-1} in all cases and therefore proposed that these materials were strongly acidic but were not superacidic. In fact Adeeva et al compared the CO shift for SZ and FeMnSZ with γ-alumina which gave rise to stretching frequencies in the range 2215-2220 cm^{-1} implying strong, but not superacidic, Lewis acidity[47].

Recent findings by both Trung et al and Farcasiu et al observed a dependence of Lewis and Bronsted sites with calcination temperature[48,49]. Pyridine adsorption infrared studies by the former authors evidenced a decrease in the intensity of the pyridine adsorption band relating to Bronsted acidity ca.1540 cm^{-1}, while that of Lewis acidity 1477 cm^{-1} increased at temperatures between 500-550C[49]. At higher temperatures the Bronsted band remained constant while the band corresponding to Lewis acidity continued to increase up to temperatures ca. 600-700C. Therefore the following observations may be made in evaluating the use of infrared spectroscopy using probe molecules to evaluate acid strength. Water may absorb onto Lewis acid

sites pre-experimentation and modify the strong Lewis sites to weaker Bronsted sites. The shifting of infrared bands of strong acid sites may be effected or masked by the presence of other bands. Further, the available surface area as well as the number and strength of acidic sites limit the absorption of probe molecules. This is a particular problem for highly coloured materials e.g. sulfated iron oxides, where high dilutions with KBr are required (ratio of Fe: KBr, 1:200), reducing still further the available surface area for gas adsorption.

1.2.2.4:*Test reactions*

Sulfated metal oxides (SMO), because of their apparent strong acidity, have been applied to a wide range of proposed acid catalysed reactions, in an attempt to correlate catalytic activity with acidity. By far the most well documented reaction is the isomerisation of n-butane (n-C_4) to iso-butane (i-C_4). This reaction is of interest since the increase in branched hydrocarbons leads to a higher octane number, as well as providing useful intermediates for further synthesis. It is well established that SMO are able to catalyse this reaction under mild reaction conditions[31,50,51]. Indeed the use of low temperatures, as low as room temperature, offers a thermodynamic advantage since isomerisation reactions become more favourable at low temperatures.

The isomerisation of n-butane over SMO can be characterised by an induction period, an increase in activity followed by a rapid deactivation. Gao et al. studied the effect of calcination and reaction temperature over sulfated zirconia, for n-C_4 and n-C_5 isomerisation[52]. The optimum calcination temperature was found to be 650C, which is consistent with findings by other authors[23]. Selectivities towards i-C_4 were in the range 90-100% with the highest conversion at 56% of n-C_4 after 240 hours on stream at a reaction temperature of 20C. Increasing the calcination temperature above 650C resulted in a decrease in i-C_4 product and an increase in C_3 and i-C_5 products, probably due to a reduction in sulfate content. Increasing the reaction temperature above 20C led to an increase in the overall conversion of n-C_4, however above the theoretical equilibrium value of ca.70% butane conversion, the selectivity towards i-C_4 decreased below 90% and a greater amount of C_3 and i-C_5 products were observed. Hammett acidity measurements determined for sulfated zirconia

calcined at 650C produced the highest value $H_o \leq -16.0$. Kinetic data were found to correlate well with the Hammett acidity measured values, Figure 1.

However, from the work by Gao et al it is difficult to distinguish between acid strength and acid site number, since no adsorption experiments were performed. Acidic zeolites HM, HSY and HZSM-5, were found to be less active for n-C_4 isomerisation than SZ at reaction temperatures in the range 20-35C.

Figure 1: Correlation of catalytic activity for n-butane isomerisation over sulfated zirconia with kinetic and Hammett acidity values[50]

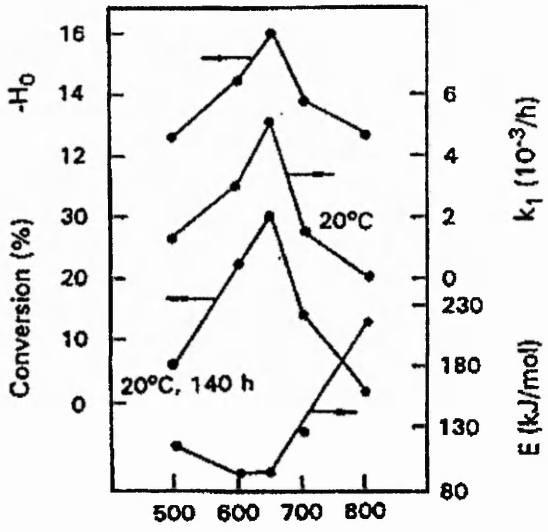

However, both sulfated zirconia and the zeolites were able to activate pentane at a reaction temperature of 75C. This led the authors to conclude that sulfated zirconia is a superacidic material and contained acidic sites stronger than those present in the zeolite samples. It is interesting to note that the work by Gao et al did not show any deactivation over a 240 hour period. However, the catalytic behaviour of sulfated zirconia is strongly dependent upon the method of preparation[52]. Limited catalyst lifetime of SMO materials for n-butane isomerisation has been reported to be due to several effects, such as coking and loss of sulfur. Several attempts to resolve this problem have centred around the introduction of hydrogen in the reaction mixture, the addition of noble metals Pt and Pd and the incorporation of transition metals. Jatia et al tested the FeMnSZ material developed by Hsu et al[31], for n-C_4

isomerisation, using a fixed bed reactor at 35C. The authors found that the addition of either Fe *or* Mn in the form of their nitrate salts promoted the reaction, while the unprommoted sulfated zirconia sample was inactive. However, impregnation of sulfated zirconia with Fe *and* Mn further increased the activity of the material with n-C_4 conversion at 8.5% after 1.5 hours, which was then followed by rapid deactivation to 2% n-C_4 conversion after 6 hours time on stream. Interestingly a doubly sulfated FeMnSZ sample denoted FeMnSSZ displayed only a slight increase in activity with an 11.5% n-C_4 conversion after 1.5 hours, followed by rapid deactivation. This material on regeneration in air was restored to 70% of its original activity[31].

Figure 2: Mechanistic routes for n-butane isomerisation[188]

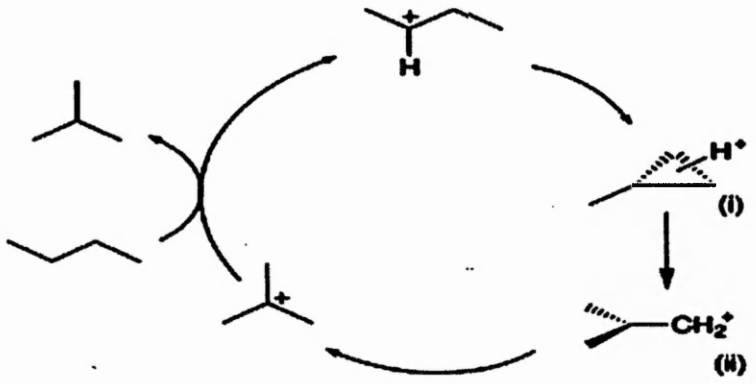

Scheme 1 Intramolecular butane isomerisation mechanism.

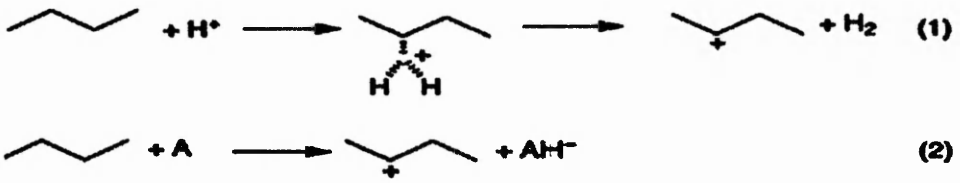

Scheme 2 Acidic activation routes of butane.

Arata et al. studied the addition of Pt, Ir, Rh, Ru, Os and Pd to sulfated zirconia using a fixed bed pulse reactor for n-C_4 isomerisation. The results from these authors showed that the addition of metals enhanced the activity of sulfated zirconia, with activity occurring below 130C under their conditions, above which point, sulfated

zirconia itself becomes active. However, the reaction temperature employed in this study is much higher than the temperatures reported generally in the literature. The best sample examined, sulfated zirconia doped with platinum (PtSZ), was assumed on the basis of the activity differences between PtSZ and SZ to have a Hammett acidity function value of $H_o \leq -20.5$. This value seems unlikely since it would make PtSZ as acidic as "Magic Acid".

Cohelo et al studied FeMnSZ and sulfated zirconia doped with nickel (NSZ), for n-butane isomerisation using a flow reactor at 100 and 250C reaction temperature[53]. At 100C sulfated zirconia was found to be inactive while both FeMnSZ and NSZ samples were both active. Indeed the addition of nickel increased slightly the reaction rate above that of FeMnSZ and showed a greater degree of stability over 100 minutes time on stream. The addition of hydrogen into the reaction mixture decreased the rate of reaction considerably and a higher temperature was employed (250C) to obtain measurable activity. An induction period without hydrogen was observed at this temperature, while with hydrogen no induction period was observed. The induction period has been attributed to a build up of intermediate species on the catalyst surface.

Mechanistically, the isomerisation of n-C_4 is thought to involve the generation of an intermediate substituted protonated cyclopropane cation (i) and primary carbenium ion (ii), which undergoes C-C and C-H bond fission and rearrangement the intramolecular/unimolecular route, Figure 2. This process is characteristic of strong acid catalysis the intermediate carbenium ion can be produced either by Lowery-Bronsted acid route (1) or a Lewis acid route (2), Figure 2.

An alternative proposal was given by Adeeva et al[47]. The authors studied ^{13}C labelled n-butane over SZ and FeMnSZ materials for the isomerisation of n-butane. A binomial distribution of isobutanes containing zero, one, two three and four ^{13}C atoms were observed. It was suggested that the classical mechanism of hydrocarbon isomerisation by strong acids generally proceed via a primary carbocation at high reaction temperatures. However at reaction temperatures employed by superacids for n-butane isomerisation a primary carbocation would be energetically unfavourable. Therefore the authors proposed, from the isotopic scrambling of the ^{13}C isotope, an intermolecular process where n-C-4 forms C-8 species followed by C-C fission forming iso-butane.

1.2.2.5:*Calorimetery*

Calorimetery offers the advantage of measuring directly the number and strength of acid sites using ammonia or pyridine titration to measure the heats of adsorption. Fogash and co-workers using micro-calorimetry observed a distribution of acid sites over a range of sulfated zirconia samples and compared these values with those of zeolites H-ZSM-5 and HY using ammonia[54]. The authors observed very strong acid sites in the range 150-165 kJ/mol and intermediate acid sites in the range 125-140kJ/mol. This corresponded to 70μmol of strong-intermediate acid sites per gram of sample. Weak acid sites were also observed in the range of 120-70 kJ/mol. The overall total coverage corresponded to 250μmol of acid sites. Therefore the percentage of strong and intermediate acid sites was ca. 30% of the sample. The high values for the heats of ammonia adsorption lead the authors to conclude that SZ, depending upon the method of preparation, contained acid sites which were very strong and were stronger than those found on the zeolites. The enhanced activity of SZ towards n-butane isomerisation was attributed to intermediate strength acid sites. However the involvement of the strong acid sites, reported as Lewis acid sites, could not be excluded. Further studies by the same group established that the degree of hydration of SZ affected the activity of n-butane isomerisation and the strong acid sites previously observed to be Lewis, were actually Bronsted[55]. The addition of water ca.75μmol/g at 150C to a SZ sample followed by calcined at 500C exhibited 70% of the activity displayed by a SZ calcined at 300C. Further additions of water, however poisoned the catalyst. This may imply that a certain degree of hydration, as proposed by the authors, is required for catalytic activity.

Drago et al using the "Cal-ad" technique came to a different conclusion as to the strength of the acid sites on sulfated zirconia[56]. In studies over SZ, FeMnSZ, HY, PtSZ, HZSM-5 and silica the heats of pyridine adsorption was found to be highest on HZSM-5, Table 3. The experimental results led the authors to conclude that sulfated zirconia is not a superacid, and they expressed some concern of the applicability of the classical hydrocarbon activation mechanism for superacidic systems for sulfated zirconia. The authors favoured the one-electron transfer mechanism proposed by Farciascu[57,58], to explain the enhanced activity observed for pentane isomerisation. Evident from Table 3, is the dependence on calcination temperature of the heats of pyridine adsorption for sulfated zirconia samples. The optimum calcination

temperature for sulfated zirconia is generally taken as 650C. Therefore the results obtained by Drago et al are of SZ in a less than optimum calcination temperature. The use of lower calcination temperatures may affect the results obtained.

Table 3: Results of "cal-ad" measurements or pyridine adsorption on various solids[56]

Sample	$-\Delta H_{ads}$(pyridine)/kJ mol^{-1}
H-ZSM-5	171
HY	142
SO_4^{2-}/ZrO_2 (600C)	130
$Pt/SO_4^{2-}ZrO_2$	125
FMSZ	109
SO_4^{2-}/ZrO_2 (300C)	63
SiO_2	50

( ) indicates temperature of calcination.

These studies clearly show the dilemma, which exists in attempting to measure and interpret the acid strength over SMO materials. Further, Farcasiu and Ghenciu showed that besides the uncertainties associated with the thermal effects due to interactions other than simply acid-base interactions, more than one proton transfer may also occur[48].

1.2.2.6:*Temperature programmed desorption*

Temperature programmed desorption (TPD) experiments by several authors using ammonia, pyridine and benzene all showed that SFe contained acid sites of higher strength than acidic zeolites[59-61]. However, the TPD using probe molecules has been questioned. Park et al, using ammonia and pyridine, TPD with mass spectrometry observed decomposition products CO_2, SO_2 and N_2 and traces of water[43]. The simultaneous appearance of a peak for carbon dioxide, nitrogen and sulfur dioxide indicated that the adsorbed molecule was decomposing at the same time as the sulfate. The concominent appearance of the peaks indicated that the decomposition proceeded via a common process occurring on the surface of the sulfated sample.

Similar observations were made with 1-butene, ammonia and n-butane. Indeed the decomposition temperature of the sulfate species decreased with adsorption of probe molecules. The most pronounced effect was observed with pyridine and 1-butene. Ammonia and n-butane only slightly decreased the temperature of sulfate decomposition. The strength of interaction of the adsorbed molecules was given as an explanation for the decrease in the decomposition temperature of the sulfate. The interaction was thought to be stronger with pyridine and 1-butene than for ammonia and n-butane. The authors proposed that the adsorption of probe molecules on the surface of sulfated iron oxide caused structural changes. These changes caused a reduction in the temperature of sulfate decomposition and created oxygen vacancies, which may relate to Lewis acid centres.

Similar observations were made by Hsu et al they also observed decomposition products over sulfated zirconia and FeMnSZ using substituted benzenes which were previously reported as useful weak base probe molecules for determining the acidity of SMO materials[62]. Corma in his review also warned of the decomposition of adsorbed molecules using TPD measurements on strongly oxidising acidic materials and believed ammonia may also absorb as NH_2^- and H^+ on both acidic and basic sites[35]. Therefore monitoring of the effluent stream from a TPD experiment must be considered.

1.2.2.7:*Electron Paramagnetic Resonance*

Since electron paramagnetic resonance (EPR) is able to detect paramagnetic carbocations formed by charge transfer between surface sites and organic molecules, it has been employed to characterise strong ionising sites on solid acid catalysts using probe molecules difficult to ionise, such as benzene. For example, Vedrine and co-workers found that benzene could only be ionised on H-ZSM-5 or on H-Mordenite zeolites, but not on HY[63]. In addition, they also measured relative acid strengths of SZ catalysts calcined at different temperatures. The intensity of EPR signal of biphenyl radical cation, which was considered to arise from a reaction of a benzene radical cation ($C_6H_6^{\cdot+}$) with a neutral benzene molecule, reached a maximum for a calcination temperature of 600C. On the other hand, SZ catalyst calcined at this temperature showed the highest catalytic activity for n-butane isomerisation. Therefore, there seems to be a close relationship between the ionising

ability and the catalytic activity. Similarly, Coster et al used aniline as a probe molecule and observed the EPR signals of the corresponding radical cations[64].

According to Tanabe, a surface is known to have oxidising sites if it is able to abstract an electron from a suitable molecule to form a paramagnetic radical cation[64]. Yamaguchi et al reported that the adsorption of perylene on SZ gave the typical EPR signal of the corresponding radical cation, whereas no signal was observed on non-sulfated zirconia, indicating that the oxidising property of zirconia is generated by the introduction of sulfate ions.

1.2.2.8:*Nuclear magnetic resonance*

Nuclear magnetic resonance (NMR) spectroscopy is a relatively new technique when applied to solid materials[65,66]. Since ca. 1980's NMR has been applied to solid acids particularly zeolites, to investigate acid strength both qualitative and quantitatively[67,68]. However, it is only in recent years that NMR has also been used to investigate both Lewis and Bronsted acid sites on SMO. The use of NMR spectroscopy offers the ability to study both the structural and chemical environment of the acid centre, and potentially measure acid strengths from the interaction of probe molecules with the catalysts surface which gives rise to chemical shift values.

One of the first research groups to apply NMR spectroscopy to SMO was Coster et al[64]. Their studies used magic angle spinning (MAS) NMR with trimethyl phosphine (TMP), as a base probe molecule, and their results were correlated with ESR spectroscopy using aniline as a probe molecule, over a range of SMO materials. The authors were attempting to correlate Lewis acid strength with catalytic activity in an attempt to define an acidity scale. In using TMP as a basic probe molecule, they proposed that Lewis acidity could be detected from the downfield chemical shift of a TMP:L (L=Lewis acid site) adduct, relative to physisorbed TMP, zero chemical shift. The degree of electron donation (or electron acceptance) of the Lewis acid site, presumably and as discussed later, to the coordinatively unsaturated metal cation, causes the P atom in the TMP molecule to loose electron density.

This effect is thought to cause a noticeable chemical shift, and the size of this chemical shift relative to adsorbed TMP gives an indication of acid strength.

By comparing the chemical shift of a series of SMO of known or approximate acid strengths measured using Hammett indicators or other means, an acid scale may be

produced which may then be applied to unknown solid acids such as zeolites. Table 4, shows the results of the authors ESR and MAS NMR experiments over SMO.
ESR spectroscopy results showed on the basis of line widths the following order of acidity:-

$$ZrO_2 > HfO_2 > Al_2O_3 > TiO_2$$

Table 4: ESR and NMR results for a range of SMO samples[64]

Sample	ESR	NMR		
	g	Bronsted (ppm)	Most upfield (ppm)	Most downfield (ppm)
SO_4^{2-}/ZrO_2 (550)	36.5	-3.2	+26.0, +23.0	-33.0
SO_4^{2-}/HfO_2	38.5	-3.0	+22.4	-36.0
SO_4^{2-}/A_2O_3	47.7	-4.0	-	-46.0
SO_4^{2-}/TiO_2 (350C)	-	-3.7	-	-

Chemical shifts of ca. 3-4ppm are due to protonated TMP where the interaction of TMP with protons forming $TMPH^+$ affects also slightly the electron density around the P nucleus hence the chemical shifts observed is small relative to adsorbed TMP. The formation of Bronsted sites were believed to be formed by the adsorption of water, since increasing the outgassing temperature for STi resulted in a suppressed intensity of the line at ca. 3ppm. In the case of sulfated haffnia and zirconia, (SHf, SZ respectively), strong upfield shifts were observed at +22.4 ppm and +26.0 ppm respectively. These lines were attributed to strong Lewis acidity. No such chemical shifts for the other SMO investigated were observed. However, in all SMO samples a band ca. 3-4 ppm was observed indicating the presence of Bronsted acid sites.
The downfield chemical shifts observed for the group (IV)B metals do not differ significantly and do not correlate with the Lewis acidity measured by ESR. Therefore as the authors noted, the downfield shift probably reflects the similar electron distribution of group (IV)B elements. The authors proposed on the basis of differences in the group (IV)B metals and aluminium electronegativity that the lines observed at ca. -30ppm group (IV)B and -46ppm for aluminium oxide, were attributed to centres more remote from the sulfate group.

The magnitude of the upfield chemical shift observed for SZ and SHf correlated with the findings from ESR spectroscopy experiments. Lunsford and co-workers studied fresh and aged SZ, outgassed in the temperature range 100-320C, using TMP MAS NMR spectroscopy[69]. Their results showed that acid sites were affected by pre-treatment conditions. Low temperature pre-treatment in vacuo for SZ showed lines at ca. –3ppm, which were assigned to Bronsted acid sites, with only a weak line at ca. –46ppm, which was assigned to Lewis acid sites. Increasing the temperature of outgassing led to a decrease in the intensity of the line associated with Bronsted acidity and an increase in the intensity of the line associated with Lewis acidity. Further an additional line was evident at ca. –39ppm, at a temperature of 200C, indicating the presence of more than one type of Lewis acid site. On outgassing at the highest temperature of 320C the lines associated with Lewis acidity increased while those of Bronsted acidity generally decreased. However additional lines at +23 +26, +34, +63 and at +91 ppm were observed. The latter lines were assigned to the formation of TMPO, which were thought to be formed by the oxidising ability of the coordinatively unsaturated sites i.e. Lewis acid sites on the TMP molecule. However the authors could offer no explanation for the lines observed at +23ppm and +26ppm, but gave the following reasons as to why they believed that the assignment of these lines to Lewis acid sites to be incorrect:

1. Chemical shifts as large as +24ppm were known for soft acid-base interactions.
2. Aluminium (III) chloride, a strong Lewis acid, has a chemical shift of ca. -42ppm only.

Therefore the use of MAS NMR with TMP to observe Lewis acidity is still in its early stages particularly with SMO. The measurement of fractional electron exchange density from ESR line(s) to define Lewis acidity is difficult. As pointed out by Lunsford et al, there may well be more than one type of Lewis acid sites, although these authors attempts at defining the sites from the model of the active site given by Clearfield et al, discussed later, is somewhat confusing[69,70].

Broad line ^{1}H MAS NMR used to define Bronsted acidity has been used successfully to determine protonic acidity. Reimer et al studied the protonic acidity of sulfated

and unsulfated zirconia[71,72]. They observed downfield shifts of 5.85ppm for SZ and 3.86ppm for non-sulfated zirconia. The difference of ca. 2ppm, was described by the authors as a significant chemical shift which showed the increase in Bronsted acidity due to sulfate incorporation. The chemical shift value for SZ was much higher than that reported by Mastikhin et al for H-ZSM-5 (4.3 ppm)[73]. However SZ prepared by impregnation of sulfate on the crystalline oxide also gave a similar result to that of a sample where sulfate had been impregnated onto amorphous zirconia. Studies by Riemer et al on sulfated and non-sulfated zirconia reported results similar to Lunsford. However these authors further observed chemical shifts of +65.7ppm for SZ. They attributed this line to the oxidation of TMP to a protonated TMPO species, demonstrating the oxidising ability of SZ. TMPO was not detected on unsulfated zirconia.

However studies by Semmer et al used water adsorbed onto SZ, sulfuric acid, Nafion-H, CF_3SO_3H and $H_2Nb_6O_{16}$ to attempt to establish the concentration of Bronsted acid sites by proton solvation[66]. The authors found that the strong acids characterised adsorbed the same number of water molecules per Bronsted site, ca. 1.0 while the weaker niobium based acid was found to be, ca. 0.2. The authors concluded that since they could only differentiate between strong and weak acids that this was not a suitable technique for quantifying Bronsted acidity and proposed the use of a weaker base such as hydrogen sulfide. Further the adsorption of water molecules on SZ was observed not to first interact with the protonic groups this indicating a problem of accessibility of probe molecules to the acid sites on SZ.

1.4:Nature of the acid site

To understand how sulfation enhances the acidity of SMO materials, a number of studies have attempted to determine the nature of the active site. Many proposals have been presented in the literature. Generally these have employed infrared spectroscopy to examine the symmetry of the co-ordinated sulfate group.

It must first be noted that sulfate can exist with several different symmetries as shown in Table 4. The different forms may be identified by observing the number of bands in the S=O stretching region in the range 1200-900 cm^{-1}. However, distinguishing between the two point groups with C_{2v}, i.e. bridging and chelating

symmetry, is difficult since they both have the same number, 4, of infrared active bands, Table 5.

Table 5: A table of the stretching frequencies for S=O[11]

Compound	Structure	Symmetry	Wavenumber/cm^{-1}	
			V_3	V_1
SO_3^{2-} Bound to metal through an oxygen	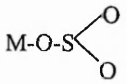	C_s	902 862	989
SO_3^{2-} Bound to a metal through a sulfur	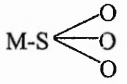	C_{3v}	1050-1120	940-985
Organic sulfites	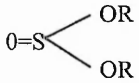	C_{2v}	1180-1250	1030-1050
SO_4^{2-}	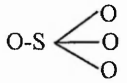	T_d	1105	
Unidentate SO_4^{2-}	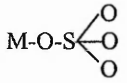	C_{3v}	1117-1147 1032-1044	970
Bridged bidentate SO_4^{2-}	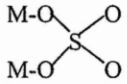	C_{2v}	1160-1195 1105-1110 1030-1035	960-990
Chelating bidentate SO_4^{2-}	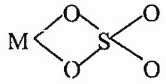	C_{2v}	1230-1240 1090-1125 995-1035	940-960
Organic sulfates	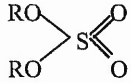	C_{2v}	1350-1460 1150-1230 975-1000	910

In order for any model to describe the nature of the acid site, it must explain the following experimental observations:

1. **The symmetry of the surface sulfate.**
2. **The generation of Lewis/Bronsted acid sites.**
3. **The interaction of probe molecules with the surface sulfate species.**
4. **The simultaneous decomposition of sulfate and absorbate.**

5. A relationship between the structure of the acid site with catalytic activity.

Yamaguchi et al was among the first to investigate the nature of the acid site[11,18,74]. Studying a number of SMO sulfated with ammonium sulfate,(AS), the authors observed four bands in the S=O region, indicating that the structure of the surface sulfate species was similar on all the SMO materials examined. However the catalytic activity for the ring opening of cyclopropane was different, as discussed in the previous section 1.2.2.3. Therefore the enhanced activity cannot be due solely to the interaction of sulfate with the metal oxide surface. Further, it was observed that metal oxides pre-treated with SO_3 produced similar infrared spectra to those impregnated with ammonium sulfate, indicating that the nature of the sulfating reagent did not alter the final structure of the surface sulfate species. Adsorption of H_2S and SO_2, where sulfur is in the –2 and +4 respectively, was found to produce different infrared spectra, in these samples sulfate was in a T_d symmetry. On calcination of these samples in air, similar infrared spectra were again observed, with sulfate in a C_{2v} symmetry, indicating that the oxidation state of the sulfur species relates to the formation of the symmetry observed for SMO. Therefore from the work of Yamaguchi et al it is clear that the nature of the surface sulfate species is independent of the sulfating reagent as long as the sulfur is in an oxidised form. X-ray photoelectron spectroscopy (XPS) studies on AS/SMO samples, confirmed that sulfur was in the +6 oxidation state and generated infrared spectra similar to those observed for the AS/SMO. However since all the SMO materials exhibited the same infrared spectra, the structure of the sulfate species itself, as observed by infrared spectroscopy, is not sufficient to explain the differences in catalytic activity. Therefore, the authors proposed it was the specific interaction of the adsorbate with the surface sulfate species, which gave rise to the observed catalytic activity for the different materials. This interaction of adsorbate and sulfate was suggested to bring about a change in the S=O bond order. Using an empirical relationship derived by Gillespie, the bond order of a range of SMO before and after pyridine adsorption was calculated, Table 6.

Figure 3: Yamaguchi model for sulfated iron oxide[112]

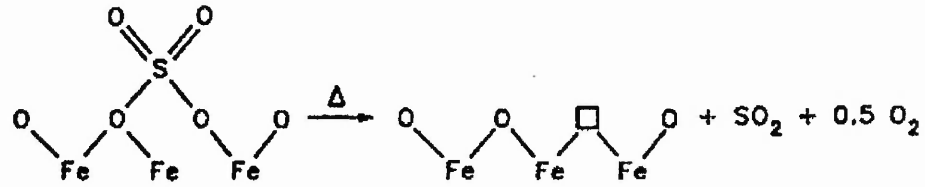

(I) **(II)**

In conclusion the authors stated it was the strong ability of the sulfur complex with structure (I), Figure 3, to accommodate electrons from the base molecules which reduced the bond order of the S=O, which gave rise to the highly acidic properties for SMO materials. Yamaguchi and co-workers described the SMO materials examined as consisting solely of Lewis acid sites but suggested that Bronsted sites may be created by the adsorption of water molecules[11]. However, Tanabe et al commented that this does not necessarily imply that the reaction examined is Lewis acid catalysed[32]. Their isotopic tracer experiments of the ring opening of cyclopropane and 1-butene isomerisation over sulfated iron oxide indicated that a carbocation intermediate formed via proton addition to the hydrocarbon was involved[32]. Yamaguchi and co-workers further suggested that the infrared results merely showed the nature of the catalyst before reaction, which under reaction conditions would be different.

Table 6:Changes in bond order of the SO bond by pyridine adsorption[18]

Catalyst	Bond order		SO stretching frequencies cm^{-1}	
	Before Py ads	After py ads	Before Py ads	After Py ads
AS/ZrO_2	1.86	1.78	1390	1339
AS/TiO_2	1.84	1.76	1375	1326
AS/Fe_2O_3	1.84	1.76	1375	1329
AS/Al_2O_3	1.88	1.82	1398	1365
AS/SiO_2	1.89	1.89	1410	1410
AS/Bi_2O_3	1.83	1.83	1370	1370

AS= ammonium sulfate, Py=pyridine, ads=adsorption

Infrared absorption experiments by Arata et al. showed the ease of inter-conversion between Lewis and Bronsted sites Figure 4,with the adsorption of water molecules[6]. The authors proposed a bidentate sulfate species of bridging C_{2v} symmetry where the S=O bond character was much stronger than observed for metal sulfates. This increased the Lewis acid strength of the metal cation by the inductive effect of the S=O in the adsorbed sulfate complex. Therefore the model proposed by Arata et al is similar to that of Yamaguchi and co-workers. However, this model shows the presence of both Lewis and Bronsted acidity, which the authors claim upon heating removes the water by producing solely Lewis acid sites.

A further model proposed by Clearfield et al[70], studied the structures of hydrous zirconia and zirconium sulfates. They commented that a chelating sulfate would leave the zirconia cation 8-coordinate and therefore not a Lewis acid centre as proposed by Yamaguchi et al. The authors proposed a model based on infrared pyridine adsorption experiments on SZ using sulfuric acid and ammonium sulfate as the sulfation reagents. Figure 5, shows a bridging bisulfate species, the predominant species formed in a sulfuric acid solution before calcination. On calcining at 300C, the proton on the bisulfate could displace a nearby hydroxyl bridge, thus forming a strong Lewis acid site, top right in Figure 5.

Figure 4: The interconversion of Lewis to Bronsted acid sites by water adsorption[6]

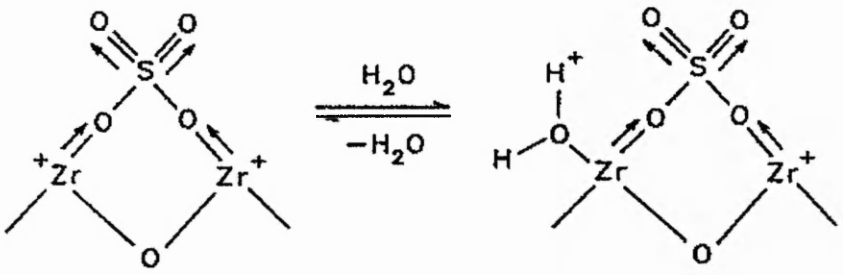

Figure 5: Structure of sulfates adsorbed onto hydrous zirconia[70]

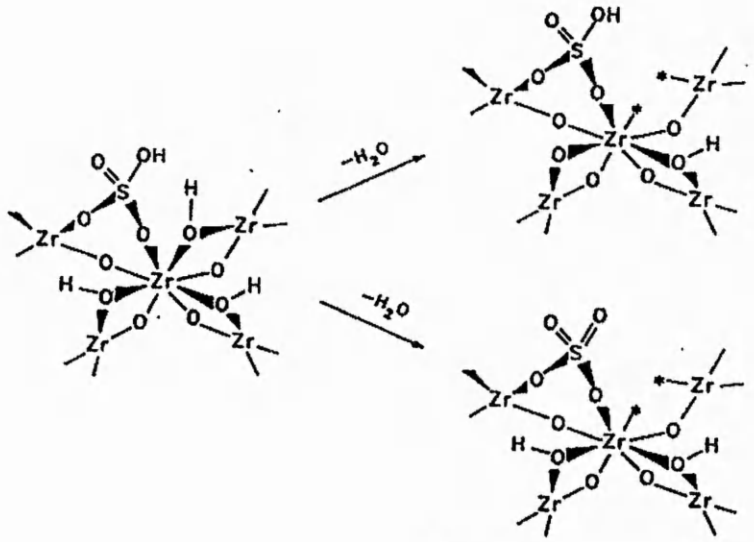

When ammonium sulfate is used, sulfate is the predominant species, and the structure bottom right in Figure 5 is formed. Vedrine et al described a two step chemical reaction between superficial hydroxyl groups on zirconium hydroxide and adsorbed sulfate in the form of sulfuric acid at the drying stage i.e. below 400C and the incorporation of sulfate on calcination at increased temperatures[75]. Clearfield's model explains many observations in the literature, such as the simultaneous presence of Lewis and Bronsted sites, which were both, believed to be required for activity[69,76].

1.3: Metal oxide/ metal oxide superacids

Impregnation of metal oxide precursors onto hydrous zirconia followed by high temperature calcination, are described as "superacidic" by Arata et al[77-80], whereas the impregnation of crystalline zirconia produces a partial oxidation catalyst which has been extensively investigated in the literature[81-83]. The impregnation of tungstate or molybdate, particularly, has been shown to cause catalytic activity for a range of acid catalysed reactions including n-butane isomerisation. Arata et al were the first to discover metal oxide supported metal oxide (MO/MO) superacids, and compared them to their crystalline doped counterparts for typical acid catalysed reactions e.g. dehydration of 1-propanol and the isomerisation of iso-pentane. Their results showed

that MO/MO materials displayed greater activity for the acid catalysed reactions[77]. In quantifying the acidity of these materials by the Hammett acidity method, the authors reported values of $H_o < -12.0$, indicating that these materials were indeed superacidic. The first MO/MO materials prepared were MoO_3/ZrO_2 (MHZ) and WO_3/ZrO_2 (WHZ) (H indicates impregnation onto hydrous zirconia), which had Hammett acidity values of $H_o < -12.7$ and -14.7 respectively. They were unable to quantify MHZ due to the yellow colouration of this sample, and assigned the Hammett value according to comparative catalytic experiments. Several different types of MO/MO solid superacids were developed by the authors, e.g. WO_3/TiO_2, WO_3/SnO_2, and WO_3/Fe_2O_3. In all cases, high calcination temperatures were employed and the activity of these materials was superior to their crystalline impregnated MO/MO counterparts. The thermal stability of these types of solid superacids is generally higher than SMO materials where calcination temperatures below ca. 700C are employed due to the reduction of catalytic activity as a result of sulfate decomposition.

1.3.1: Preparation

Typical preparation methods for WHZ and MHZ are given below. Analogous methods for WO_3/TiO_2, WO_3/SnO_2 etc. exist.

$$ZrOCl_2 \cdot 8H_2O + NH_{3(aq)} \xrightarrow{pH\ 8} Zr(OH)_4$$

$10g\ of\ Zr(OH)_4 + 3.8g\ (NH_4)_6(H_2W_2O_{40}) \cdot nH_2O\ in\ 15ml\ H_2O$

OR $\quad + \ 2.54g\ H_2MoO_4\ in\ 2ml\ H_2O$

Followed by:
1) Evaporation of water at room temperature
2) Drying at 100C.
3) Generally calcination temperatures in the range 600-900C to achieve optimum activity.

Williams et al and Machej et al questioned the method used for the preparation of solid superacids[84,85]. These sets of authors proposed that the catalytic activity of these materials does not depend on the preparation method but on the nature of the support, molybdenum or tungsten oxide loading and calcination temperature. Wachs et al, from their studies on the design of supported group V-VII metal oxides stated

that the only important factor was the chemical nature of the support and the active oxide. They concluded that the synthesis method was not critical since it cannot considerably affect the structure of the support.

Therefore, there appears a division in the literature between those authors who believe that the preparation conditions of MO/MO materials are unimportant and those authors who believe it is. It is evident that the differences in activity between the crystalline doped and the hydrous doped supported metal oxides may depend upon bulk or micro-structural changes upon impregnation or calcination. Several studies have been performed to elucidate the structural nature of MO/MO materials by comparing different preparation routes with catalytic activity.

1.3.2: Catalytic activity

Superacidic MO/MO materials have been applied to several reactions, which are proposed to display their enhanced activity due to the method of impregnation of the metal oxide as previously discussed.

Arata et al was the first to discover these materials and applied them to the dehydration of ethanol, isomerisation of iso-pentane and the bezolylation of toluene with benzoic acid[6]. In general high calcination temperatures were required to achieve optimum activity (in the range 700-1000C). Table 7 displays activity data for the dehydration of ethanol at 190C over a range of tungsten impregnated oxides

From Table 7, it is evident that the activities of the MO/MO materials are greater than the commercial aluminosilicate (13wt% alumina). The major product for all samples was diethyl ether indicative of an acid catalysed reaction mechanism. Industrially, sulfuric acid is used for the formation of diethyl ether. The oxidation ability of MO/MO systems was also demonstrated by Arata et al. al. for the isomerisation and cracking of iso-pentane. The major products for the reaction was CO_x over tungstated iron and tin oxide samples, described as superacids, as well as a range of C-4 to C-7 products over the other materials. The aluminosilicate sample was inactive for this reaction at a reaction temperature of 250C.

Afanasiev studied the dehydration of iso-propyl alcohol, (IPA), over molybdenum doped zirconia materials at 200C[86]. Calculated reaction rates showed that a MHZ sample was much more active than yittria stabilised zirconia material with conversions of $6x10^{-6}$ and $5.6x10^{-8}$ $molg^{-1}s^{-1}$ respectively. However n-butane

isomerisation studies over both materials showed no reaction products. In comparison SZ displayed higher activity, although the values for this reaction were not tabulated.

Table 7: Tungsten oxide impregnated on a range of metal oxides for the dehydration of ethanol at 190C[6]

Sample	Maximum ethanol* conversion (%)	Optimum calcination temperature/C
WO_3/ZrO_2	47	800
WO_3/SnO_2	67	1000
WO_3/TiO_2	73	700
WO_3/Fe_2O_3	33	700
SiO_2-Al_2O_3	18	500

*Reaction temperature 160C.

The authors therefore concluded that MHZ samples were less acidic than SZ. Yan et al observed similar trends for WZH and SZ for n-butane isomerisation[61]. It was observed that the WHZ material was active for n-butane isomerisation and the activity of this material increased with increasing tungsten oxide content. The optimum content of tungsten oxide was found to be ca. 15wt%, further WHZ samples had a lower activity than SZ examined under the equivalent test conditions. However, the SZ sample deactivated more rapidly than the WHZ sample.

1.3.3: Acid strength

Much of the literature on superacidic MO/MO materials relates to studies by by Arata et al[6]. As a consequence, the measurements of acidity were performed using the Hammett acidity method. The limitations of such measurements have been mentioned previously in connection with sulfated metal oxides (Section 1.2.2.1). In view of the limitations of the Hammett method for solid acids, previously described, it would appear that the assignment of Hammett values to these materials is ambiguous.

Table 8: Pyridine adsorption infrared data molybdated and yittria stabilised samples[87].

		Absorbance (mass normalised)* / cm^{-1}				
Sample	T_{evac}/C	1638 (B)	1608 (L)	1540(B)	1450 (L)	1466 (L)
	25	35	95	32	113	0
7wt%	150	28	63	28	25	0
MoO_3/ZrO_2	250	6	28	8	10	0
800C	350	2	16	0	5	6
(216 $m^2 g^{-1}$)	450	0	12	0	5	5
	25	50	80	58	120	0
7wt%	150	40	75	40	40	0
MoO_3/ZrO_2*	250	30	30	15	12	30
800C	350	18	20	5	10	20
(247 $m^2 g^{-1}$)	450	5	12	0	10	10
	25	10	90	0	180	0
6wt%	150	0	70	0	60	0
Y_2O_3/ZrO_2	250	0	40	0	30	0
800C	350	0	10	0	15	0
(165 $m^2 g^{-1}$)	450	0	10	0	15	0

B= Bronsted, L=Lewis acid centres * prepared according Arata method[4]

Indeed the assignment of strong acidity was based solely on catalytic data and compared to commercial zeolites or to SZ. Attempts at measuring the acidity of molybdate doped zirconia, prepared via different routes, by pyridine adsorption were performed by Afanasiev et al[87]. Table 8 summarises the adsorption data from their experiments for MZH samples prepared via different routes. However this data does not compare MZH samples with MZ samples, which would be more informative.

Table 8 shows the presence of both Bronsted and Lewis acid sites. The absorbance has been mass normalised, although not specific surface area normalised. The surface areas of the samples are shown in the table. It is evident that the yittria stabilised zirconia sample contains only Lewis acid sites, which are in general higher than the other samples irrespective of the outgassing temperature. The 7wt% MHZ material, prepared via the Arata method[27], has a higher proportion of both Bronsted and Lewis acid sites even at the higher outgassing temperatures. Analogously to SZ

it was proposed that both types of acid sites are required for enhanced activity of MO/MO materials. In the decomposition of iso-propyl alcohol (IPA), the AM sample displayed a 3-fold increase in activity over the FM sample. These results do not conclusively answer the question of acid strength but provide an indication only.

1.3.4: Nature of acid sites

Afansiev et al, on the basis of XRD, ultra-violet spectroscopy and temperature programmed desorption of ammonia experiments on molybdated zirconia samples deduced that the molybdenum oxide species was the same on all species irrespective of the method of preparation[87]. However, EPR of adsorbed aromatic molecules IR spectra of adsorbed pyridine and catalytic tests observed differences between the samples impregnated with molybdenum precursor onto the hydrous and crystalline zirconium support. The authors proposed that a majority of the molybdenum oxo species was the same in all the samples, which gave rise to similar characterisation results. However, some of the molybdenum oxo species in the hydrous impregnated molybdate samples were present on some peculiar superficial centres, giving rise to strong acidity, and differences in the EPR signal. These centres were believed by the authors to relate to the enhanced activity observed. Based on their experiments and analogies from inorganic chemistry of molybdenum oxo species the authors proposed a model for the nature of the active site, Figure 6, the first ever presented for molybdated zirconia superacidic materials.

Figure 6: Proposed model for the nature of the active for MO/MO materials[88]

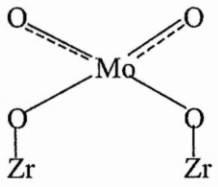

The essential features of the model are the protonic nature of the acid centre, the presence of at least two metal=oxygen atoms near to the acid site. It was thought that high calcination temperatures were required to obtain the metal oxygen double bond via the simultaneous crystallisation of the support and the decomposition of the molybdenum precursor to generate the above structure. A different structure was

proposed for the impregnation of the molybdenum precursor on a crystalline surface. In this case the surface is covered by -OH species, which are replaced by molybdenum or tungsten oxoanions, where superacidic centres are not created.

Zhao et al on the basis of their Raman studies also proposed a similar model on the basis of new surface state present in the molybdenum impregnated hydrous zirconia samples and not in the crystalline impregnated samples. The authors stated that increasing the temperature of calcination narrowed the band for the new surface Mo-O-Zr sate indicating a strengthening of the interaction between the molybdate oxo species and the zirconia support.

1.4: Summary

The oxidation of methane involves the activation of the C-H bond(s) to form a reaction intermediate followed by an oxygen insertion mechanism and the release of the product(s). Oxygen insertion may, depending upon the mechanism of the reaction the type of catalyst and the oxidant used, be inserted in the gas phase or on the catalyst surface, while activation of the methane molecule generally takes place on the surface, in a catalysed process. The strength of which the catalyst binds with the methane molecule often dictates the nature of the products formed. Generally, for the synthesis of partial oxidation products such as methanol or formaldehyde the catalyst is required to bind methane relatively weakly to the surface. Strong interaction of methane with the catalyst surface may lead to over oxidation and complete combustion products, i.e. carbon dioxide and water, being formed. Oxygen insertion may be performed on the surface of the catalyst either from molecular oxygen, in an activated process, or by a concerted mechanism, e.g. Mars Van Krevelen type mechanism, where the oxygen molecule originates from the crystal lattice and is replaced by molecular oxygen present in the feed. Therefore, in this respect metal oxide materials are an advantage for partial oxidation reactions, due to their lower catalytic activity for hydrocarbon oxidation and the ability to donate oxygen from the lattice, compared to noble metals. Similarly, noble metals are generally considered as useful catalysts for the complete oxidation of methane due to their ability to interact strongly with hydrocarbons.

Industrially, the partial oxidation of methane, from natural gas to form methanol, is a two-stage process. The first stage involves the "stripping" of the methane molecule

of its hydrogen atoms via a process known as steam reforming, which is a highly endothermic process, $\Delta H = +206 kJ/mol$, equation 1.

$$CH_{4(g)} + H_2O_{(g)} \xrightarrow{Ni/\gamma\text{-}Al_2O_3/800C} CO_{(g)} + 3H_{2(g)} \quad \text{Eqn. 1}$$

The second stage is an exothermic process, $\Delta H = -90.64 kJ/mol$, where the hydrogen atoms are replaced and oxygen is included.

$$CO_{(g)} + 2H_{2(g)} \xrightarrow{Cu/ZnO/Al_2O_3 \text{ ca. } 300C} CH_3OH_{(g)} \quad \text{Eqn.2}$$

Therefore, in general the industrial two-stage partial oxidation of methane to form methanol reaction is limited by the need to maintain the reaction temperature and the removal of 1 mole of hydrogen for every mole of methane converted in the first stage, before stage two can be operated. Therefore the current process is energy intensive.

In this respect a direct one-stage methane to methanol process would be advantageous.

$$CH_{4(g)} + O_{(2)} \longrightarrow CH_3OH_{(g)} \quad \Delta H = -127 \text{ kJ/mol} \quad \text{Eqn.3}$$

The heat produced from the reaction could be utilised to operate other parts of the plant. Further, the reduced costs of the above direct one-stage process would be able to exploit at source, sources of natural gas, some of which are currently found in remote locations e.g. Siberia, where transportation costs are expensive. In this respect there exists a wealth of literature regarding investigations of a direct one-stage process for the synthesis of methanol and/or formaldehyde. However, the main problem associated with the above reaction is the low selectivity towards partial oxidation products with over oxidation to carbon oxides occurring. Therefore one of the main aims for the success of this reaction is the prevention of over oxidation of the oxygenated product. The activation of methane may be performed via hydride abstraction yielding a methyl anion, basic catalyst or a methyl radical in a free radical process e.g. gas phase homogeneous process. The interest for this study in the novel application of strongly acidic solid metal oxides termed, "superacids", for the direct partial and complete oxidation of methane, derives from the analogous

activation of hydrocarbons, including methane, by liquid superacids, i.e. the formation of carbocation intermediates. The formation of carbocation intermediates by solid superacids may invoke a novel activation process, i.e. protonation of methane, a weak base, forming a CH_5^+ carbocation. Hence, one may envisage the possible formation of primary carbocation type intermediates over solid superacids, which are known to be formed in superacidic liquid media. Further, the addition of molecular oxygen to the reaction feed may react with the carbocation so forming oxygenated products such as methanol. Therefore the use of solid superacids may offer an alternative carbocation intermediate mechanistic pathway, favouring the formation of oxygenated products.

Iron oxide possess many polymorphs which are dependent upon the method of preparation and offers the ability to study a structure function type relationship which may be more generally applied to solid superacids. In view of the method of preparation of SMO the nature of the precursors for sulfated iron oxide has not been evaluated. Similarly MO/MO solid superacids are of interest in view of the relatively small amount of literature available on these materials. In this respect the study of MZH type superacids are of particular interest since many partial oxidation catalysts contain molybdenum oxide, present in many partial oxidation catalyst formulations.

The study of the complete combustion of methane in Chapter 5 of this thesis, originated from previous experimental results obtained during this study. However, the complete combustion of methane to carbon dioxide is also of environmental and academic interest since methane may be considered as an environmental pollutant. Further the catalytic combustion of methane enables the reduction of the ignition temperature < 1000C, above which NO_x also an environmental air pollutant, is formed. In Chapter 5 of this thesis SMO and MO/MO superacidic materials as well as ceria/zirconia materials were investigated for their efficacy for the complete combustion of methane. Trovarelli et al reported on the novel use of ceria/zirconia type materials for hydrocarbon combustion[168]. Therefore these materials as well as the superacidic materials were investigated for methane combustion. For comparative purposes simple oxides, iron and copper, and supported platinum metal materials, known for their catalytic activity for hydrocarbon combustion, were also studied.

Hence this study investigates the use of superacidic materials based on sulfated iron oxides derived from several polymorphs of iron oxyhydroxides/hydroxides and a range of molybdated zirconia materials for the partial and complete oxidation of methane.

2.0: CATALYST PREPARATION, CHARACTERISATION AND CATALYTIC TESTING.

2.1: CATALYST PREPARATION

2.1.1:Preparation of iron and oxyhydroxides and hydroxide precursors

As mentioned in the introduction, previous studies of sulfated metal oxides have demonstrated the importance of the precursor; therefore sulfated iron oxides were prepared from several polymorphs of iron oxyhydroxide/hydroxide. The methods of preparation were based on those in Schwertmann and Cornell, "The Preparation of Iron Oxides in the Laboratory"[89], and were modified as follows.

(i): *Lepidocrocite*

60 mmol of unhydrolysed iron (II) chloride tetrahydrate (Fisons 98+%) was added to 300 ml of distilled water. The pH of the solution was adjusted to pH 6.7- 6.9 by the dropwise addition of a 5M sodium hydroxide solution. A flow of air (200-300 ml/min) was continuously bubbled through the solution while stirring. The pH of the solution was kept constant during the oxidation of the Fe^{2+}, by further additions of the sodium hydroxide solution, until 120 ml of base was added, where the reaction was complete. The orange precipitate was then filtered through a glass sinter funnel and washed with 4 x 1L of distilled water before drying in a vacuum oven at room temperature for two days. Powder x-ray diffraction confirmed the phase to be lepidocrocite (JCPDS 8-98).

(ii): *Goethite*

100 ml of a 1M solution of iron (III) nitrate nonahydrate (Avocado 98+%), prepared using distilled water, was added to a polythene screw top bottle. To this, 180 ml of a 5M sodium hydroxide solution was added while stirring. This solution was then diluted to 500 ml with distilled water and aged in an oven at 70C for sixty hours. The resultant yellow precipitate was then filtered and washed with distilled water and dried in a vacuum oven for two days. X-ray diffraction of this sample indicated the phase to be goethite (JCPDS 27-713).

(iii): *Feroxyhyte*

300 ml of a 0.1M solution of iron (II) chloride tetrahydrate (Fisons 98+%) was added to a 1L glass beaker and the pH of the acidic solution was adjusted to pH 8 by the dropwise addition of a 5M sodium hydroxide solution. 90 ml of hydrogen peroxide (Fisons 30% H_2O_2) was added rapidly. The resulting precipitate was then filtered and washed with 4 x 1L of distilled water and dried in a vacuum oven at room temperature for two days. Powder x-ray diffraction of this sample was consistent with the feroxyhyte phase (JCPDS 13-87).

(iv): *2-Line Ferrihydrite*

40 g of iron (III) nitrate nonahydrate (Fisons 98+%) was dissolved in 500 ml of distilled water. To this solution 330 ml of a 1M sodium hydroxide solution was added to raise the pH to 7.5, while stirring, with the last 20 ml being added dropwise. The resulting precipitate was then filtered and washed with 4 x 1L of distilled water and dried in an oven at 100C overnight. Powder x-ray diffraction indicated that this sample was consistent with 2-line ferrihydrite (JCPDS 29-712).

(v): *Arata method*

The preparation of this precursor is taken from the literature[6] and is analogous to the method for the preparation of the 2-line ferrihydrite precursor described above, except the pH was raised to 9 by further additions of a 1M sodium hydroxide solution. Powder x-ray diffraction of this material was consistent with 2-line ferrihydrite.

2.1.2: Sulfation procedure

Sulfated iron oxides, denoted SO_4^{2-}/Fe_2O_3, were prepared by immersing the precursor in sulfuric acid solution for 30 minutes (1g of precursor:15ml of 0.5M sulfuric acid solution). The suspension was then filtered and the filtrate was then dried in an oven at 100C overnight. Samples were then calcined at 550C for three hours in air. Sulfated iron oxide derived from goethite was also calcined at 800C for twelve hours using a ramp rate of 10C/min for the methane combustion experiments.

2.1.3: Non-sulfation procedure

Non-sulfated iron oxides, denoted H_2O/Fe_2O_3, were prepared in an analogous manner to their sulfated counterparts except immersion was performed in distilled water. Iron oxide derived from goethite was also calcined at 800C for twelve hours using a ramp rate of 10C/min for methane combustion experiments.

All iron based samples were stored as the hydroxide in capped glass vials. Sulfation or water impregnation was performed as required and calcined at the appropriate temperature. Zirconia samples were stored as the impregnated hydroxide and stored in glass sample bottles and calcined at the appropriate temperature when required.

2.1.4: Preparation of zirconium hydroxide

Zirconium hydroxide, as described in the literature, is the precursor for several types of solid "superacids" including sulfated, molybdated and tungstated zirconias. The preparation method for the hydroxide is described as follows:

To a 0.5M zirconium basic carbonate (MEL) solution, prepared in a 1:1 ratio of distilled water and hydrochloric acid (Fisons SG 1.18 m^3/g), ammonia solution (Philip Harris 35% NH_3) was added dropwise until pH 10 was reached. The precipitate was then filtered and washed with 4 x 1L of distilled water and dried in an oven overnight at 110C. An amount of this material was then calcined in static air at 800C for twelve hours at 10C/min.

2.1.5: Molybdenum (VI) oxide supported on zirconium oxide

Molybdated zirconia was prepared by the incipient wetness technique on the zirconium hydroxide precursor. Zirconium hydroxide was placed in a solution containing appropriate amounts of ammonium molybdate tetrahydrate (Aldrich 99.98%) and mixed using a micro-spatula. A ratio of 0.445 g of distilled water per gram of zirconium hydroxide was used as to obtain loadings corresponding to 2, 5 and 10 wt% MoO_3/ZrO_2 samples. The samples were then dried in an oven at 110C overnight and calcined at 800C for 12 hours in static air.

2.1.6: Iron manganese sulfated zirconium oxide

The method followed was as described by Adeeva et al[46]. 10 g of sulfated zirconium hydroxide (MEL) was immersed in 10 ml of a 0.5M solution of iron (III) nitrate nonahydrate (Fisons 98+%) in distilled water for two hours while stirring. The sample was dried in an oven overnight at 110°C. The dried sample was then immersed in 10 ml of a 0.1M solution of manganese (II) nitrate (Aldrich 45-50 wt% manganese nitrate, dilute aqueous solution of <5wt% nitric acid) in distilled water for two hours while stirring. The sample was again dried in an oven at 110°C overnight. The sample was then calcined at 800C for twelve hours in static air at a ramp rate of 10C/min.

2.1.7: Platinum supported on metal oxides

Platinum supported on non-sulfated iron oxide derived from goethite, sulfated and non-sulfated zirconium oxide, and 5 wt% molybdated zirconium oxide samples were prepared. The wet impregnation technique was performed on the oxide using an aqueous solution of hexachloroplatinic (IV) acid (Aldrich 8wt% aqueous solution of platinum), 0.016g of hexachloroplatinic acid in 0.5g of distilled water per gram of oxide corresponding to ca. 0.5wt% of platinum. The samples were then dried in the oven overnight at 110C. Resultant samples were then heated in-situ in a 100 ml/min flow of helium (Air products 99.999%) at 300C for three hours prior to activity testing, so as to obtain 0.5 wt% loading of platinum on the oxide.

2.1.8: 10 wt% zirconia supported on cerium oxide

To a 1:1 solution of nitric acid (Fisons) and distilled water, 4 g of zirconium basic carbonate (MEL) and 12 g of cerium carbonate (Aldrich 99.9%) were added while stirring. Ammonia solution (Philip Harris 35% NH_3) was then added to form a purple precipitate at pH 10. The precipitate was then filtered and washed with 4 x 1L of distilled water and dried in an oven at 110C.

2.1.9: Cerium oxide supported on zirconium oxide

A solution of 1.2g of zirconium basic carbonate (MEL) and 11.0 g of cerium carbonate (Aldrich 99.9%) was prepared in 700 ml of a 1:1 volumetric ratio of distilled water with hydrochloric acid, (Fisons S.G. 1.18 m^3/g). This solution was

slowly added to 1.5 L of ammonia solution, (Philip Harris 35% NH_3), to precipitate the product at pH 10. To this precipitated solution was added 50 ml of hydrogen peroxide, (Fisons 100 volumes), was added. The precipitate was then filtered and washed with 4 x 1L of distilled water and dried in an oven at 110C.

2.1.10: Sulfated zirconium oxide

Sulfated zirconia was prepared by calcining sulfated zirconium hydroxide (MEL) at 800C for twelve hours in static air using a ramp rate of 10C/min.

2.1.11: Copper (II) oxide (Aldrich 99+%)

This material was used both in the methane combustion experiments and as a reference for quantitative temperature programmed reduction analysis. The sample was calcined at ex-situ 800C prior to activity testing.

2.1.12: Molybdenum (VI) oxide (Aldrich 99.5%)

This material was used for comparison with the activity of the supported molybdate samples. The sample was calcined at ex-situ 800C prior to activity testing, at which temperature much of it is volatilised.

2.1.13: α-Alumina (Aldrich 99%)

This material was used as an inert bed in the partial oxidation of methane experiments. The sample was calcined at ex-situ 550C prior to activity testing.

2.1.15: 10wt% Silica supported on zirconium oxide

This material was prepared by M.Keenan[90] and was subjected to high temperature calcination above 800C, and was used as prepared. X-ray diffraction showed this material to be 100% metastable tetragonal phase of zirconia.

2.2: CATALYST CHARACTERISATION

2.2.1: Powder x-ray diffraction

Powder x-ray diffraction was performed using two different diffractometers. Iron based samples were analysed at the University of Loughborough on a Hiltonbrooks modified Philips powder diffractometer fitted with a detector monochromator to

remove fluorescence. All non-iron based samples were analysed on a Hiltonbrooks modified Philips powder diffractometer, at the Nottingham Trent University. Samples were prepared by compaction into a glass backed aluminium sample holder. Iron samples were scanned in the range 5-75° 2θ at a step size of 0.05° with a count rate of 2°/minute. All non-iron based samples were scanned in the range 5-80° 2θ at a step size of 0.02° at a rate of 0.5s per step.

The diffractometers used a CuK_α radiation source (1.5418Å). X-ray generators operated at 40 kV with a set current of 20 mA, for the instrument at the University of Loughborough, and at 42.5kV and a current of 18mA, for the instrument at The Nottingham Trent University.

2.2.2: Surface area determination

Surface areas were measured by the application of BET method to nitrogen physisorption isotherms at liquid nitrogen temperatures. Isotherms were measured using an automated computer controlled gas adsorption system using nitrogen physisorption. Samples were first degassed at 150C for at least one hour to remove adsorbed moisture and adsorbed gases prior to analysis.

2.2.3: Mossbauer spectroscopy

^{57}Fe Mossbauer spectra were kindly recorded by Dr. Q. Pankhurst of the University College London at room temperature using a conventional constant acceleration spectrometer and a ^{57}CoRh source. A double-ramp velocity drive signal was used and the recorded spectra were numerically folded to eliminate any baseline curvature. Calibration was performed with respect to α-iron at room temperature.

2.2.4: Temperature programmed reduction

Temperature programmed reduction (TPR) was performed using an in house designed computerised system, equipped with a thermal conductivity detector. A mass of sample in the range 0.26-013g was packed into a silica glass tube held centrally in the heated zone of a tube furnace. Analysis was performed in a flow of 5% hydrogen in argon (Air Products) at a flow rate of 40 ml/min while the furnace temperature was increased at 5C/min from room temperature to 1000C. The reduction profile was automatically logged to a computer and the hydrogen

consumption was calculated using copper (II) oxide (Aldrich 99+%), under the conditions outlined above.

2.2.5: Transmission electron microscopy

Transmission electron microscopy was performed using a Jeol 2010 electron microscope operating at 200 keV with a lanthanum hexaboride (LaB_6) filament. Samples were prepared by sprinkling onto a carbon coated copper grid 200 mesh 3mm diameter and shaken to remove excess sample. Compositional analysis was performed using energy dispersive x-ray spectroscopy (EDXS), with a lithium drifted silicon detector, operating at 100kV. High resolution transmission electron microscopy, (HRTEM) was kindly performed at the University of Liverpool by Dr. C. Kiely and Mr.M. Edwards. Prior to HRTEM examination, samples were gently ground in ethanol using an agate pestle and mortar. A drop of the resulting slurry was then allowed to evaporate onto a lacy carbon film supported on a copper mesh grid. The samples were examined using a JEOL 2000FX HRTEM operating at 200kV. Energy dispersive compositional mapping was performed using a VG HB601UX scanning tunnelling electron microscope (STEM) equipped with a LINK EDXS operating at 100kV.

2.2.6: Fourier transform infrared spectroscopy

Iron based samples were analysed using a Perkin-Elmer 1600 series FTIR spectrometer scanning in the range 4500 - 450 cm^{-1} (wavenumber), four times at 4.0 cm^{-1} resolution. Molybdenum based samples were analysed on a 750 Nicolet Magna-IR spectrometer fitted with a deuterated triglycine sulfate detector (DTGS) scanning in the range 4500 - 100 cm^{-1}, scanning 4.0 cm^{-1} resolution. Samples were ground in dried potassium bromide (BDH, SpectrosoL), and pressed at 10 tons under vacuum. Far-infrared analysis in the 600 - 100 cm^{-1} region, was performed similarly in caesium iodide (Aldrich spectroscopic grade).

2.2.7: Laser Raman spectroscopy

Laser Raman spectra, kindly performed at the University of Wales College Cardiff by Dr. S.H. Taylor, were recorded on a Renishaw System 100 laser Raman microscope on powdered samples. The spectrometer was a dispersive mode

instrument using an argon ion laser (518 nm), which produces a low power and minimises the effects of catalyst heating.

2.3: CATALYST TESTING

2.3.1: Reactor design

Catalytic performance was evaluated in a standard fixed bed continuous flow micro-reactor. The reactor consisted of pressure gauges, filters, Brooks 5850TR mass flow controllers and non-return valves. The reactor consisted of a 2mm, (1/2"), stainless steel tube with a quartz lining (8.5mm internal diameter), housed in a Carbolite furnace. The exit lines were trace heated using Isopad ITH-75/3 heating tapes to a temperature in excess of 150C to prevent condensation of products. Online analysis was performed using a Varian Saturn 6000 gas chromatogram-mass spectrometer (GC-MS) fitted with a 10- and an 8-port Valco gas sampling injection valves and a thermal conductivity detector (TCD). The 10-port valve was trace heated with Isopad ITH-75/73 heating tape to prevent condensation of products. All chromatograms and peak area integrations were automatically plotted by the GC. The 10-port Valco valve was used for automated injections onto a Megabore Poraplot, GS-Q column (30M x 0.5mm internal diameter) and a GS-Molesieve column, (30M x 0.53mm internal diameter). The first column was used to effect the separation of carbon dioxide and oxygenated products such as methanol, and the second, to effect the separation of carbon monoxide, methane, oxygen and non-polar products such as ethane or ethene. The columns were used in series, where the GS-Molsieve column was switched in and out of series via an 8-port Valco valve to protect the column from water and oxygenated products, which could damage the column.

2.3.2: Experimental procedure

The feed gases were methane (Air Products 99 %), oxygen (Air Products 99.6%) and helium (Air Products 99.999%). Samples were pressed and pelleted in the particle range 0.6-1.0 mm prior to activity testing. The sample volume was 0.75 ml, which corresponds to a mass range of 0.4-1.0g and was packed in the reactor tube and positioned centrally in the heated zone of the tube furnace. Methane partial oxidation experiments were performed with a methane:oxygen:helium flow ratio of 46:4:12 ml/min respectively which gives a gas hourly space velocity of (GHSV) ~4600 h^{-1} at

a pressure of 15 bar, which was maintained using a Tescom back pressure regulator. All experiments under these conditions were performed in the temperature range 250C-550C using at 50C increments. Methane combustion experiments were performed at atmospheric pressure with a methane:oxygen:helium flow rate ratio of 10:40:250 ml/min which produces a GHSV of ~24000 h^{-1}. All experiments under this reactor regime were performed in the temperature range of 600C - 800C. The reactor was allowed to stabilise for an hour at the set temperature prior to data collection. The results are the average of three analyses. From the data produced several parameters were calculated and the equations for which are given in Appendix 1.

3.0: THE APPLICATION OF SULFATED IRON OXIDES FOR THE PARTIAL OXIDATION OF METHANE

3.1: General Introduction

Iron oxide based materials are and have been involved as catalysts for a variety of reactions including high temperature water gas shift, ammonia synthesis, as well as being investigated for a number of oxidation reactions[91-93]. In selective oxidation studies of methane using Fe/ZSM-5 it was found that α-Fe_2O_3 clusters combined with the Bronsted acid sites on the zeolite were responsible for the formation of aromatic hydrocarbons at >85% selectivity at 700C. Anderson and Tsai reported that Cu^+ exchanged FeZSM-5 zeolite containing residual Al is an effective catalyst for converting methane into methanol when using N_2O as oxidant at temperatures in the range 230-350C[94]. The authors stated that Cu-FeZSM-5 was the only active combination for this reaction and that there must be a synergistic effect between the Cu and Fe functions. Similar synergistic influences[95] between copper and iron cation sites were suggested by Sojka et al in their studies on Cu^{2+} and Fe^{3+} doped zinc oxide for the selective oxidation of methane in a temperature range of 500-850C, using air as an oxidant[96]. The authors observed a shift in selectivity from coupling products to carbon dioxide and formaldehyde when zinc oxide was doped with equimolar quantities of both Cu^+ and Fe^{3+}. It was proposed that that this promotional effect was due to redox, ($Cu^{I/II}/Fe^{II/III}$) and Lewis acid (Fe^{III}) functions. These functions were believed to facilitate the surface oxidation of intermediate methyl radicals by a redox process, which produced methoxide species and subsequent hydride ion transfer to the dopant redox couple.

A significant problem in catalytic selective oxidation reactions, is generally the thermodynamic stability of the product which, often over oxidises to carbon oxides and water or other undesired products. In the selective partial oxidation of methane methanol and/or formaldehyde are more reactive than methane. Therefore the oxygenated products formed tend to undergo further reaction, usually to carbon oxides and water. In 1968 Dowden et al[97] studied a series of multi-component molybdenum oxide systems based on the idea of bifunctionalisation. The authors suggested that one component of the catalyst should be a relatively weak dehydrogenation function (suggested d^0, d^1,d^5, d^{10} or possibly d^4 configuration) and a

second component, connected with an n-type oxygen insertion function and suggested TiO_2, V_2O_5, MoO_3, Fe_2O_3 and ZnO, amongst other metal oxide materials. The authors believed that methanol production would also increase relative to formaldehyde since the methylene diol, thought to be produced, and was resistant to further oxidation, at least in aqueous solution. In methane partial oxidation studies Kobayashi et al[98], on 3d transition metals supported on silica found that by supporting 0.05 atom % of Fe^{III} on silica a tenfold increase in the formaldehyde yield was observed. However, supporting similar amounts of Fe^{III} on titania, zirconia and alumina had no effect. The authors described this as a synergistic effect between the highly dispersed iron centres and the support material. Otsuka et al in their investigations of iron, niobium and boron catalysts for the direct partial oxidation of methane at 870C using molecular oxygen at 34 kpa pressure found for their best catalyst, high selectivity to formaldehyde (61.6%) at low methane conversion (2.15%)[99]. The space-time yield for this catalyst was 1210 $g(kg\ cat)^{-1}\ h^{-1}$ the highest yield for any catalyst applied to the partial oxidation of methane known to date. X-ray diffraction studies indicated the presence of three phases, $FeNbO_4$, $FeNb_{11}O_{29}$ and B_2O_3. Through an investigation of the individual phases, the authors found the active phase to be $FeNbO_4$ and proposed that this phase supplied reactive lattice oxygen required for C-H bond cleavage in the formation of formaldehyde. Furthermore, they proposed that the role of boron was to prevent deep oxidation of the products and increased selectivity.

As discussed in the introduction, synergistic effects between the sulfate and the oxide support for sulfated metal oxides, termed "superacids", have been proposed[6]. The basis for the enhancement in activity, as observed by several authors for isomerisation reactions[31,50,51], has been explained in terms of increased acidity when compared to their unsulfated counterpart as a result of this synergism. However, there application to oxidation reactions has not been widely investigated with only few examples pertaining to zirconium based sulfated oxides. Murata et al[100], found that lithium doped sulfated zirconia was an active catalyst for oxidative coupling of methane at atmospheric pressure at 800C using molecular oxygen. Only slight differences in methane conversions, (16-17%), and combined product selectivities for C-2 hydrocarbons (ethane, ethene and ethyne, 18.3%) were observed for the sulfated and non-sulfated zirconia samples respectively. Doping lithium on sulfated

zirconia produced a twofold increase in methane conversion (32.1%), and a four-fold increase in the selectivity towards C-2 hydrocarbons. The authors concluded that the activity was dependent upon sulfate content and calcination temperature. The optimum preparation method reported, consisted of a 6wt% sulfated zirconia, which had been calcined at 650-700C, in accordance with many literature methods[6,12]. It is generally considered that the apparent strong acidity of these materials results in their high catalytic activity, however it is apparent that these materials also possess redox behaviour. Oxidative activity of sulfated metal oxides was first reported by Jaitia et al[31], in their attempts to measure the acidity of iron/manganese/sulfated zirconia, believed to be the strongest solid "superacid" prepared to date[61,62]. In their studies using temperature programmed desorption coupled with a mass spectrometer for benzene adsorption, the authors observed peaks corresponding to carbon and sulfur dioxides, which was identified as decomposition products of benzene. During detailed investigations by Farcasiu et al deduced a one-electron transfer model when benzene was adsorbed on sulfated zirconia at 100C, observing only hydroxylated products of adamatane[57]. Although the enhancement in activity with sulfated metal oxides is unquestionable, the main problem is these materials deactivate rapidly. Cheung et al observed this occurrence in studying iron/manganese/sulfated zirconia for methane conversion in a temperature range of 400-450C, using dinitrogen and methane at 100 kPa[101]. The authors found a low conversion of methane <0.15% to ethene and acetylene, with rapid deactivation, within a couple of hours on stream. The authors proposed two mechanisms, firstly, methane was protonated by a minority of very strong acid sites and that this protonated species undergoes oligocondesation reactions to give the observed product. Alternatively a redox behaviour by the iron to initiate a carbocation intermediate as an iron oxide species was observed in their previous work.

Industrial applications of sulfated metal oxides are limited, with a recent patent by the Sun Oil company for the non-oxidative dehydrogenation of saturated or partially saturated hydrocarbons giving isobutane to isobutylene as an example over sulfated zirconia[9,10]. Much of the recent research on sulfated metal oxides has been concentrated on zirconia based materials; to date sulfated iron oxide has not been studied in oxidative reactions. In this study sulfated iron oxides, due to their redox behaviour and the apparent strong acidity brought about by sulfation, were

investigated for the partial oxidation of methane. Further it may be considered that the activity of sulfated iron oxide may depend on the morphology of the iron oxyhydroxide/hydroxide precursor. Several polymorphs of iron precursors are known and these were prepared as described previously, Chapter 2. Sulfated and non-sulfated iron oxides prepared from their corresponding precursors were examined for their catalytic performance for the partial oxidation of methane.

3.2: Results and Discussion

3.2.1: Reactor Studies

Table 1 shows the catalytic performance of the non-sulfated iron oxides, the empty reactor tube and α-alumina, which was considered to be an inert material and was used to determine the background gas-phase activity. A general trend of high selectivity to carbon dioxide, the major product, was observed with all the non-sulfated iron oxides tested. Methane and oxygen conversions for all the iron oxides were in excess of the background, indicating that the observed activity was due to the materials and not purely as a result of the homogeneous gas-phase activity, which is known and was observed to be considerable for this reaction[102]. However differences between non-sulfated iron oxides were observed. Goethite derived non-sulfated iron oxide was observed to be the most active sample with the onset of carbon dioxide, evident at 300C. The least active sample was non-sulfated iron oxide derived from 2-line ferrihydrite, which began producing carbon dioxide exclusively at 400C, 100C higher than goethite derived non-sulfated iron oxide. The differences in activity between the samples, maybe as a result of morphology, which will be elaborated upon in further sections. Carbon monoxide was only observed with iron oxide derived from goethite at temperatures above 450C. This maybe as a consequence of the higher oxygen consumption limiting molecular oxygen in the feed and/or the consecutive oxidation of reaction products such as ethane or C-2 hydrocarbons. From an inspection of oxygen demand given in Table 1, it is possible to speculate which reaction pathways are operative for the formation of the observed products and whether consecutive oxidation of intermediate products occurs. Oxygen demands, given in Table 1, were based on reactions given in equations (1-2), while possible consecutive conversion routes are given in equations (3-5).

Primary oxidation routes

$CH_{4(g)} + 2O_{2(g)} \longrightarrow CO_{2(g)} + 2H_2O_{(g)}$ Eqn 1

$CH_{4(g)} + 1.5O_{2(g)} \longrightarrow CO_{(g)} + 2H_2O_{(g)}$ Eqn 2

Secondary oxidation routes

$C_2H_{6(g)} + 2.5O_{2(g)} \longrightarrow 2CO_{(g)} + 3H_2O_{(g)}$ Eqn 3

$C_2H_{6(g)} + 3.5O_{2(g)} \longrightarrow 2CO_{2(g)} + 3H_2O_{(g)}$ Eqn 4

$CO_{(g)} + H_2O_{(g)} \longrightarrow CO_{2(g)} + H_{2(g)}$ Eqn 5

Table (1): Reactor data for non-sulfated iron oxides.

Empty Tube

Temperature/C	Conversion[a] (%)		Selectivity[b] (%)			Carbon Balance[c] (%)
	methane	oxygen	carbon dioxide	Carbon monoxide	methanol	
450	2.6	22.8	22	68	10	102
500	8.5	98.9	9	80	11	101
550	8.2	98.1	9	81	10	101

α-Alumina

Temperature/C	Conversion[a] (%)		Selectivity[b] (%)			Carbon Balance[c] (%)
	Methane	oxygen	carbon dioxide	Carbon monoxide	methanol	
450	0.4	2.5	60	40	-	97
500	0.6	12.9	100	-	-	97
550	1.6	19.8	63	37	-	97

Non-sulfated iron oxide derived from 2-line ferrihydrite.

Temperature/C	Conversion[a] (%)		Selectivity[b] (%)			Carbon Balance[c] (%)	Oxygen Balance[d] (%)
	methane	Oxygen	carbon dioxide	Carbon monoxide	methanol		
400	0.7	16.4	100	-	-	101	95
450	0.8	15.6	100	-	-	102	99
500	1.0	20.4	100	-	-	103	97
550	1.3	26.8	100	-	-	102	97

[a,b,c,d] See appendix 1 for definition

Table (1) continued: Reaction data for non-sulfated iron oxides

Non-sulfated iron oxide derived from goethite.

Temperature/C	Conversion[a] (%)		Selectivity[b] (%)			Carbon Balance[c] (%)	Oxygen Balance[d] (%)
	methane	Oxygen	carbon dioxide	carbon monoxide	methanol		
300	0.1	1.3	100	-	-	101	100
350	0.6	14.2	100	-	-	101	97
400	4.0	73.5	100	-	-	100	104
450	4.3	71.4	97	3	-	101	111
500	5.6	71.9	89	11	-	99	133
550	6.8	68.4	75	25	-	97	142

Non-sulfated iron oxide derived from the Arata method.

Temperature/C	Conversion[a] (%)		Selectivity[b] (%)			Carbon Balance[c] (%)	Oxygen Balance[d] (%)
	methane	oxygen	carbon dioxide	carbon monoxide	methanol		
350	0.4	5.4	100	-	-	101	102
400	2.0	32.7	100	-	-	101	102
450	2.0	32.2	100	-	-	100	102
500	2.2	35.6	100	-	-	101	102
550	2.7	37.8	100	-	-	99	110

[a,b,c,d] See appendix 1 for definition

Equations 3 and 4 could be written similarly for the combustion of other possible products such as methanol or formaldehyde. Hence a value of 100% indicates that the formation of carbon dioxide and carbon monoxide follows the reaction pathway indicated in equations 1 and 2 respectively. A value below 100% can indicate production of products, which are not detected. A value above 100% therefore, indicates a non-oxidative secondary route is being followed as given in equation 5. Equation 5 is the water gas-shift reaction (WGS). It is known that iron oxide based materials are effective for this reaction and that the formation of carbon monoxide becomes thermodynamically more favourable at higher temperatures. From Table 1, it appears, with the exception of non-sulfated iron oxide derived goethite, the oxygen demand values are close to those expected on the basis of equations 1 and 2. However, in the case of goethite derived iron oxide, higher reaction temperatures are associated with oxygen demands greater than 100% and carbon monoxide is produced. Therefore a less oxygen consuming route, for the formation of carbon oxides may be in operation for this sample. Since no other reaction products were observed then it may be proposed that the WGS reaction, given in equation 5, may be operative which is a non-oxidative pathway to the formation of carbon monoxide. Similarly a reaction pathway which consumes less oxygen than those given in equations 1,3 and 5 may also be operative. One such reaction could be the catalytic partial oxidation of methane (CPO) given in equation 6 below.

CPO Reaction

$$CH_{4(g)} + 0.5O_{2(g)} \longrightarrow CO_{(g)} + H_{2(g)} \quad \text{Eqn 6}$$

However, differentiating between these two possible reaction routes is difficult since hydrogen could not be detected under the analysis conditions employed in this study. Water-gas shift reaction would require the initial formation of carbon monoxide, which was not observed at lower reaction temperatures. However, it may be possible that the WGS reaction occurs simultaneously with carbon monoxide formation. Therefore CPO reaction may be more likely for non-sulfated iron oxide derived from goethite. Recalculating oxygen balances based on equation 6 does not lower the oxygen demands significantly, 450C(109%), 500C(127%) and 550C(132%). Therefore without the analysis of hydrogen and/or water it is difficult to determine a

reaction pathway, indeed a combination of reaction pathways may well be operative over non-sulfated iron oxide derived from goethite. The absence of water-gas shift behaviour in the other non-sulfated iron oxides may be due to lower methane and oxygen conversions even at the higher temperatures since only carbon dioxide is observed as products, or may relate to morphology differences.

The catalytic activity of the sulfated materials is summarised in Table 2. Activities of sulfated samples were generally observed to begin at 100C higher than their non-sulfated counterparts, with the predominant formation of carbon monoxide. At the initial temperature of activity, methane and oxygen conversions are significantly lower due to the suppression in oxidation behaviour by sulfate incorporation. Above this temperature carbon dioxide is observed as a minor product and oxidation activity is increased with methane and oxygen conversions higher than those of their non-sulfated counterparts. The exception to this was iron oxide derived from goethite, where oxygen and methane conversions become comparable to the non-sulfated counterpart above 450C. Further, carbon dioxide was also observed at temperatures below 450C. Partial oxidation products, particularly methanol, and, in some cases C-2 hydrocarbons were also observed at temperatures in the range 450-500C for the sulfated materials. An exception was sulfated iron oxide derived from lepidocrocite, where only carbon monoxide and carbon dioxide were observed. In this case methane and oxygen conversions were much lower than for the other samples.

Oxygen demands were calculated for all samples, based on equations 1-2 given above and equations 7-9, given below, for the formation of methanol, ethane and ethene.

Equations 7-9: The formation of methanol and C-2 products

$$CH_{4(g)} + 0.5O_{2(g)} \longrightarrow CH_3OH_{(g)} \quad \text{Eqn. 7}$$

$$2CH_{4(g)} + 0.5O_{2(g)} \longrightarrow C_2H_{6(g)} + H_2O_{(g)} \quad \text{Eqn. 8}$$

$$2CH_{4(g)} + O_{2(g)} \longrightarrow C_2H_{4(g)} + 2H_2O_{(g)} \quad \text{Eqn. 9}$$

Table (2): Reactor data for sulfated iron oxides.

Sulfated iron oxide derived from goethite.

Temperature /C	Conversion (%)		Selectivity[a] (%)				Carbon Balance (%)	Oxygen Balance (%)
	methane	oxygen	carbon dioxide	Carbon monoxide	methanol	ethane		
400	0.4	9.2	16	84	-	-	99	97
450	1.3	29.5	36	64	-	-	99	91
500	5.9	85.0	32	61	4	3	98	100
550	6.6	82.7	82	15	-	3	99	129

Sulfated iron oxide derived from 2-line ferrihydrite

Temperature /C	Conversion (%)		Selectivity[a] (%)				Carbon Balance (%)	Oxygen Balance (%)
	methane	oxygen	carbon dioxide	Carbon monoxide	methanol	Ethane		
450	0.2	4.8	-	100	-	-	100	97
500	7.3	95.6	16	77	3	4	96	96
550	7.3	96.6	18	75	-	7	95	99

Sulfated iron oxide derived from the Arata method.

Temperature/°C	Conversion (%)		Selevtivity[a] (%)					Carbon Balance (%)	Oxygen Balance (%)
	methane	oxygen	carbon dioxide	carbon monoxide	methanol	Ethane	ethene		
450	0.4	6.5	8	92	-	-	-	103	99
500	10.1	99.0	16	71	6	7	-	100	120
550	13.0	92.2	16	68	5	11	1	97	165

. [a,b,c,d] See appendix 1 for definition.

Table (2): Reactor data for sulfated iron oxides.

Sulfated iron oxide derived from lepidocrocite

Temperature/C	Conversion (%)		Selectivity[a](%)			Carbon Balance (%)	Oxygen Balance (%)
	methane	oxygen	carbon dioxide	Carbon monoxide	methanol		
400	0.3	5.7	-	100	-	100	98
450	3.0	36.6	30	70	-	98	96
500	3.1	44.7	100	-	-	99	707
550	4.0	47.9	86	14	-	98	118

Sulfated iron oxide derived from the ferroxhyte.

Temperature/C	Conversion[a] (%)	Selevtivity[b] (%)				Carbon Balance[c] (%)	Oxygen Balanced[d] (%)
	methane	oxygen	carbon dioxide	carbon monoxide	methanol		
350	0.3	5.9	-	100	-	99	98
400	1.9	11.5	7	93	-	102	114
450	3.6	56.3	35	63	-	103	96
500	4.9	80.4	100	-	2	100	105
550	8.3	78.7	68	27	-	97	152

[a,b,c,d] See appendix 1 for definition.

From the catalytic activity data Tables 1 and 2, it is observed that selectivities to carbon dioxide were higher than their non-sulfated counterparts at temperatures ca.400C and above. An amount of carbon monoxide was also observed for all the sulfated iron oxides, the selectivity of which generally increased with increasing reaction temperature. However the amount of carbon dioxide observed differs between the sulfated samples, and appears to be a function of oxygen conversion. Generally it was observed that oxygen demands for the sulfated iron oxides were greater than 100%, particularly at the higher reaction temperatures. The exception being sulfated iron oxide derived from 2-line ferrihydrite, where oxygen demands were ca. 100%. Oxygen demands greater than 100% were associated with high oxygen conversions. This may relate, in part, to the observations discussed previously with non-sulfated iron oxide derived from goethite. However, the presence/absence of carbon monoxide is less clear with the sulfated materials, i.e. carbon monoxide is observed even when the oxygen demands are ca.100%. Similarly, the increased oxygen demand values, given in Table 2, could be due to WGS or CPO. Further the formation of carbon oxides could proceed via the consecutive combustion of reaction products, which are observed at temperatures ca.500C and above.

e.g.: $CH_{4(g)} + 0.5O_{2(g)} \longrightarrow CH_3OH_{(g)} \longrightarrow CO_{(g)} + 2H_{2(g)}$ Eqn 10

A general and interesting feature in Table 2, is the decrease in the oxygen demands at ca. 450C, particularly for sulfated iron oxide derived from goethite. The decreased oxygen demands at this temperature are not associated with increased oxygen or methane conversions nor are they associated with increases/decreases in carbon oxides selectivities. This indicates that oxygen is being consumed by an oxidative reaction pathway not taken into account by the stoichiometry of equations 1,2 and is not sample specific. This may be related to the production of for example, formaldehyde or partial or complete sulfate decomposition at this temperature. The formation of partial oxidation products at 500-550C for methanol, ethane and ethene may occur as a result of equations 7-9 given above and are associated with high oxygen conversions.

It is acknowledged that for the oxidation of methane many other equations exist, some of which may be discounted on the basis of kinetic limitations such as the reaction of methane with water equation 11, which although thermodynamically favourable requires temperature above 800C.

$$CH_{4(g)} + H_2O_{(g)} \longrightarrow CO_{(g)} + 3H_{2(g)} \qquad \text{Eqn 11.}$$

Therefore the equations used in the above discussion were selected based on simplicity and kinetic feasibility.

Specific activity

Tables 3 and 4 show the specific surface area and specific activity with per pass yields for methanol, for sulfated and non-sulfated samples, respectively. From Table 3 it is observed that the surface areas of the non-sulfated materials are less than their sulfated counterparts. However surface areas for the non-sulfated materials are dependent upon the precursor oxyhydroxide/hydroxide, since the percentage decrease in surface area, compared to their precursors, is not constant.

Table 3: BET surface areas of precursors, sulfated and non-sulfated iron oxides using N_2 adsorbate at 77K

Sample	Precursor Surface Area m^2/g	Unsulfated Iron Oxide Surface Area m^2/g	Sulfated Iron Oxide Surface Area m^2/g
Goethite	40	13	29
2-Line Ferrihydrite	234	15	73
Ferroxyhyte	143	36	70
Lepidocrocite	100	22	41
Arata	271	17	50

Indeed the percentage reduction in surface area is similar, ca. 94%, for both the Arata and 2-line ferrihydrite samples. This may be expected on the basis of their similar methods of preparation, see Chapter 2.

The incorporation of sulfate stabilises the surface area of all the samples examined. However, with the exception of lepidocrocite derived sulfated iron oxide, there is a linear relationship between the percentage of surface area reduced, after sulfate addition and calcination at 550C, and the initial surface area of their precursors. Therefore if sulfate alone is responsible for the stabilisation of surface area of the sulfated materials, relative to the precursor surface area, there should appear to be a direct relationship between the percentage of sulfate uptake and the percentage increase in surface area. However it is known that sulfate content may be reduced at temperatures of ca.600C.

The problems of reproducibility associated with SMO materials, in terms of their catalytic activity, have been observed by several authors[103]. Farcasiu et al suggested that problems of reproducibility were associated with sulfate uptake[104]. These authors proposed a more controlled method of sulfate addition for sulfated zirconia by impregnating the solid with the desired amount of sulfuric acid in water, evaporating the solvent, and calcining the residue. This produced sulfated zirconia materials with a standard deviation of 0.08 for a ca.1.58wt% loading of sulfate. The surface areas of the sulfated materials were also related to the uptake of sulfate. However, reproducibility may also be related to the adsorption of water by the precursor during storage[6].

Table 4: Specific activity and per pass yield data for sulfated and non-sulfated iron oxides at 500C

Sample	Specific Activity/ $moles_{CH4\ converted}\ min^{-1}\ m^{-2}$		Per Pass Yield for Methanol (%)
	Sulfated Iron Oxide	Non-Sulfated Iron Oxide	Sulfated Iron Oxide
Goethite	4.82	4.88	0.35
2-Line Ferrihydrite	3.66	1.80	0.26
Arata	4.66	2.82	0.64
Feroxyhyte	1.75	-	0.08

Specific activity data, calculated in Table 4, shows the specific activity of non-sulfated iron oxide derived from goethite is approximately twice that of the other samples. Further addition of sulfate to this precursor does not significantly affect its specific activity. However, this remains the most active sample in comparison with the other sulfated iron oxide samples. In comparison the addition of sulfate to the other precursors significantly increases their specific activities. Sulfated iron oxide derived from 2-line ferrihydrite shows the largest increase in specific activity, with approximately a twofold increase.

In view of the comparative performances of sulfated and non-sulfated samples (Tables 1-4) a two site mechanism is proposed in which those sites active at lower temperatures are poisoned by sulfated addition, whilst those active at higher temperatures are promoted. Partial oxidation products at suitable temperatures and levels of oxygen conversion are related to the high temperature site. In summary, the differences in activity between the non-sulfated iron oxides are related to their precursors and a structure function relationship can be inferred. The variations in activity between the sulfated iron oxides can be explained in terms of the precursor and/or the degree of sulfate uptake/retention.

3.2.2: X-Ray diffraction

The x-ray diffraction profiles of non-sulfated and sulfated iron oxides, prior to activity testing shows the phase to be haematite (JCPDS 33-664) in all cases, Figures 1 and 2 respectively.

Figure 1: Powder x-ray diffraction patterns of pre-reactor non-sulfated iron samples

Non-sulfated iron oxide derived from goethite precursor

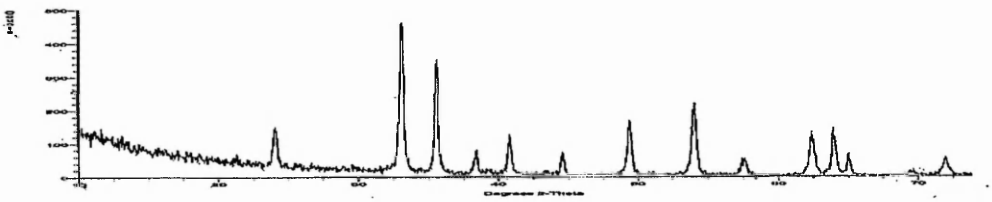

Figure 1 continued: Powder x-ray diffraction patterns of pre-reactor non-sulfated iron oxides

Non-sulfated iron oxide derived from lepidocrocite precursor

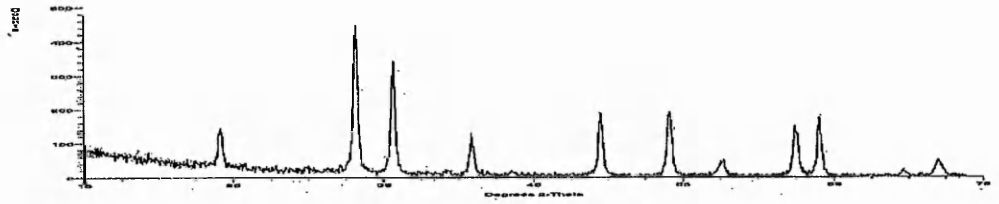

Non-sulfated iron oxide derived from feroxyhyte precursor

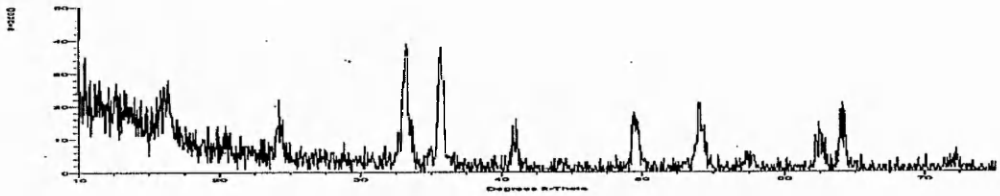

Non-sulfated iron oxide derived from 2-line ferrihydrite precursor

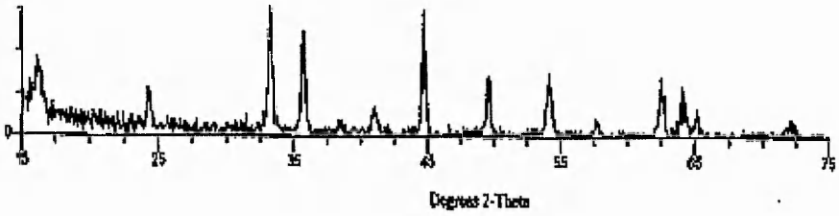

Non-sulfated iron oxide derived from Arata precursor

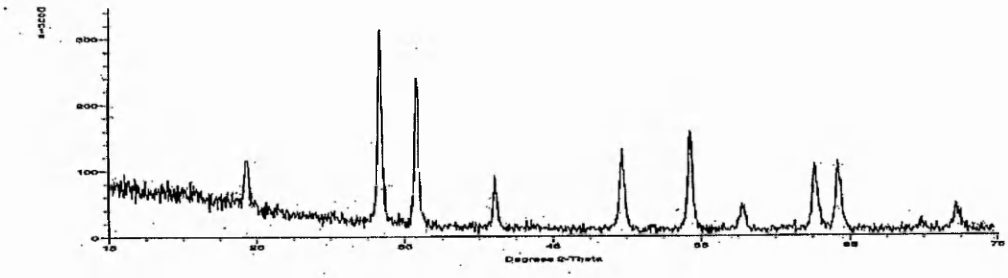

Figure 2: Powder x-ray diffraction patterns of pre-reactor iron oxides

Sulfated iron oxide derived from goethite

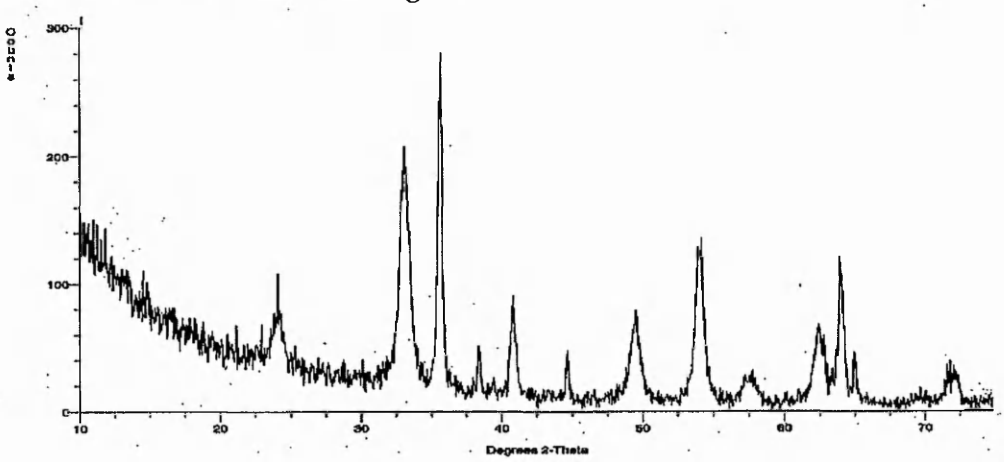

Sulfated iron oxide derived from 2-line ferrihydrite

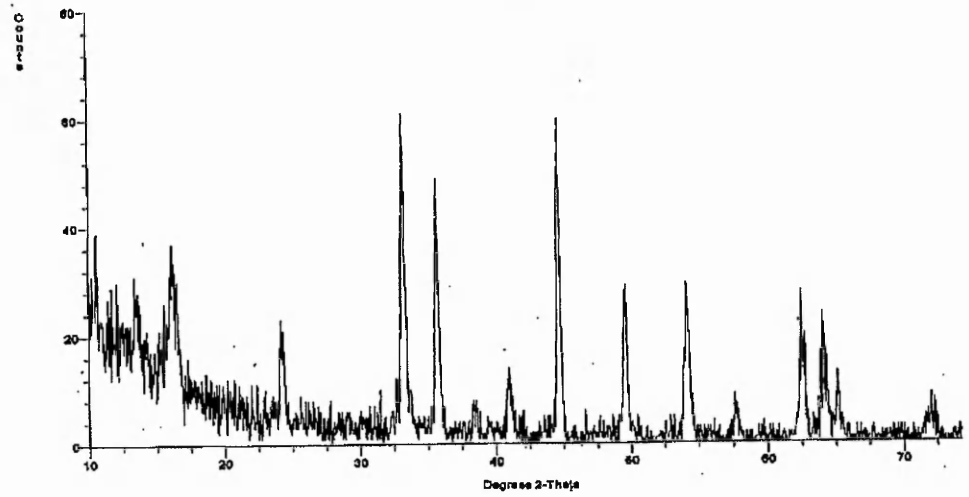

From Table 5 it is apparent that there are differences in the full width half maxima (FWHM) for the reflections relating to (104), (110), (024), (116), (214) and the (300) planes. Broad reflections may be indicative of smaller crystallite (or diffracting domain) size, degree of structural disorder and or lattice strain effects. Table 5 relates to the trend observed in the differences in the x-ray line widths to the position of the reflections for the non-sulfated iron oxides, and follow a similar trend with the measured surface areas. Iron oxide derived from feroxyhyte having the largest surface area and the overall broadest reflection widths, while non-sulfated iron oxide

derived from goethite has the smallest surface area and the overall smallest reflection widths.

Further, it is observed from Table 5 that both goethite and lepidocrocite derived iron oxides show similar widths while their surface areas differ. However, there is a significant contribution from the (300) plane, which is significantly narrow. This may also affect the crystallite sizes calculated in Table 5 and discussed later in this section.

Table 5: Crystallite sizes and FWHM of non-sulfated iron oxides

	Goethite derived iron oxide		2-line ferrihydrite derived iron oxide		Lepidocrocite Derived iron oxide		Feroxyhyte derived iron oxide	
Reflection	Size (Å)	Width degree[a] (2θ)	Size (Å)	Width degree[a] (2θ)	Size (Å)	Width degree[a] (2θ)	Size (Å)	Width degree[a] (2θ)
(104)	305	0.30	458	0.20	367	0.25	458	0.20
(110)	462	0.20	308	0.30	370	0.25	370	0.25
(024)	386	0.25	322	0.30	322	0.30	193	0.50
(116)	329	0.30	247	0.40	395	0.25	197	0.50
(214)	513	0.20	256	0.40	410	0.25	147	0.70
(300)	518	0.20	259	0.40	691	0.15	173	0.60
Average	**419**	**0.24**	**308**	**0.33**	**426**	**0.24**	**265**	**0.54**

[a] reflection widths not corrected for instrumental broadening.

Although all the materials are the α-Fe_2O_3 phase, broadening of their FWHM have been reported in the literature to be as a consequence of microstrains, in the case of feroxyhyte derived haematite[105], and stacking faults in the hexagonal close packed lattice for haematite derived from lepidocrocite[106,107]. However these reports relate to the use of low temperature, usually <400C, for their conversion to haematite.

In this study the differences in FWHM for the differently prepared hematites are as a direct result of their surface area or morphological differences since all samples were calcined at the same temperature of 550C. X-ray line broadening associated with haematite prepared from goethite and 2-line ferrihydrite have been similarly investigated and will be discussed more fully below. Crystallite sizes given in Table 5, calculated for the non-sulfated iron oxides calculated from the Scherrer equation

given in equation 12, shows a 40% variation in the average crystallite sizes between 270-420Å.

$$d = k\lambda/b\sin\theta \qquad \text{Eqn. 12}$$

where, d = Average crystallite size

k = Constant (0.9)

b = Width (2θ)

θ = Bragg angle

and λ = Wavelength of x-ray source

The effect of sulfate addition to iron oxides can be seen in their x-ray diffraction patterns. A general increase in FWHM is observed, which is indicative of smaller crystallite (or diffracting domain) size and may at least in part explain the differences in surface areas measured for the sulfated iron oxide samples.

However it is also observed that sulfation decreases markedly the crystallinity of goethite derived iron oxide, as expected on the basis of increased surface area, but unexpectedly increases crystallinity in the case of 2-line ferrihydrite derived iron oxide. An indication of the degree of crystallinity may be given by examination of the intensity ratios of the 110/104 planes. Schwertmann and Cornell[89] indicated that for a well crystallised haematite sample this ratio is 0.70. A comparison of these ratios for goethite derived iron oxide gives 0.75 for unsulfated iron oxide, the most crystalline iron oxide sample, and 1.50 for sulfated iron oxide, the least crystalline iron oxide sample, indicating a greater degree of amorphous content. Iron oxide samples derived from 2-line ferrihydrite produce the reverse trend of 0.83 for non-sulfated iron oxide and 0.80 for the sulfated iron oxide sample indicating only a slight increase in crystallinity. It is evident that by inspection of the x-ray patterns and the calculated ratios that there is a varying degree of amorphous material associated with both the sulfated and the non-sulfated iron oxide samples. It may be proposed that the degree of amorphous content may have a contributing effect on catalytic activity. It should be noted that by taking the intensity ratio of the 110/104 planes, effects such as preferential orientation may occur, where crystallite orientations are not random, particularly for acicular crystals.

Table 6 shows FWHM for sulfated and non-sulfated iron oxide samples derived from goethite. It is observed that particular reflections namely (104), (024), (116), (018) and the (1010/(119) are preferentially broadened. Instrumental line broadening, where the alignment of the x-ray diffractometer can change can produce x-ray line broadening. This possibility can be discounted since all the samples tested on the same day on the same diffractometer.

Table 6: Powder x-ray diffraction line widths for pre-reactor non-sulfated and sulfated haematite derived from goethite

Reflection	Width (2θ)[a]	
	H_2O/Fe_2O_3	SO_4^{2-}/Fe_2O_3
(012)	0.35	0.50
(104)	0.30	0.70
(110)	0.20	0.30
(006)	0.15	0.30
(113)	0.30	0.40
(202)	0.30	0.20
(024)	0.25	0.70
(116)	0.30	0.60
(018)	0.40	1.00
(214)	0.20	0.50
(300)	0.20	0.15
(1010)/(119)	0.25	1.00

[a]Reflection widths not corrected for instrumental broadening.

Anisotropic reflection width effects on iron oxides have been observed in the literature, the cause of which is currently an area of much debate[108]. Consequently there are several explanations given to the observed effect. Studies by Rooksby et al on the transformation of acicular goethite to haematite, observed non-uniform x-ray line broadening, which was assigned to the particular shape of the iron oxide crystals[109]. In further work the same authors proposed another explanation based on a disordered transitional state, which on further heating resulted in a completely ordered haematite[109]. Further investigations into the nature of the anomalous x-ray

line broadening was investigated by Lima-de-Faria, using both single and crystal and powder x-ray diffraction[110]. The observed anisotropic line broadening effects was related to stacking fault effects in the packing of the oxygen sub-lattice caused by the loss of water at localised positions in the dehydroxlation stage on the initial thermal transformation. It was also noticed that "holes" formed in the structure, presumably by the evolution of water, although the possible effect in causing the x-ray line broadening was not commented upon. Derie et al, observed similar "holes" which were described as long-slit pores[108]. These studies involved the preparation of several morphologies of goethite ranging from colloidal, tabular and acicular and observing the effects of the thermal transformation to haematite at 300-600C using powder x-ray diffraction and transmission electron microscopy. Similar anomalous x-ray line width broadening to that reported by Lima-de-Faria was observed in acicular goethite. Further the authors acknowledged that there may be an effect from stacking faults[108]. However the (110) and (116) planes were also broadened, which if stacking faults alone were the cause should not occur. From their investigations the authors proposed that the observed x-ray line broadening was as a result of morphology i.e., the aspect ratio of the crystal (crystal thickness:crystal width). In the work by Naona et al[111] anomalous x-ray broadening were assigned to the formation of unformed slit shaped pores (0.8nm in width). Yamaguchi and Tasahashi, in calcining α-FeOOH (goethite) in the temperature range 300-900C reported a temperature dependence associated with the (012), (104), (024) and (018) planes, which were associated with the diffraction intensity contributed more strongly by iron atoms than by oxygen atoms[112]. These reflections appeared broadened at low temperatures in comparison with (116), (300), (110), and the (113) planes, which were observed to be temperature independent. The authors found a good correlation of the broadened reflections to the modulus of the structure factor for iron and oxygen in haematite. They proposed that low temperature decomposition of α-FeOOH yielded α-Fe_2O_3 where the iron atoms are not displaced to their equilibrium lattice positions, producing broader reflections from the planes associated with iron atoms. They attributed this to the topatactic mechanism in the thermal transformation of goethite to haematite. In this study the incorporation of sulfate enhances the effects observed by others and transmission electron microscopy

(reported later in this chapter) indicates that the effect is not simply related to the aspect ratio.

3.2.3: Mössbauer spectroscopy of goethite derived samples

Mössbauer spectroscopy of sulfated and non-sulfated iron oxide derived from goethite calcined at 550C and also at a lower temperature of 350C where the anisotropic line broadening effects are enhanced, as shown in Figures 3 and 4, was performed and interpreted by Dr.Q. Pankhurst at University College London. Adam Baker, a final year undergraduate project student, prepared the goethite sample calcined at 350C independently[113]. Mossbauer spectroscopy confirmed the phase of all samples to be haematite. The spectra of the samples, shown in Figure 3, are dominated by a hyperfine magnetic sextet with line positions that are close to those of a well crystallised haematite. However, unlike a well crystallised haematite sample, the absorption lines are broad, and to varying degrees show asymmetries, which are indicative of disordered environments for Fe atoms, leading to distributions in the local hyperfine parameters experienced at the Fe nuclei.

Figure 3: Mossbauer spectra of goethite and iron oxide derived samples

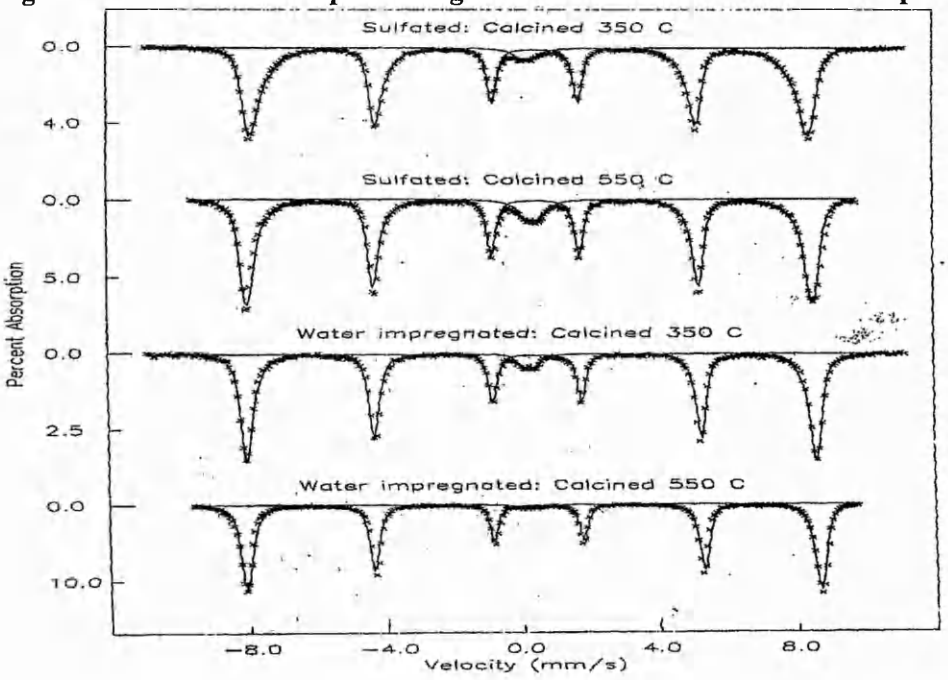

The spectra were analysed in terms of a 40-box smoothed probability distribution of hyperfine fields. As a first approximation several simplifying assumptions were made. The isomer shifts and quadrapole splittings of all the subspectra for a given sample were constrained to be equal. The line widths of the component sextets were set to 0.28 mms^{-1}, which is an experimental estimate of the natural line widths. The relative areas of the outer to middle to inner pairs of lines in the sextets were constrained to 3:2:1, as appropriate for powder absorbers with no preferential alignment of crystallites. Finally, in addition to a smoothing criterion on the probability distribution, the fits were subject to an end-point constraints.

Figure 4: Hyperfine field distributions for sulfated and non-sulfated iron oxides derived from goethite calcined at 350C and 550C

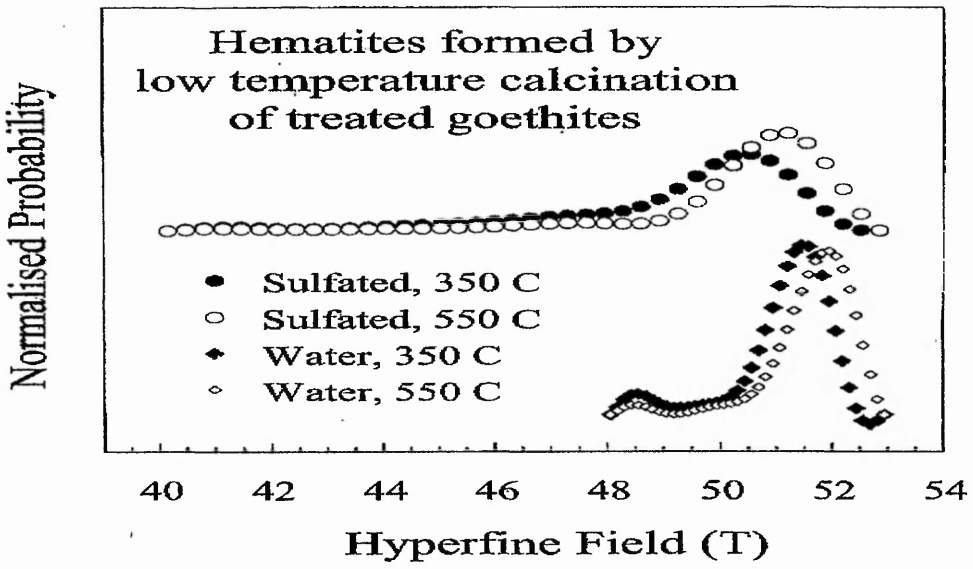

The hyperfine field distributions obtained are shown in Figure 4. These distributions verify that which is apparent from inspection of the spectra, firstly that samples calcined at 550C were less disordered than the samples calcined at 350C and secondly that sulfated samples produced haematites with a greater disorder than the water impregnated counterparts. Although on the basis of Mossbauer evidence alone it is difficult to determine the nature or location of the disorder in the haematite samples, the data obtained is consistent with distortions in hyperfine field brought about by the presence of sulfur atoms adjacent to Fe atoms. Given the smooth shapes

of the observed hyperfine field distributions this may most likely entail interstitial or substitutional defects, rather than a more macroscopic defect structure which would be more likely to give rise to phase separation and the presence of distinguishable sites in the Mossbauer spectra.

Figure 5: Powder X-ray diffraction patterns of non-sulfated iron oxides derived from goethite calcined at various temperatures

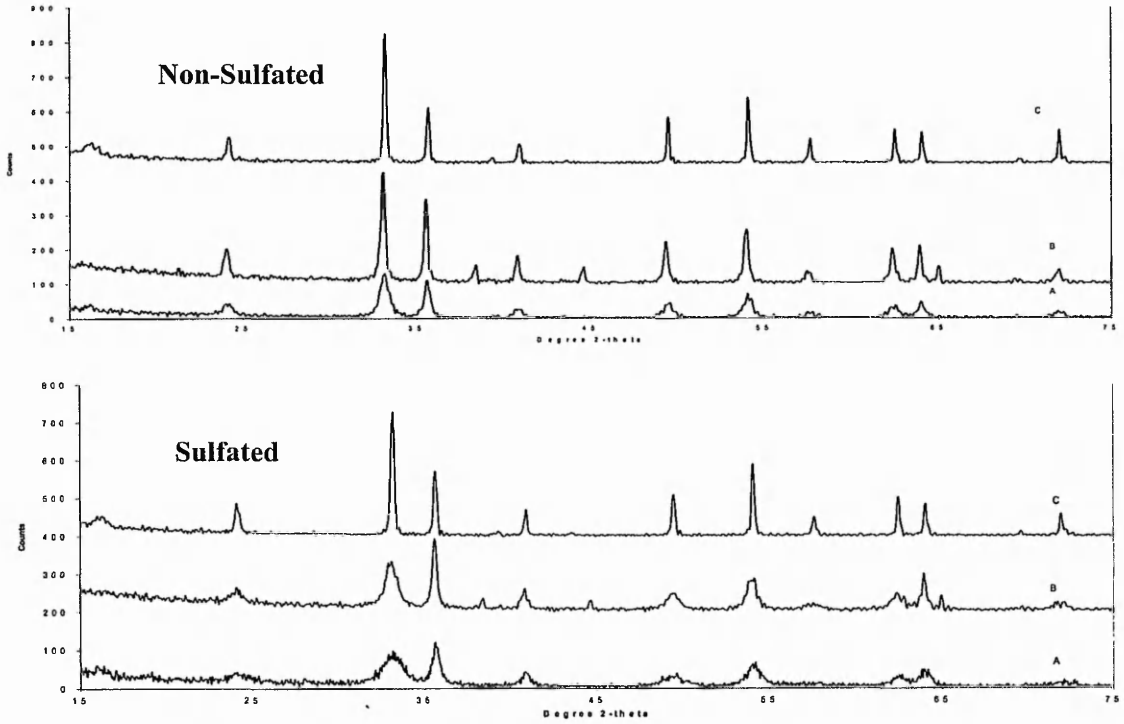

Iron oxide samples derived from goethite calcined at (A) 350C, (B) 550C and (C) 750C for 3 hours in static air.

In all four samples it is also observed that there is a small paramagnetic component that appears as a broad singlet or doublet near zero velocity. The most likely explanation for this is a fraction of the sample existing in very small crystallites that are undergoing superparamagnetic relaxation at room temperature. For haematite the critical dimension for this is 8nm.

A comparison of the powder x-ray diffraction patterns of iron oxide samples derived from goethite shown in Figures 5, above shows clearly the effect of sulfate addition with anisotropic x-ray line broadening observed. The anisotropy observed is also shown in Figures 5 to be a function of calcination temperature and diminishes at higher calcination temperatures, i.e. 750C.

3.2.4: Fourier Transform Infrared spectroscopy

The infrared spectrum of goethite Figure 6, showed two intense bands at ca. 3425 and 3166 cm^{-1} which correspond to the hydroxyl, (O-H), stretching vibration. These bands are consistent with the spectra of goethite given by Schwertmann and Cornell[89]. However the intensity of the first band is higher than that reported. The increased intensity of this band may be related to the KBr, which was used to prepare the samples and has an infrared band at ca. 3440cm^{-1}. The infrared spectra of 2-line ferrihydrite, Figure 7, showed only one very broad feature at ca.3372cm^{-1}, which may indicate the heavily hydrated nature of this precursor[89]. On the addition of distilled water to goethite, Figure 6, a slight shift in one of the bands, observed in the hydroxyl region, by ca.7 cm^{-1} to 3159cm^{-1} while the first band remains approximately constant. Similarly water adsorbed on 2-line ferrihydrite, Figure 7 showed the appearance of two broad bands at 3472cm^{-1} and 3143cm^{-1} in the hydroxyl region. These bands may be related to structural Fe-O-H groups and adsorbed water molecules. On addition of sulfate to both precursors, Figure 6 and 7, it was observed that four bands characteristic of sulfate binding with a C_{2v} symmetry in the region ca. 1200-900 cm^{-1} appeared.

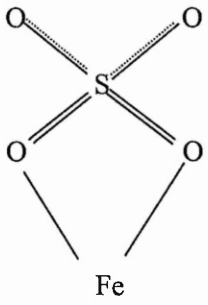

Chelating Complex
(C_{2v})

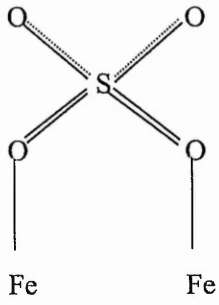

Bridged Bidentate Complex
(C_{2v})

The C_{2v} symmetry is the lowest possible symmetry group possible by sulfate (SO_4^{2-}) and can be either chelating or bridging, as shown above.

Figure 6: Infrared spectra of goethite, and goethite derived samples

Goethite

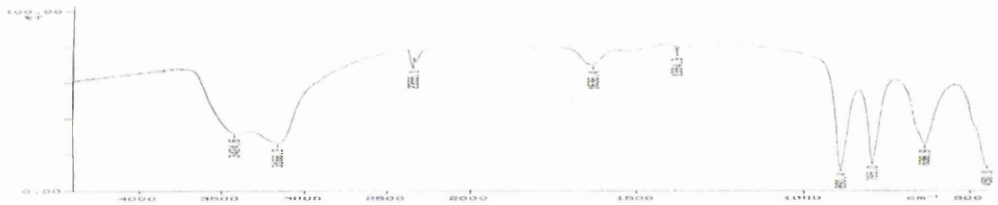

H_2O/Goethite

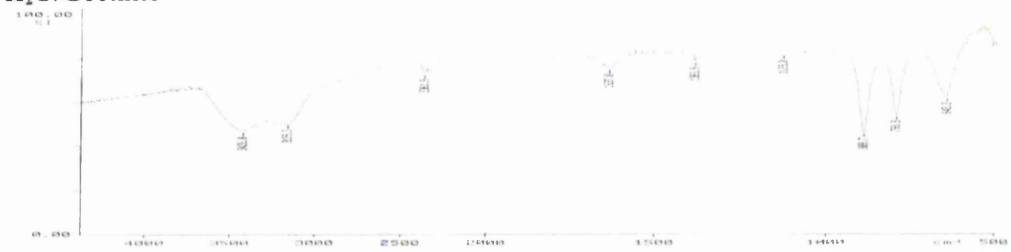

SO_4^{2-}/Goethite

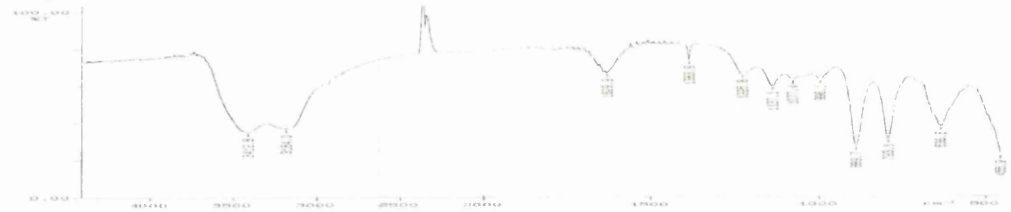

H_2O/Fe_2O_3

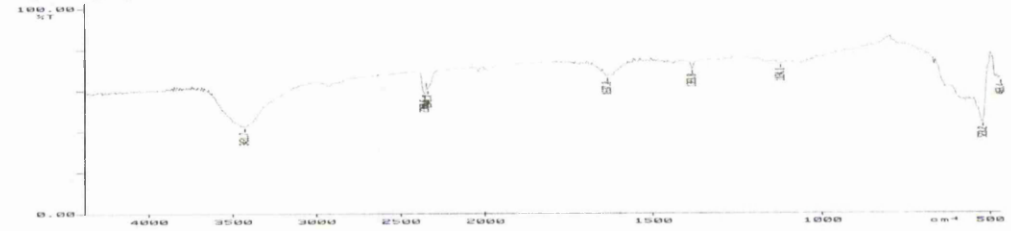

SO_4^{2-}/Fe_2O_3

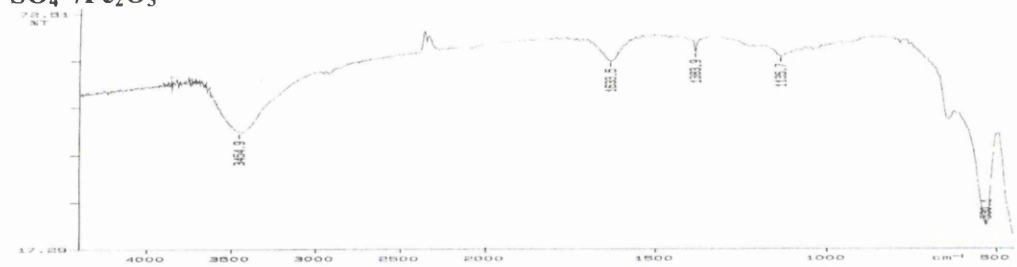

Figure 7: Infrared spectra of 2-line ferrihydrite and derived samples

2-Line ferrihydrite

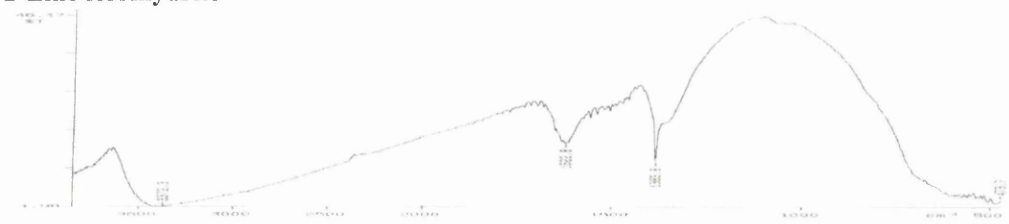

H_2O/2-Line ferrihydrite

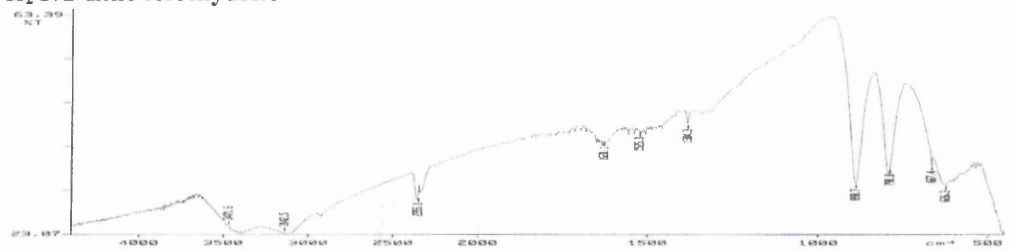

SO_4^{2-}/2-Line ferrihydrite

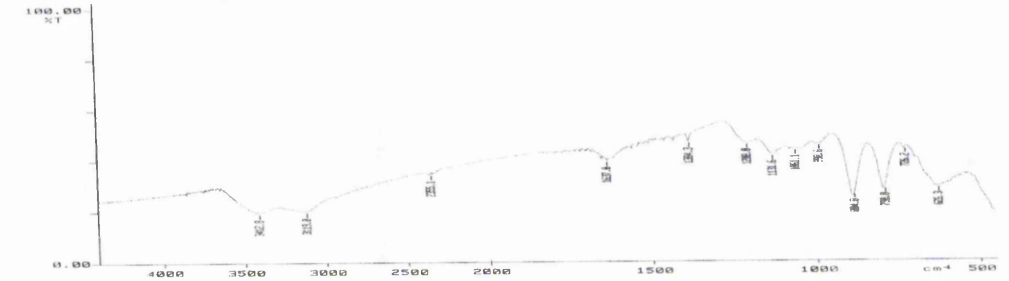

H_2O/Fe_2O_3

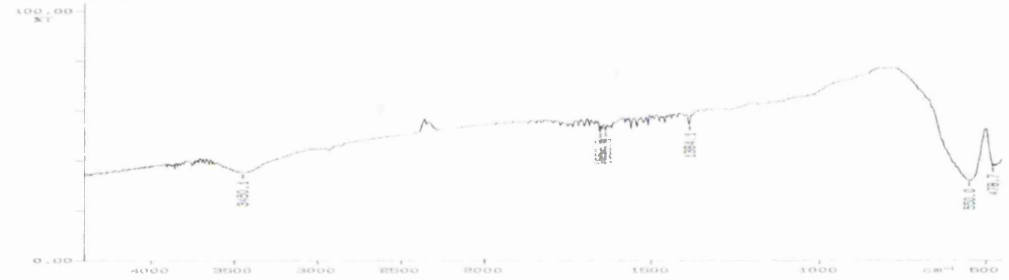

SO_4^{2-}/Fe_2O_3

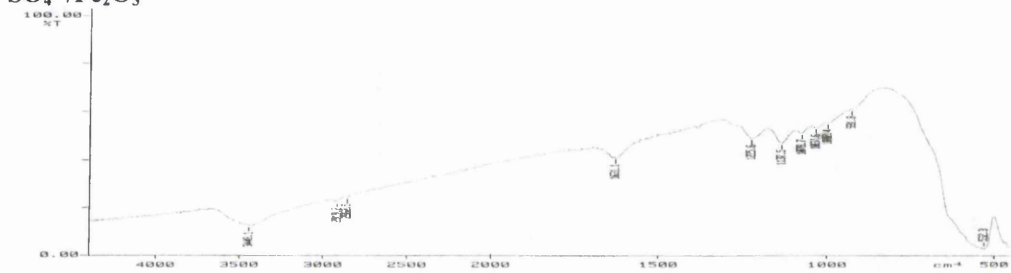

However distinguishing between the two complexes is difficult. Nakamoto et al in studying sulfate complexes based on cobalt and lead by infrared spectroscopy concluded that the sulfate groups could be distinguished on the basis of the highest υ_3 frequency which for bidentate sulfate lies above 1200 cm^{-1} and for the bridged complex lies below 1200 cm^{-1}[114]. Parfitt et al in their studies of sulfate adsorbed on goethite from sulfuric acid solutions, warned of the dangers in using infrared spectroscopy data alone to differentiate between the two complexes[115]. The authors suggested that in order to determine the type of complex formed further structural evidence must be obtained.

Table 7: A summary of FT-IR data for goethite, 2-line ferrihydrite sulfated and non-sulfated haematites.

Material	(O-H) st/cm^{-1}	H_2O bend cm^{-1}	SO_4^{2-} st/cm^{-1}	Fe-O st/cm^{-1}
Goethite	3425, 3166	-	-	890,795 639,450
SO_4^{2-}/Goethite	3413, 3184	-	1226,1137 1077, 996	890,793 637,456
H_2O/Goethite	3426, 3159	-	-	890,794 642
2-Line Ferrihydrite	3372	-	-	474
SO_4^{2-}/2-Line Ferrihydrite	3413, 3131	-	1208, 1132 1061, 991	885,791 726,626
H_2O/2-Line Ferrihydrite	3472, 3143	-	-	891, 791 668, 626
H_2O/Fe_2O_3 (G)	3432	1637	-	525,469
SO_4^{2-}/Fe_2O_3 (G)	3455	1634	-	530
H_2O/Fe_2O_3 (F)	3450	1636	-	550, 479
SO_4^{2-}/Fe_2O_3 (F)	3448	1631	1226, 1138, 1079, 1038, 1002, 932	523

G=goethite, F=2-line ferrihydrite and st=stretch

Therefore in this study the type of complex is not assigned. However, Parfitt et al in their studies, indicated above, postulate the formation of a bridging complex Fe-O-SO_2-O-Fe, which was similar to the type of complex found in phosphate absorption the goethite precursor, which on addition of both sulfate and water appeared

the goethite precursor, which on addition of both sulfate and water appeared unchanged. The first two bands are sensitive to any cation substitution. Similar bands for 2-line ferrihydrite were also observed, Table 7. On calcination sulfate is retained after calcination of the sulfated 2-line ferrihydrite sample, with six bands in the sulfate region 1200-900 cm^{-1}, being observed Figure 7, although several of these bands are very weak. The presence of so many bands makes the analysis complex, but it may indicate that a mixture of sulfate symmetries, including the C_{2v} sulfate complex, is present. It is evident that an amount of sulfate has been lost during calcination of the sulfated goethite sample, as no apparent sulfate bands were observed in this region. The differing degree of sulfate decomposition may relate to the differences in sulfate uptake initially, and may ultimately explain the marked effect of sulfation on the specific activity on the 2-line ferrihydrite derived sulfated iron oxide. Hence it may be suggested that sulfate adsorbs onto the precursors, the amount of which may be precursor dependent or dependent upon the amount of adsorbed water during storage. On calcination it is apparent that an amount of sulfate is lost probably in the form of SO_2, which appears to be precursor dependent since all the samples were calcined at the same temperature. For goethite derived sulfated iron oxide particularly sulfate appears to be completely removed by heat treatment. However the effect of sulfate is still observed in the Mossbauer studies, discussed in the previous section. This indicates that an amount of sulfate is still present in this sample. The co-ordination of the resulting adsorbed sulfate appears unchanged after calcination with the possible inclusion of other sulfate complexes X-ray diffraction experiments indicated an anomalous x-ray line broadening, particularly in the goethite derived sulfated iron oxide sample which, was related to the topatactic transformation. Further, it is known that the thermal transformation of iron precursors to haematite may be hindered by the adsorption of silicate, phosphate and sulfate as well as by a range of organic compounds. Therefore, it may be proposed that the adsorption of sulfate, in a C_{2v} symmetry, may retard the movement of iron centres during calcination pinning the iron centres preventing them from further movement to their new equilibrium positions.

3.2.5: Transmission Electron Microscopy

Figure 8-10, shows micrographs of the precursors 2-line ferrihydrite, lepidocrocite and goethite and of their corresponding sulfated and non-sulfated iron oxide samples, respectively. 2-line ferrihydrite is observed to comprise of heavily aggregated areas of fine particles and is similar to the precursor prepared by the Arata method. The amorphous nature of the precursor was confirmed by x-ray diffraction which, showed two very broad reflections indicative of fine crystallites <10nm. The lepidocrocite precursor, Figure 9, although showing a poorly defined morphology in the transmission electron micrograph, produces a powder x-ray diffraction pattern, indicating that this material has a degree of crystallinity. Transmission electron microscopy experiments by Giovanoli et al[106], on the thermal transformation of γ-FeOOH to α-Fe_2O_3 found corrugated regions which showed unusual extinction contours called Bragg fringes, at a magnification of 5000K, on partly decomposed crystals. Bragg fringes are bands in which the Bragg condition for diffraction are fulfilled and therefore produces an electron diffraction pattern. The magnification used in this study was not sufficient to observe the corrugated structure observed by Giovanoli. It is known that the morphology of haematite may be related to its precursor at calcination temperatures below 600C[89]. Non-sulfated iron oxide derived from 2-line ferrihydrite, Figure 8, appears to consist of heavily aggregated areas of irregular shaped crystals. Sulfation of this precursor, Figure 8, is observed to produce a decrease in the particle size, and these particles also appear to be more uniform. A similar variation in particle size is also observed between the sulfated and non-sulfated iron oxide derived from lepidocrocite. These variations in particle size may explain the general increase in the specific surface area with sulfation and are consistent with powder x-ray diffraction line widths.

Transmission electron microscopy studies on goethite shows needle like acicular crystals characteristic of those published in the literature[89]. Non-Sulfated and sulfated samples, Figure 10, calcined at 550C showed a related morphology to that of the precursor, with the sulfated sample showing some elongation from 0.5μm to ~1μm along the c-axis, the growth axis. The aspect ratios i.e length:width ratio, of the sulfated and non-sulfated haematites are similar, therefore, as mentioned

Figure 8: Transmission electron micrographs of 2-line ferrihydrite and derived sulfated and non-sulfated iron oxide samples

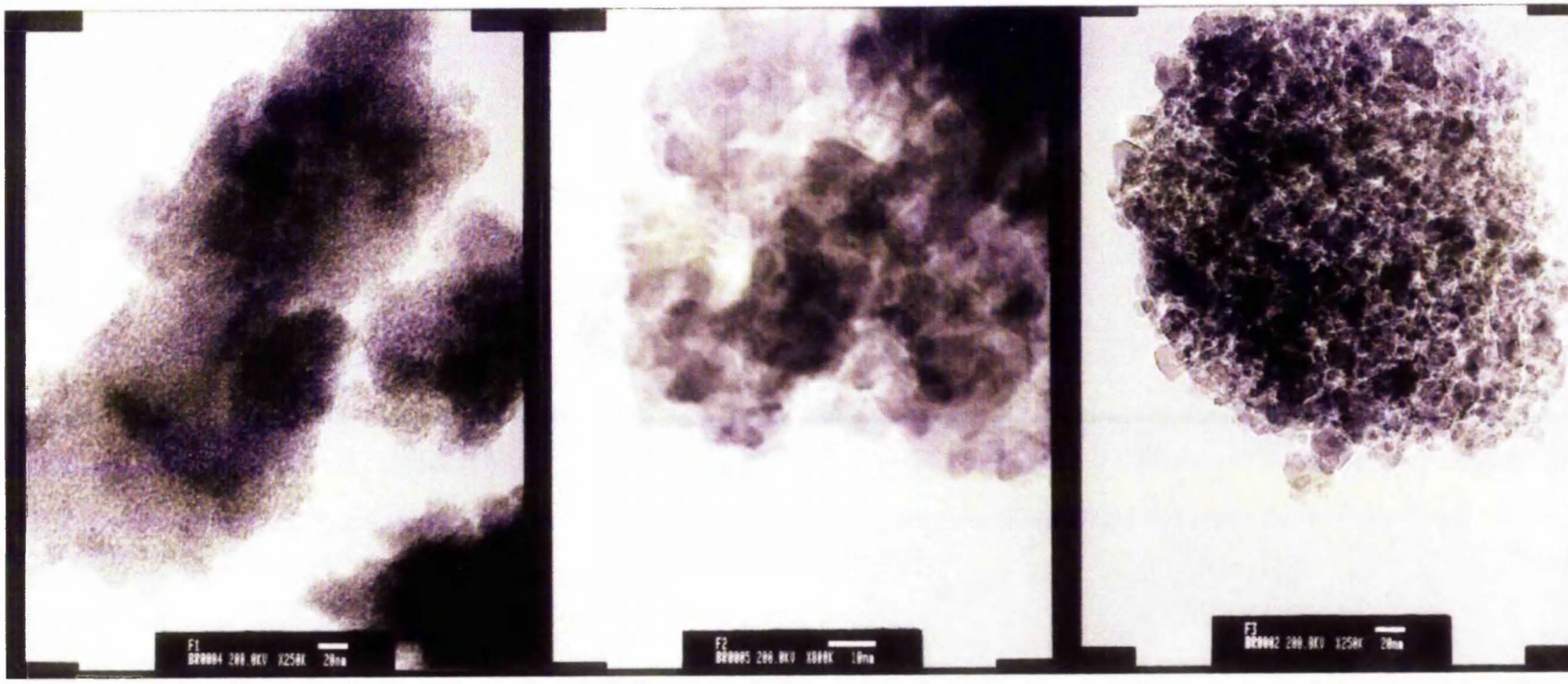

(F1) 2-line ferrihydrote, (F2) Non-Sulfated iron oxide derived from 2-line ferrihydrite and (F3) sulfated iron oxide derived from 2-line ferrihydrite

Figure 9: Transmission electron micrographs of lepidocrocite and derived non-sulfated and sulfated iron oxide samples

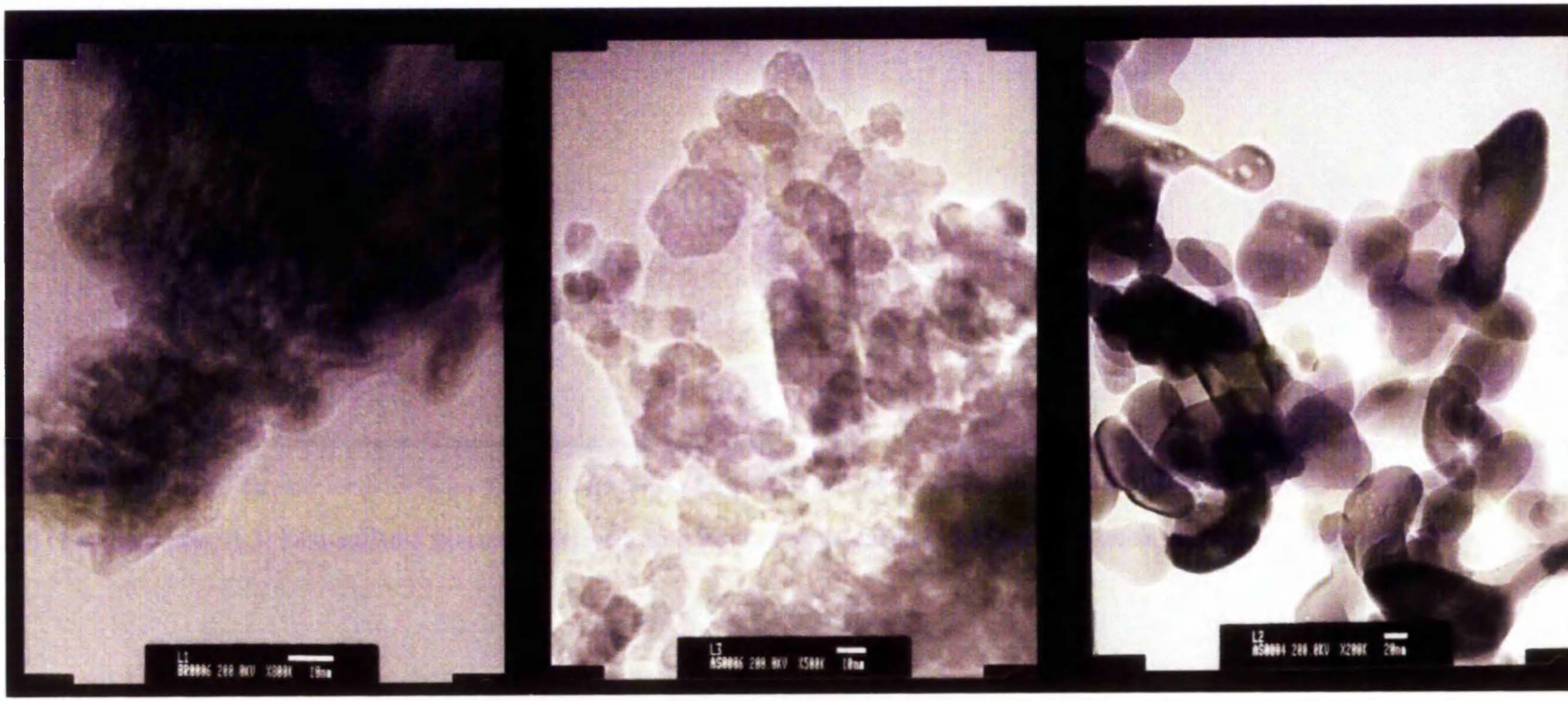

(L1) Lepidocrocite, (L3) Non-sulfated iron oxide derived from lepidocrocite and (L2) Sulfated iron oxide derived from lepidocrocite

Figure 10: Transmission electron micrographs of sulfated iron oxide, goethite and non-sulfated iron oxide samples

(G1) Sulfated iron oxide derived from goethite, (G2) Goethite and (G3) Non-sulfated iron oxide derived from goethite

Previously, anisotropic x-ray line broadening observed in the x-ray diffraction profiles for the sulfated sample can be discounted.

However, the sulfated haematite sample also appeared porous with the surface of the material appearing pitted. Similar observations for the non-sulfated material were also observed, although the extent of pitting was significantly lower. Such observations of the porous nature of haematites were confined only to haematites produced from goethite. Therefore it was assumed that porosity observed in the sulfated samples is as a result of proton attack at the domain boundaries of the goethite precursor, although subsequent measurements performed at the University of Liverpool has shown that this mechanism is not operative. In the case of the sulfated material increased porosity was due to the direct addition of the sulfuric acid solution compared to the distilled water added to the non-sulfated sample. The effect of porosity as a cause of anisotropic x-ray line broadening was proposed by Naono et al[111] and was previously discussed. In an attempt to investigate this anomaly further, similarly prepared sulfated and non-sulfated haematites derived from goethite were prepared[113]. Calcination of these materials was at 350C where anisotropy becomes more prominent, Table 8.

Table 8: FWHM values for sulfated and non-sulfated haematite derived from goethite calcined at 350C[113]

Reflection	Full Width Half Maximum/ degrees 2θ	
	H_2O/Fe_2O_3	SO_4^{2-}/Fe_2O_3
(012)	1.20	2.50
(104)	0.65	1.90
(110)	0.40	0.50
(113)	0.70	0.50
(024)	0.65	1.50
(116)	0.60	1.00
(018)	1.20	-
(214)	0.70	1.00
(300)	0.40	0.70
(1010/119)	0.90	-

Investigations of this material were performed using high resolution transmission electron microscopy (HRTEM) at the University of Liverpool by Prof. C. Kiely. Figure 11 shows the transmission electron micrograph of the sulfated haematite sample calcined at 350C. TEM confirms that the needle dimensions of the sulfate and non-sulfated sample are comparable, in agreement with transmission electron microscopy observations for the samples calcined at 550C. As can be seen by comparing the micrographs in Figure 10, the sulfated sample is associated with pore formation, and these pores are regularly shaped and run down the centre of the needles (Appendix 2 shows the TEM of the goethite precursor for the samples calcined at 350C). Internal voids which run along the lengths of the needles, which are of variable length and are sometimes open ended, are a feature of the sulfated material calcined at 350C. Elemental mapping of this material showed that the pores were associated with sulfur, Figure 12. Stacking faults previously reported by Lima de-Faria, as a possible cause of anisotropic x-ray line broadening were not observed in either of the samples[110]. Although the overall crystallite dimensions were observed to be similar for both the sulfated and non-sulfated iron oxides derived from goethite in this study, the development of internal voids effectively reduces the Scherrer size across the crystal, whilst that along the crystal remains unchanged. This would have the effect of producing anisotropic broadening in those reflections, which relate more to the needle width. As a consequence of this investigation, it is proposed that sulfation modifies the effective crystal thickness via the modification of porosity resulting in anisotropy. A relationship given by Derie et al for determining crystal thickness for the (104), (116) and the (024) planes, where the high l index of these planes gives an indication of crystal thickness, is given below[108].

(104) $\longrightarrow$ 1.27t

(116) $\longrightarrow$ 1.35t

(024) $\longrightarrow$ 1.89t

Where t = crystallite thickness.

Figure 11: HREM of sulfated iron oxide derived from goethite calcined at 350C

Sulfated iron oxide

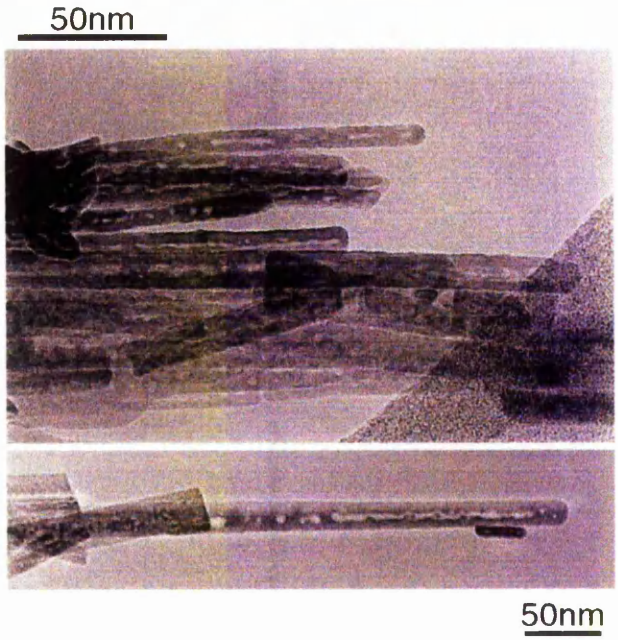

Therefore it is possible to calculate the crystallite thickness from the Scherrer equation for the 350C and 550C sulfated and non-sulfated samples assuming no broadening due to strain and/or instrumental effects, Table 8.

It is apparent from the calculations that the average crystallite size of the sulfated samples is approximately twice that of their non-sulfated counterparts at the same temperature of calcination, Table 8. This can be explained as an effect of the porosity caused by sulfation limiting the diffraction from these planes. This results in a two fold increase in crystallite thickness. Determining the difference in crystallite thickness between the sulfated and non-sulfated sample, at the specified temperature, also has the effect of removing any instrumental x-ray broadening, which is a possible source of x-ray line broadening. It can be seen that the difference in crystallite thickness of the sample calcined at 350C is ~60Å which is similar to the difference in crystallite thickness between the sulfated and non-sulfated sample at 350C measured by TEM ~80Å. The samples calcined at 550C show a sample thickness approximately twice that measured for the 350C sample ~130Å. However it must be stated that these samples were from two different batches of goethite. However this may still indicate that the crystals increase in thickness with calcination temperature.

Table 8: shows crystallite size and crystallite thickness for sulfated and non-sulfated haematite samples calcined at 350 and 550C

	Crystallite Size/Å				t/Å				Difference in t/Å	
T	**350C**		**550C**		**350C**		**550C**		**350C**	**550C**
Planes	H_2O	SO_4^{2-}	H_2O	SO_4^{2-}	H_2O	SO_4^{2-}	H_2O	SO_4^{2-}	H_2O	SO_4^{2-}
(104)	141	49	305	131	111	39	240	103	72	137
(116)	166	96	329	164	123	71	244	122	52	122
(024)	149	64	386	138	79	34	204	73	45	131
Average/ Å	**152**	**70**	**340**	**144**	**104**	**48**	**229**	**99**	**56**	**130**

H_2O indicates non-sulfated haematite, SO_4^{2-} indicates sulfated haematites. T is the calcination temperature in degrees Celsius, and t is the crystallite thickness in Å.

Therefore it can be concluded that the formation of pores in sulfated haematite derived from acicular synthetic goethite, modifies the thickness of the crystals and limits the x-ray diffraction from the (012), (104), (110), (024), (116), (214) and (300) planes. These planes not only give an indication of the needle thickness but also relates to the cation positions on thermal transformation of the goethite via the topatactic mechanism. It may also be postulated that the amount of sulfate in the final haematite, which is a function of calcination temperature, may retard the cation movement on sulfation. Calcination of the goethite material at high temperatures leads to a complete change in the morphology. Figure 12, shows the goethite material calcined at 750C, the change in morphology is due to the fusion of the needle shaped crystals.

The average crystallite sizes for the sulfated and non-sulfated samples, in Table 8, indicates that sulfation reduces the crystallite size. This reduction in crystallite size as previously discussed was implied to be responsible for the twofold increase in surface area. However, as discussed above transmission electron microscopy and high resolution electron microscopy indicated that the morphology of both systems were similar. Therefore a reduction in crystallite size cannot explain the two fold increase in surface area.

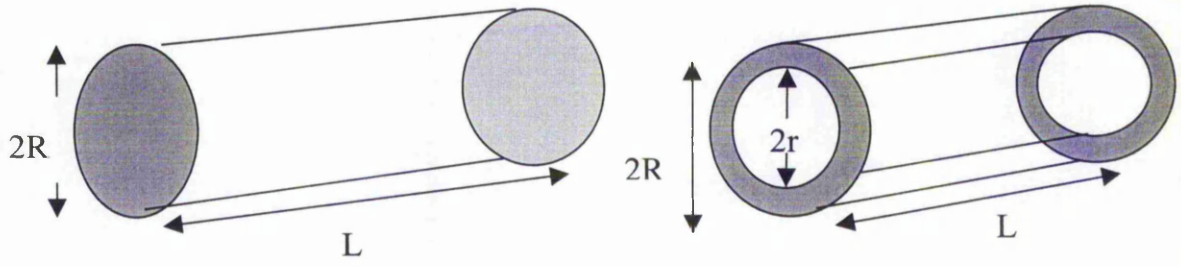

Model A Model B

Cylindrical model of (A) non-sulfated haematite crystal and (B) Sulfated haematite crystal

R = 7.5nm, L=1μm and ρ= 5.26 g cm^{-3} and r = 2nm.

Figure 12: **HREM of sulfated and non-sulfated iron oxide derived from goethite calcined at 750C**

Sulfated iron oxide

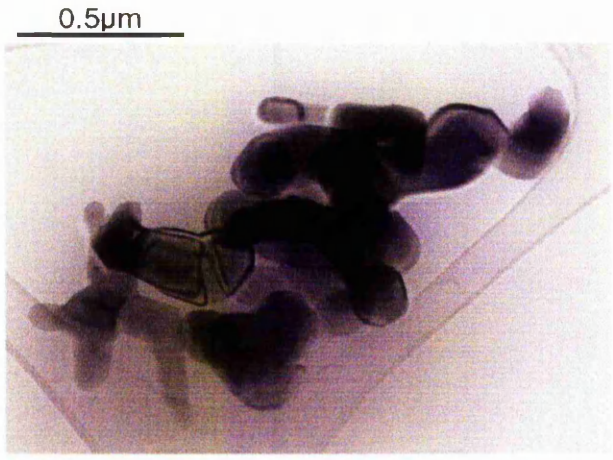

Non-sulfated iron oxide

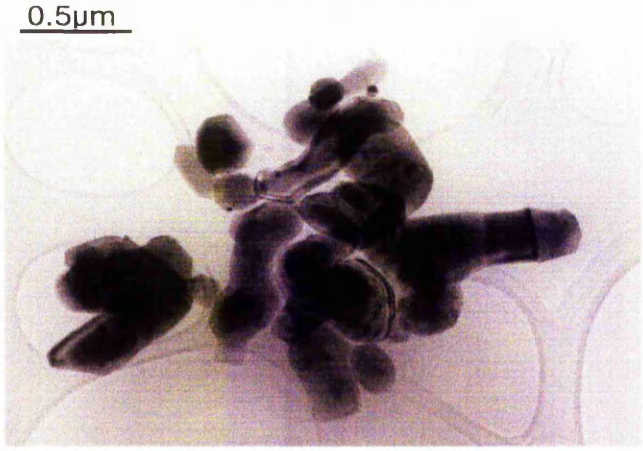

In an attempt to explain the difference in surface area between the sulfated and non-sulfated sample a model given above was proposed. Measurements of the dimensions of the crystal were taken from high resolution transmission electron microscopy.

Calculation of Specific Surface Area for the Non-Sulfated Haematite Model A.

Mass Of Crystal = $\pi R^2 \rho L$ Area of crystal = $2\pi RL$

Specific surface area = Area / Mass = 51 m^2/g.

Specific surface area measured by N_2 absorption BET method = 38 m^2/g.

Calculation of Specific Surface Area for the Sulfated Haematite Model B.

Mass of crystal = $\pi R^2 L\rho - \pi r^2 L\rho$ Area of crystal = $(2\pi RL + 2\pi rL) - 2\pi r^2$

Specific surface area = Area / Mass = 70 m^2/g.

Specific surface area measured by N_2 physisorption BET method = 68 m^2/g.

Although this model over estimates the specific surface area, it is useful in explaining the twofold increase in specific surface area. The increase in specific surface area is due to the loss of material through the dissolution of the goethite forming a porous structure, which increases the surface area of the resulting sulfated haematite sample. Therefore the increase in surface area is due to a reduction in sample mass and the increase in surface area as a result of the development and/or stabilisation of porosity.

3.2.6: Post Reactor Analysis

powder x-ray diffraction analysis

X-ray diffraction patterns of the post reactor non-sulfated iron oxides shown in Figure 13 shows the crystallinity of the materials to be reduced and the phase of the materials to be haematite α-Fe_2O_3. However post reactor goethite derived non-sulfated iron oxide shows a mixed phase of haematite and maghemite γ-Fe_2O_3 (JCPDS 25-1402). Maghemite formation directly from haematite is not known to occur[89]. However it is known that haematite transformation to maghemite operates via a reduced iron oxide phase magnetite, Fe_3O_4. It is evident that under the

reducing conditions created in the reactor, i.e. high oxygen conversion, that the haematite phase can be reduced to magnetite.

Figure 13: Powder x-ray diffraction patterns of post reactor non-sulfated iron oxides

Post reactor non-sulfated iron oxide derived from goethite

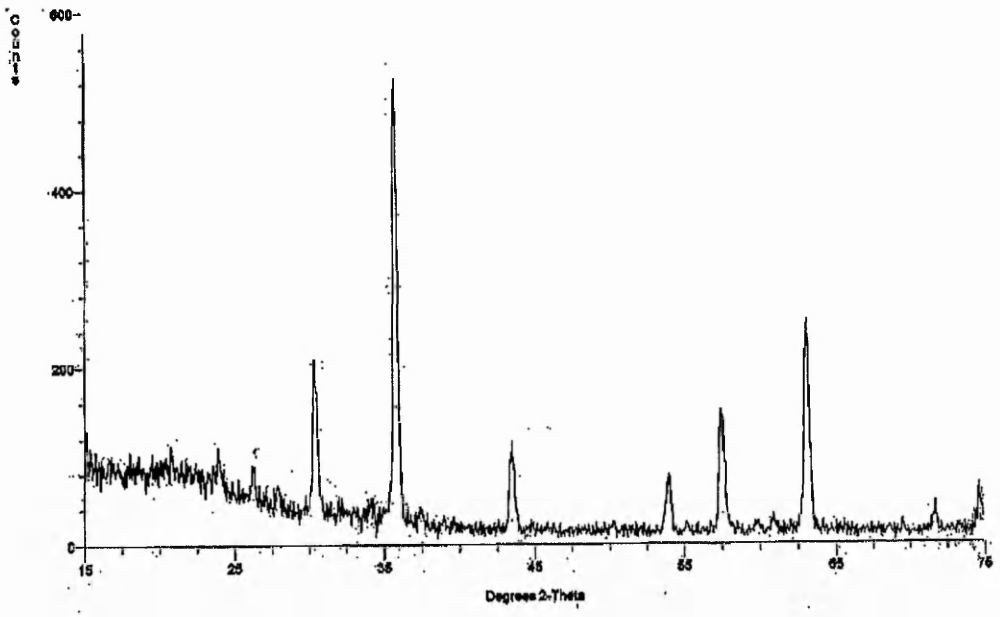

Post reactor non-sulfated iron oxide derived from 2-line ferrihydrite

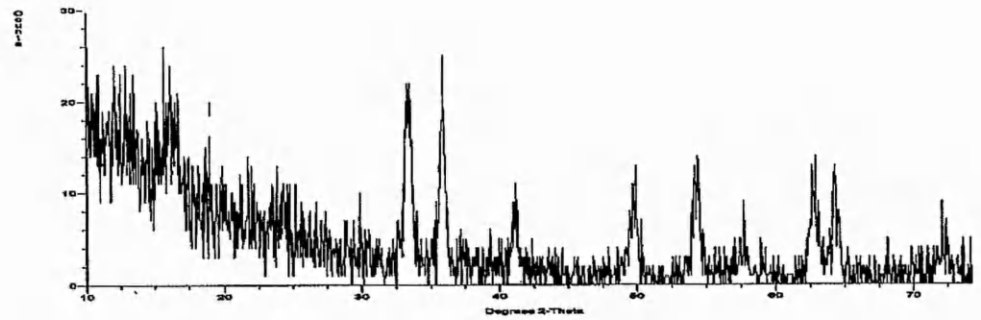

Figure 14: Post reactor powder x-ray diffraction patterns of sulfated iron oxide samples

Post reactor sulfated iron oxide derived from 2-line ferrihydrite

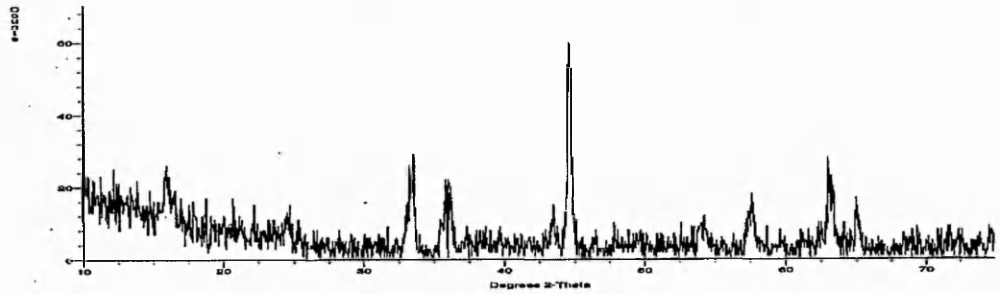

Post reactor sulfated iron oxide derived from feroxyhyte

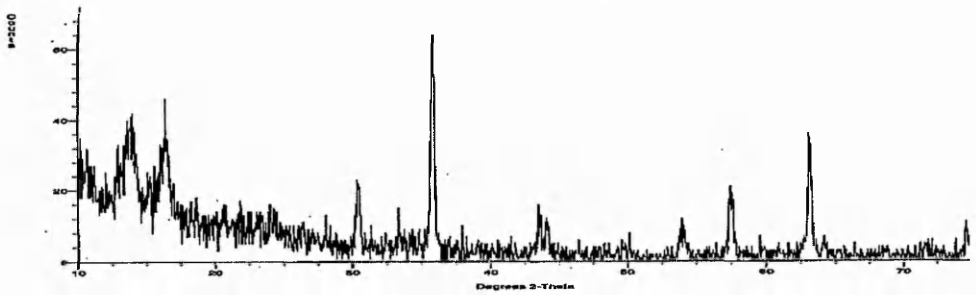

Post reactor sulfated iron oxide derived from goethite

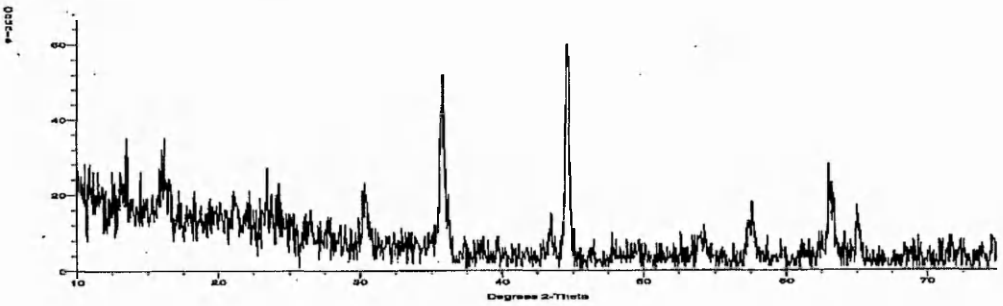

Post reactor sulfated iron oxide derived from the Arata method

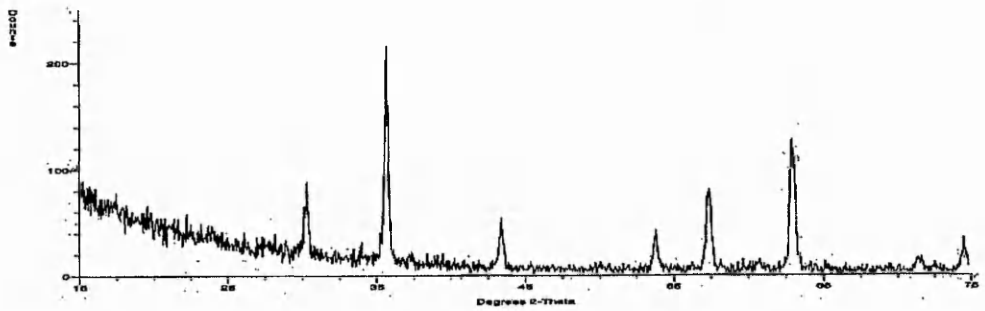

Maghemite phase formation observed from the x-ray diffraction profile occurs as a result of the re-exposure of the sample to the reaction atmosphere at 450C, (a standard procedure in these experiments), thereby reoxidising the magnetite phase to maghemite. The overall scheme is given below.

α-Fe_2O_3 $\xrightarrow{\text{(Reduction)}}$ Fe_3O_4 $\xrightarrow{\text{(Oxidation)}}$ γ-Fe_2O_3

X-ray diffraction of the post reactor sulfated iron oxide samples, Figure 14, also show a decrease in crystallinity and a high background, which indicates a large degree of amorphous content. Phase identification of the samples also showed a mixed phase is produced for both the Arata and goethite materials. However post reactor sulfated iron oxide derived from 2-line ferrihydrite showed the phase to be haematite. The observations are consistent with the interpretation of the reactor data previously discussed. The haematite phase is associated with the production of carbon dioxide. As the oxygen conversion increases during the reaction, suitable conditions for the partial reduction of the haematite iron oxide phase, which then becomes active for the water gas shift reaction at higher temperatures.

Table 9: Post reactor data for goethite, 2-line ferrihydrite and Arata non-sulfated iron oxides.

Goethite			2-Line Ferrihydrite		
Crystallite size/Å	Width (2θ)	Phase	Crystallite Size/ Å	Width (2θ)	Phase
607	0.15	M,Mg	153	0.60	H
462	0.2	H,M	231	0.40	M
270	0.35	M	162	0.60	H
395	0.25	M	198	0.50	H
295	0.35	M	172	0.60	Mg
542	0.20	M			
286	0.35	M			
408			**308**		

M= Maghemite, Mg= Magnetite and H=haematite

This is evidenced in the reactor data for non-sulfated iron oxide derived from goethite. Sulfated materials appear to be more susceptible to a degree of phase reduction, which is probably due to the reaction environment, under high oxygen conversion.

Table 10: Post reactor data for goethite, 2-line ferrihydrite and the Arata derived sulfated iron oxides

Goethite			2-Line Ferrihydrite			Arata		
Crystallite size/Å	Width (2θ)	Phase	Crystallite Size/ Å	Width (2θ)	Phase	Crystallite Size/ Å	Width (2θ)	Phase
182	0.50	M	153	0.60	H	303	0.30	M
308	0.30	M	154	0.60	Mg	462	0.20	H
380	0.25	-	372	0.25	M	378	0.25	M
100	0.60	M	475	0.20	M	395	0.25	M
258	0.40	M	123	0.80	H	286	0.25	Mg
345	0.30	-	695	0.15	H	170	0.60	M
						344	0.30	M
						181	0.6	Mg/M
262			**329**			**315**		

M= Maghemite, Mg= Magnetite and H=haematite

3.3: Conclusions

Catalytic activity of the non-sulfated iron oxides is dependent upon the nature of the precursor. The effect of sulfation suppresses low temperature oxidation while enhancing the oxidation activity at higher reaction temperatures. Further selective oxidations products are also formed under high oxygen conversions over the sulfated iron oxide materials. The structure of the adsorbed sulfate appears to be a C_{2v} symmetry, which may affect the thermal transformation to haematite. Specific effects were observed for iron oxides derived from goethite, with anomalous x-ray line broadening effects. Mossbauer spectroscopy studies of this material indicate that this may be associated with cation disordering. However TEM results indicate that the incorporation of sulfate modifies mesoporosity. This therefore may indicate a method for preparing haematite nanotubes from goethite.

4.0: THE USE OF MOLYBDATED ZIRCONIUM OXIDES FOR THE PARTIAL OXIDATION OF METHANE

4.1: General Introduction

It is evident from an investigation of the literature that molybdenum containing materials have been and continue to be applied to the direct partial oxidation of methane[117,118]. In this respect the direct conversion of methane to formaldehyde or methanol, its precursor, continues to be of interest. As discussed in the introduction to Chapter 3, Dowden and Walker reported space-time yields for methanol and formaldehyde over a low surface area ($0.1m^2/g$), catalyst containing 5wt% $(MoO_3)\cdot Fe_2O_3$ supported on alumina/silica (25%:75%)[97]. Their most active catalyst produced both methanol and formaldehyde with space-time yields of 869 and 100 g(Kg cat)$^{-1}$ h^{-1} respectively. The replacement of the iron oxide component with copper oxide leads to an analogous $CuO\cdot MoO_3$ system, which was studied by Stroud in 1975[119]. Under similar experimental conditions as those employed by Dowden et al the author observed oxygenated products including methanol. For example, at a reaction temperature of 485C and a pressure of 20atm with a gas hourly space velocity (GHSV) of 46,700 h^{-1}, a combined space time yield of 490 g(Kg cat)$^{-1}$ h^{-1} for oxygenates was achieved. This value included ethanol, acetaldehyde and formaldehyde as well as methanol. The formation of C-2 oxygenates as well as ethene was due to the addition of ethane (6% on average), which was suggested to be beneficial for the formation of oxygenates.

In 1982 Liu et al published their first paper using nitrous oxide as oxidant instead of molecular oxygen for the catalytic oxidation of methane over MoO_3/SiO_2[120]. Nitrous oxide is considered to be a weaker gas-phase oxidant and to deliver atomic oxygen species. The authors observed high combined selectivity towards both methanol and formaldehyde at 84.6% with a methane conversion of 16% at reaction temperature of 560C and a pressure of 1 bar for 1.7wt% MoO_3/SiO_2 catalyst. They also found that the addition of steam increased the selectivity towards methanol by inhibiting further oxidation. In further studies by the same authors it was found that by supporting molybdenum oxide on Cab-O-Sil M-5 silica, the catalyst produced formaldehyde, methanol and carbon monoxide with little or no carbon dioxide[121]. A combined selectivity of 78.1% towards methanol and formaldehyde was observed over the

1.7wt% MoO_3/SiO_2 catalyst. Liu et al were the first to consider a mechanism for the activation of methane and their conversion to oxygenates and the kinetics for the partial oxidation of methane[121]. Based on catalytic results using nitrous oxide in the presence of steam the following rate expression was suggested.

$$\frac{d[CH_4]}{dt} \quad -k[N_2O]^1[CH_4]^1$$

The Arrhenius plot of the rate of methane conversion was linear over the temperature range 550-594C, giving an activation energy of 176 ± 8 kJ/mol. They proposed a mechanism not only for the selective oxidation of methane but also for the non-selective oxidation. Using electron spin resonance spectroscopy they showed that the O^- species from N_2O was responsible for the initiation of the selective oxidation cycle. ESR also showed the existence of $CH_3^{\cdot}$ radicals that reacted with surface $Mo(V)O^{2-}$ moieties to form surface methoxy anions CH_3^-. Liu et al proposed the following reaction mechanism for the partial oxidation of methane[121].

$$Mo(V) + N_2O \longrightarrow Mo(VI)O\text{-} + N_2$$
$$Mo(VI)O^- + CH_4 \longrightarrow Mo(VI)OH^- + CH_3^{\cdot}$$
$$Mo(VI)O^{2-} + CH_3^{\cdot} \longrightarrow Mo(V)OCH_3^-$$
$$Mo(V)OCH_3^- + H2O \longrightarrow Mo(V)OH\text{-} + CH_3OH$$
$$Mo(VI)OH^- + Mo(V)OH^- \longrightarrow Mo(V) + Mo(VI)O^{2-} + H_2O$$

Khan and Somorjai described a series of similar experiments[122]. They were successful in reproducing Liu et al's results, but their examination of the kinetics showed some important differences. They were able to specify rate equations for the formation of methanol and formaldehyde. For methanol formation the rate was found to be approximately first order with respect to methane and water and zero order with respect to nitrous oxide. In the case of formaldehyde the kinetic orders were zero with respect to all reactants. The rate of formation of methanol and formaldehyde was measured over the temperature range of 480-590C. The Arrhenius plot for methanol formation showed a linear relationship up to 520C indicating an approximate activation energy of 172 ± 17kJ/mol and 168 ± 8kJ/mol below 540C. Methanol and formaldehyde were formed simultaneously from the same intermediate by two independent pathways. Above 540C the activation energies for methanol and formaldehyde can be seen to be

almost identical, implying the formation of formaldehyde by the sequential oxidation of methanol. Khan and Somorjai were still unable to supply an explanation of the role of steam in the reaction[122]. One suggestion they did put forward was that the steam prevented the formation of carbonaceous deposits on the catalyst surface, as experiments into the reaction without steam were unsuccessful due to coking of the catalyst.

Since Liu et al demonstrated the ability of molybdenum oxide supported silica catalysts to produce methanol and/or formaldehyde from the partial oxidation of methane, there have been numerous investigations on this material[81,83,190-193]. The role of sodium present at ppm levels in the silica support was reported by Spencer et al to retard the direct oxidation of methane to formaldehyde and carbon dioxide whilst promoting further oxidation of formaldehyde to carbon monoxide[123]. The inhibitory effect of sodium was also confirmed by Kennedy et al using a 7wt% MoO_3/Cab-O-Sil catalyst, at low methane conversions (<0.13%), using oxygen as the oxidant. The influence of the support was investigated by Hodnett et al[124,125]. The authors used MgO and TiO_2 to support the molybdenum oxide phase and compared their results to molybdenum supported on porous silica (Spherosil) and Cab-O-Sil (fumed silica). At a temperature range of 500-600C using nitrous oxide both the MgO and TiO_2 materials produced only carbon oxides while the silica materials produced formaldehyde. A zeolite containing molybdenum oxide catalyst has been tested by Banares et al[126]. A range of ultrastable (USHY) zeolites were synthesised using different molybdenum precursors and methods of activation. However, the main products observed over these catalysts were carbon oxides. These materials exhibited some formaldehyde selectivity, approximately 6% at low conversion with oxygen as oxidant. There most selective catalyst was an 8wt% MoO_3-USHY with 9% selectivity towards formaldehyde at 550C. Wada and co-workers reported on the use of zinc oxide as a support material for molybdenum[127]. The authors used ultra-violet radiation at >300nm wavelengths to enhance the selectivity towards formaldehyde from methane at low temperatures 227-277C.

The influence of oxidant and molybdenum loading were investigated by Banares et al[128]. A series of molybdenum materials were prepared in the range 0.5-16.2wt%. The authors observed that using molecular oxygen increased the selectivity towards formaldehyde while decreasing carbon oxides selectivity relative to nitrous oxide examined under the same test conditions.

A number of studies have attempted to define the surface features of the MoO_3/SiO_2 catalyst. Bardaux et al observed three different regions of distribution and molybdenum species, which were dependent upon the molybdenum content[129]. Molybdenum loadings in the range 1-5wt%, showed a uniformly distributed phase, interacting strongly with the support, which was identified as silicomolybdic acid (SMA). From 5-10wt% loadings, a polymolybdate species was also observed which appeared to cover the SMA phase but not the support. At molybdenum loadings of 15wt%, SMA was no longer observed and crystalline bulk MoO_3 species were identified, distributed over the polymolybdate phase. Micro-reactor studies, at 597C with nitrous oxide over the 1-5wt% molybdenum catalyst, correlated formaldehyde selectivity with the concentration of the SMA phase. Hu et al using in-situ X-ray adsorption near edge spectroscopy (XANES) measurements at elevated temperatures and in the presence of oxygen, revealed that surface molybdenum oxide species on SiO_2 possess a co-ordination which was between tetrahedral and octahedral[130]. Corresponding in situ Raman and extended fine structure (EXAFS) spectroscopy measurements demonstrated that the surface molybdenum oxide species on SiO_2 was present as an isolated species[130]. In situ infrared spectroscopy studies by Conrac et al employing ^{18}O-labelling further showed the surface molybdenum oxide species on SiO_2 possess only one terminal Mo=O bond[131].

The use of supported molybdenum materials particularly MoO_3/SiO_2, are active for the partial oxidation of methane, as illustrated above. In this respect it would be of interest to apply, superacidic MoO_3/ZrO_2 catalysts, which until now have not been applied for this reaction. The significant difference between the catalyst used for partial oxidation and that described as a solid superacid, is in the method of preparation. Arata et al reported that the impregnation of hydrous zirconia provided a superacidic material, which is in contrast to the partial oxidation catalyst where the molybdenum precursor is generally impregnated on crystalline silica support. Therefore the aim of this study was to apply superacidic molybdated zirconia materials for the partial oxidation of methane and to characterise the nature of the molybdenum oxide phase(s).

4.2: Results and Discussion

4.2.1: Catalytic activity

The performance of molybdate doped zirconia materials for methane oxidation at elevated pressures and low space velocity, (ca. 4600h^{-1}), has been determined and the results are presented in Table 1. Their activity is in excess of the background, which was evaluated using α-Al_2O_3. It is apparent that carbon monoxide and carbon dioxide are the major products produced over the temperature range of 400-550C with only trace amounts ≤1% of the partial oxidation products methanol and ethane. The activity of the 5wt% MoO_3/ZrO_2 sample is generally greater than that of the other two samples investigated over much of the temperature range. No reaction products were observed at temperatures below 400C.

At the initial temperature of product formation, 400C, the ratio of carbon dioxide:carbon monoxide is 1:4 for both the 2 and 5wt% samples, however on increasing the molybdate content this ratio is increased to 1:1 for the 10wt % sample. This may indicate that the reaction pathways over the 2 and 5wt% samples are similar which led to similar activities and carbon dioxide:carbon monoxide ratio, as observed in Table 1. Similarly, the reaction routes leading to carbon dioxide and carbon monoxide production may be different over the 10wt% sample, leading to a higher ratio between the two products. However it is evident that methane conversion at 400C does not differ significantly between the samples i.e. 0.4± 0.1% methane conversion, while oxygen conversion increases linearly as a function of molybdate loading. This may indicate that molybdate as well as increasing surface area also promotes oxygen activation. On the basis of oxygen conversion for the 2wt% sample at 400C, the 5 and 10wt% samples showed higher oxygen conversions than expected on the basis of their surface areas. Therefore, the increase in oxygen conversion is not simply a surface area effect, but a function of molybdate loading. Above 400C the similarity in the activities between the 2 and 5wt% samples is no longer evident and the 2wt% sample displays catalytic activity more similar to that of the 10wt% sample, particularly at 500C and above. However, all the materials behave similarly at the highest reaction temperature of 550C. It is further noted that the activity of the 2wt% sample at 450C is intermediate between the activity of the 10wt% sample displayed at 400 and 450C, in terms of methane and oxygen conversions.

Table (1): Catalytic activity of molybdated zirconia samples for methane oxidation at elevated pressure.

Material	Surface Area $m^2 g^{-1}$	Temperature / C	Conversion[a] (%)		Selectivity[b] (%)				Carbon Balance[c] (%)	Oxygen Demand[d] (%)	Specific Activity[e] ($x10^4$ mol CH_4 conv. $g^{-1} min^{-1}$)
			CH_4	O_2	CO_2	CO	CH_3OH	C_2H_6			
2wt% MoO_3/ZrO_2	26	400	0.5	2.0	20	80	-	-	100	104	0.10
		450	0.9	7.6	46	54	-	-	100	105	0.17
		500	3.0	29.2	49	51	-	-	100	111	0.58
		550	8.1	84.8	65	34	trace	1	103	127	1.59
5wt% MoO_3/ZrO_2	33	400	0.6	3.9	21	79	-	-	98	104	0.11
		450	4.4	47.7	33	67	-	-	100	111	0.82
		500	7.5	57.4	62	38	-	-	105	149	1.39
		550	8.0	84.2	70	30	trace	1	99	142	1.48
10wt% MoO_3/ZrO_2	48	400	0.4	6.6	50	50	-	-	95	99	0.08
		450	1.7	20.3	53	47	-	-	95	105	0.33
		500	2.9	32.6	53	47	-	-	98	110	0.57
		550	7.1	73.7	59	40	-		103	130	1.40

[a-e]= See appendix 1 for definition.

All of the samples experienced a dramatic increase in oxygen and to a lesser extent methane conversions. This increase occurs at 500C for the 2wt% sample but at a lower temperature of 450C for the 5 and 10wt% samples. The 5wt% sample experiences the largest increase in methane and oxygen conversions than the other two samples, indeed the overall conversions of methane and oxygen is highest for this sample over the entire temperature range investigated.

Oxygen demands, shown in Table 1, were calculated based on the moles of oxygen consumed in reactions 1 and 2, calculated from the moles of carbon monoxide and carbon dioxide formed, as a percentage of the oxygen converted. Hence these values should be 100%, indicating that the formation of products is via reactions 1 and 2.

$$CH_{4(g)} + 1.5O_{2(g)} \longrightarrow CO_{(g)} + H_2O_{(g)} \qquad \text{Eqn 1}$$

$$CH_{4(g)} + 2O_{2(g)} \longrightarrow CO_{2(g)} + 2H_2O_{(g)} \qquad \text{Eqn 2}$$

It is observed from Table 1 that all the values for oxygen demand are greater than 100% with the exception the 10wt% sample at 400C. Therefore, in an attempt to determine the reaction pathways operating over the molybdated samples and thereby understand the differences and similarities in their activities, oxygen demands were calculated using alternative reaction pathways, given below are the possible reaction pathways operative.

$$CH_{4(g)} + 0.5O_{2(g)} \longrightarrow CO_{(g)} + 2H_{2(g)} \qquad \text{Eqn 3}$$

$$CH_{4(g)} + O_{2(g)} \longrightarrow CO_{2(g)} + 2H_{2(g)} \qquad \text{Eqn 4}$$

From the recalculated oxygen demands it is evident that there are several similarities between the samples. The 2 and 10wt% samples appear to operate via routes 2 and 3 over the temperature range 400-550C. This is shown by the small variation in oxygen demand values over this temperature range 100± 2%. However routes 1,4 cannot be discounted for the 10wt% sample over the temperature range nor can this route be discounted for the 2wt% sample at 400-450C.

Table 2: Summary of oxygen demands combinations for 2wt% MoO_3.

Temperature/C	Combinations of Reaction Equations			
	1,2	1,4	2,3	3,4
400	102	104	102	101
450	106	102	102	98
500	112	100	100	88
550	127	87	106	66

Table 3: Summary of oxygen demands combinations for 5wt% MoO_3.

Temperature/C	Combinations of Reaction Equations			
	1,2	1,4	2,3	3,4
400	104	103	100	99
450	111	100	87	76
500	150	113	127	90
550	142	94	121	73

Table 4: Summary of oxygen demands combinations for 10wt% MoO_3.

Temperature/C	Combinations of Reaction Equations			
	1,2	1,4	2,3	3,4
400	100	98	98	97
450	105	98	98	91
500	110	97	98	86
550	121	95	98	72

The 5wt% sample appears to operate via routes 2 and 3 at 400C, however at 450C the oxygen demand value cannot be corrected to 100% using routes 2 and 3 or 1 and 2, instead routes 1,4 appears to be operative. Therefore it appears that at 450C this sample operates via a completely different reaction pathway than the other two samples. However at 500C no combinations of the reaction pathways, calculated from equations 1-4 above, correct the oxygen demand to 100%, with all combinations being above or below this value. Oxygen demand values greater than

100% indicate a less oxygen consuming reaction pathway. The water gas shift reaction is one such reaction and is given below.

$$CO_{(g)} + H_2O_{(g)} \longrightarrow CO_{2(g)} + H_{2(g)} \qquad \text{Eqn 5}$$

Similarly, oxygen demands lower than 100% indicate further oxygen consuming pathways as well as the combinations of reactions 1-4 given above may be involved. The consecutive oxidation of carbon monoxide to carbon dioxide is an example

$$CO_{(g)} + 0.5O_{(g)} \longrightarrow CO_{2(g)} \qquad \text{Eqn 6}$$

It must be stressed however that the oxygen balances calculated from equations 1-4 indicate possible oxygen consuming reaction pathways. In order to obtain a fuller picture as to which reaction pathways are operating hydrogen and water product concentrations must be known. Therefore the data given in Tables 2-4 only gives a broad indication of possible oxygen consuming reaction pathways and changes in reaction pathways with temperature.

Mass and specific area normalised activities, are shown in Table 1. It is evident, from this table, that the specific activity of the 5wt% sample is generally higher than the other two samples over the temperature range of 400-500C. At the highest reaction temperature of 550C specific activities of the 5 and 10wt% samples are similar. However, at this temperature the specific activity of the 2wt% sample is higher than the 5 and 10wt% samples. Figure 1, clearly shows the relationship of specific activity with temperature for the molybdated zirconia samples. It is observed from Figure 1 that the 5wt% sample shows a dramatic increase in specific activity in the temperature range of 400-500C, which is as a consequence of higher methane conversion as discussed previously. The 2 and 10wt% samples display similar trends with respect to their specific activities over this temperature range, which are significantly lower than the 5wt% sample. Above 500C, the specific activity of the 5wt% sample begins to plateau, probably as a result of limiting oxygen conversion. This indicates that the 5wt% sample achieves a maximum rate of methane conversion at lower temperatures than the other two samples. The specific activities of the 2 and 5wt% samples, at this temperature, increases rapidly. Indeed the large

increase in the specific activity from 500 to 550C of the 2wt% sample is the largest increase experienced in this temperature range for all the samples examined.

Figure 1: Specific activity v reaction temperature for molybdated zirconia materials for the partial oxidation of methane.

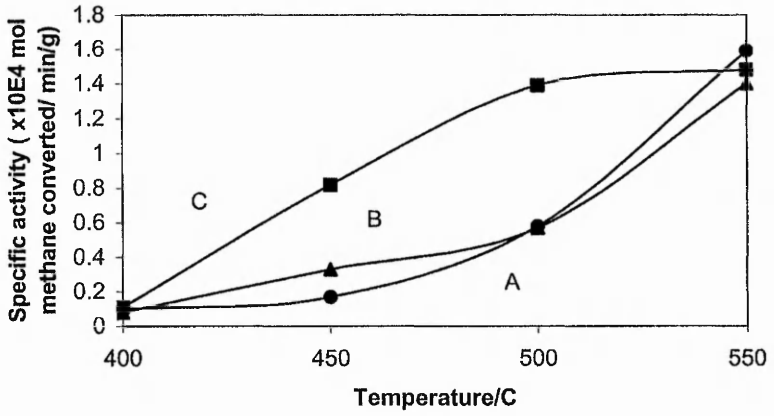

A-C =2, 10 and 5wt % molybdated zirconia samples.

It is observed from Figure 1 that the specific activities of the 2 and 10wt% samples appear to be further increasing above 550C. It may be further expected on the basis of oxygen conversions of the 2 and 10wt% samples that they will also display a reduction in the rate of increase of their specific activities above 550C. Therefore, above this temperature similar plateaus, as observed for the 5wt% sample, may be expected from the 2 and 10wt% samples. On this basis the plateau of the 10wt% sample may be below that of the 5wt% sample while that of the 2wt% sample may in fact be higher than that of the 5wt% sample. However, the similar specific activities observed at 550C maybe related to gas phase activity, which is known to be significant for this reraction at higher temperatures.

To further observe the differences between these materials methane combustion experiments were performed at atmospheric pressure in the temperature range 500-800C using conditions as given in Chapter 2. Methane combustion is an active area of industrial and academic research since this would be environmentally and economically beneficial, further discussion on methane combustion is given in the introduction to Chapter 5. Table 5 shows the reaction data for methane combustion at ambient pressure. This table shows a similar trend as those observed for molybdated

materials investigated for the partial oxidation of methane at elevated pressures, presented in Table 1. The activity results summarised in Table 5, for the molybdated zirconia samples, again shows the superior activity of the 5wt% over the other two samples, with the exclusive formation of carbon dioxide in the temperature range of 650-800C. The 2 and 10wt% samples were also active for the combustion of methane but apparently only at 700C and 800C respectively. At 700C the 2wt% sample produced carbon dioxide similar to the 5wt% sample, although at significantly lower methane and oxygen conversions.

Table 5: A summary of the reaction data for methane combustion at atmospheric pressure.

Sample	Temperature /C	Conversion[a] (%)		Selectivity[b] (%)		Carbon Balance[c] (%)	Oxygen Demand[d] (%)	Specific Activity[e] ($x10^{-5}$ mol CH_4 conv. g^{-1} min^{-1})
		CH_4	O_2	CO_2	CO			
	700	1.0	0.2	100	-	100	100	0.8
2wt%	750	-	-	-	-	86	96	-
MoO_3	800	-	-	-	-	87	95	-
	650	6.4	0.4	100	-	95	100	5.4
5wt%	700	7.6	0.8	100	-	96	99	6.4
MoO_3	750	8.4	1.3	100	-	97	99	7.1
	800	7.4	1.0	100	-	97	99	6.3
10wt% MoO_3	800	1.2	0.7	72	28	97	100	0.6

[a-e] See Appendix 1 for definitions.

The 10wt% sample, as well as producing carbon dioxide, also produced carbon monoxide at 800C. Pure zirconia was found to be ineffective for this reaction therefore the observed activity of the molybdated materials was related to the molybdate. The reduced activity of the 2wt% sample observed at temperatures in excess of 700C may relate to the low carbon balance ca. 87%, calculated in Table 5. Therefore it may be proposed that at high reaction temperatures carbon may be deposited on the surface of this sample. Further evidence and discussion with respect to the suspected carbon deposition is discussed later.

Hence in order to investigate the nature of the observed activity of these materials and to attempt to understand the increased activity of the 5wt% sample in both the combustion and partial oxidation of methane, a comprehensive characterisation study was performed.

.2.2: X-Ray Diffraction

X-ray diffraction patterns of the molybdated materials and undoped zirconia are shown in Figure 2. Figure 2a shows undoped zirconia which contains two characteristic reflections at ~28 and 31.5° 2θ (Cu K_α radiation) which are characteristic of the monoclinic phase of zirconia.

Figure 2: Powder x-ray diffraction patterns of molybdated materials

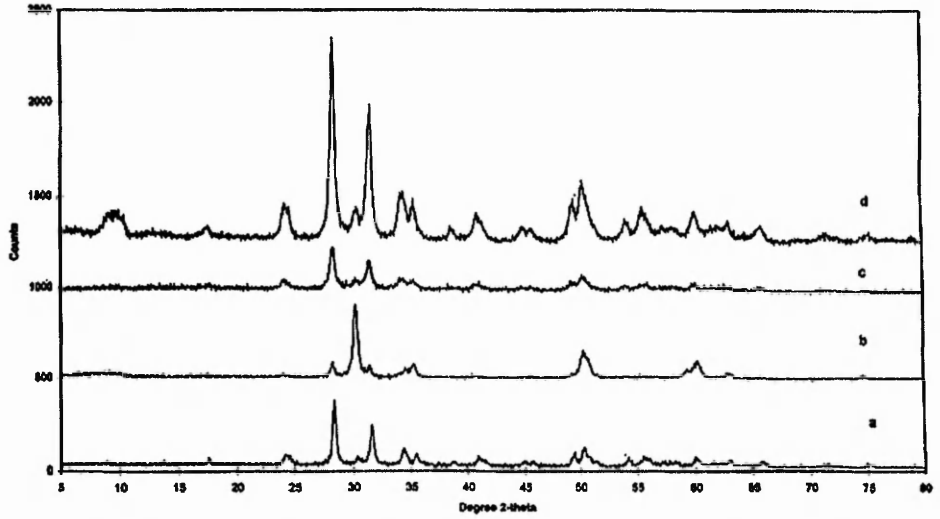

Powder X-ray diffraction patterns: (a) zirconia, (b) 10 wt% MoO_3/ZrO_2, (c) 5 wt% MoO_3/ZrO_2 and (d) 2 wt% MoO_3/ZrO_2.

(a) Zirconia, (b) 10wt% MoO_3/ZrO_2, (c) 5wt% MoO_3/ZrO_2 and (d) 2wt% % MoO_3/ZrO_2

On addition of 2wt% molybdate the intensity of these reflections is observed to increase with the appearance of a low intensity reflection at ~ 30° 2θ indicative of the tetragonal phase of zirconia. This reflection at ~30° 2θ increases with increasing molybdate loading and the x-ray diffraction pattern of the 10wt% sample is dominated by this reflection. This indicates a progressive change in the phase of the zirconia support with increased amounts of molybdate. The relative composition of the monoclinic and tetragonal phases can be quantified using the Toraya's method[132,133].

Hence in order to investigate the nature of the observed activity of these materials and to attempt to understand the increased activity of the 5wt% sample in both the combustion and partial oxidation of methane, a comprehensive characterisation study was performed.

.2.2: X-Ray Diffraction

X-ray diffraction patterns of the molybdated materials and undoped zirconia are shown in Figure 2. Figure 2a shows undoped zirconia which contains two characteristic reflections at ~28 and 31.5° 2θ (Cu K_α radiation) which are characteristic of the monoclinic phase of zirconia.

Figure 2: Powder x-ray diffraction patterns of molybdated materials

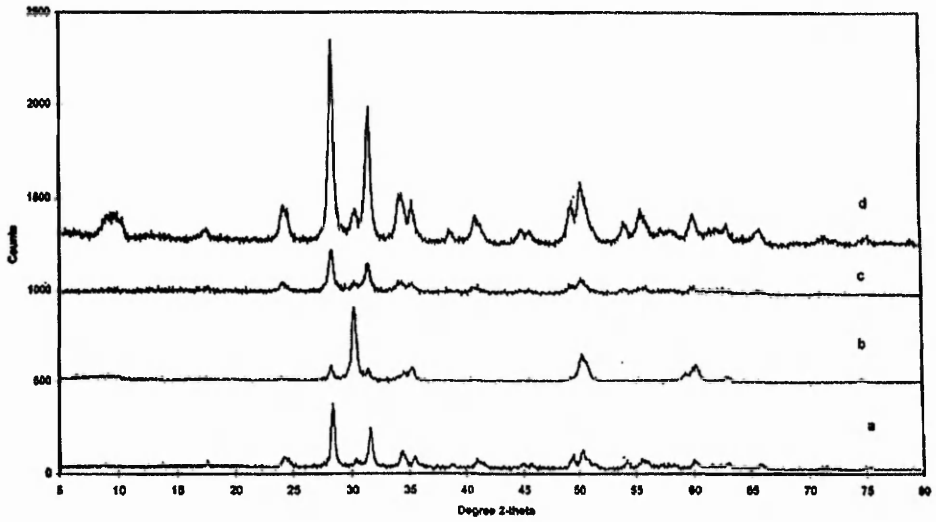

Powder X-ray diffraction patterns: (a) zirconia, (b) 10 wt% MoO_3/ZrO_2, (c) 5 wt% MoO_3/ZrO_2 and (d) 2 wt% MoO_3/ZrO_2.

(a) Zirconia, (b) 10wt% MoO_3/ZrO_2, (c) 5wt% MoO_3/ZrO_2 and (d) 2wt% % MoO_3/ZrO_2

On addition of 2wt% molybdate the intensity of these reflections is observed to increase with the appearance of a low intensity reflection at ~ 30° 2θ indicative of the tetragonal phase of zirconia. This reflection at ~30° 2θ increases with increasing molybdate loading and the x-ray diffraction pattern of the 10wt% sample is dominated by this reflection. This indicates a progressive change in the phase of the zirconia support with increased amounts of molybdate. The relative composition of the monoclinic and tetragonal phases can be quantified using the Toraya's method[132,133].

$$V_m = 1.311X_m/(1+0.311X_m) \qquad \text{Eqn.7}$$

Where, V_m= Volume fraction of monoclinic phase

and $X_m = I_{m(\bar{1}11)} + I_{m(111)} / I_{m(\bar{1}11)} + I_{m(111)} + I_{t(111)}$

I_m= Intensity of monoclinic reflections and I_t = Intensity of tetragonal reflections

Table 6: Volume of monoclinic and tetragonal phases, average crystallite size and specific surface areas for molybdate doped and undoped zirconia samples

Samples	V_m (%)	V_t(%)	Specific Surface Area m^2/g	<Å>
ZrO_2	90	10	17	522
2wt% MoO_3	92	8	26	413
5wt% MoO_3	87	13	33	202
10wt% MoO_3	37	63	48	376

V_M Volume % of monoclinic phase, V_t Volume % tetragonal phase and <Å> Average crystallite size measured from XRD patterns.

It can be seen from this table that the tetragonal volume % increases with increasing loadings of molybdate and the 2 and 5wt% samples are fairly similar. This indicates that the 2 and 5wt% mainly comprise monoclinic zirconia, and that the tetragonal phase forms as the molybdate loading is increased. As the difference in phase composition between the 2 and 5wt% samples is small then the enhanced catalytic activity observed for the 5wt% sample is not simply dependent on the phase of the zirconia support. The various loadings of molybdate are observed to stabilise the tetragonal phase, which indirectly follows the trend of increasing specific surface area. Therefore it may be implied that the addition of molybdate stabilises the tetragonal phase of zirconia, which produces the observed increase in specific surface area of the zirconia support. Figure 3 shows a relationship between the volume percent of monoclinic phase and specific surface area with molybdate loading. It is known that undoped zirconia can exist as several different phases, cubic, orthorhombic, monoclinic and tetragonal and that the formation of a particular phase is temperature dependent[133]. However it is known that a metastable tetragonal phase may be stabilised at high temperatures by the addition of various transition metal oxide dopants including molybdenum trioxide[134]. This phase has generally been reported in the literature as the high surface area and often more catalytically active phase compared to the monoclinic form.

Figure 3: Percentage volume of monoclinic phase and surface area as a function of molybdenum content.

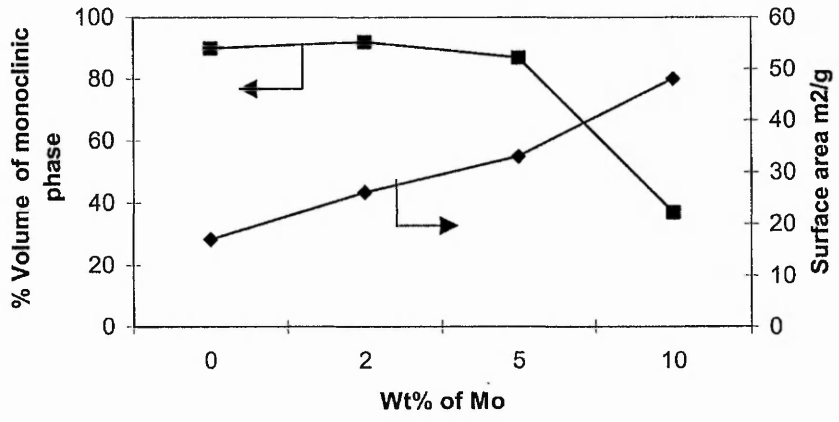

The addition of molybdate also has an effect on crystallinity. In the x-ray patterns in Figure 2 it is observed that the 2wt% sample increases the crystallinity of the zirconia support, while the 5wt% sample significantly reduces the crystallinity as indicated by the higher reflection intensity of the 2wt% sample. The 5wt% sample is also the least crystalline of all the samples characterised which is evidenced by the high background and low broad reflections. This indicates that this sample has a large degree of amorphous content, i.e particle sizes <30 Å, compared to the other samples and would suggest a larger specific surface area than measured in Table 6. The reduction in crystallinity of the 5wt% sample is the most significant difference between the samples. These observations can be explained in terms of a crystallite size effect and a gradual phase change related to molybdate loading. The addition of 2wt% molybdate increases the crystallinity of the zirconia support by increasing the proportion of monoclinic phase and this is observed as an increase in the intensity of the two characteristic reflections at 28 and 31.5 2θ, with the effective contribution of the reflection relating to the tetragonal phase being reduced. The addition of 5wt% molybdate reduces the crystallinity of the zirconia support by reducing the average crystallite size, shown in Table 6. This is observed to produce a 1.5 fold increase in the percentage volume of the tetragonal phase, which interestingly is similar to the increase in the measured specific surface area. The molybdate loading of 10wt% shows an almost complete phase change from the monoclinic to the tetragonal phase. This is accompanied with an increase in specific surface area and an increase in

crystallinity compared to the 5wt% sample. This is due to the greater stabilising effect on the tetragonal phase as a result of increased molybdate content. Garvie et al have shown that the metastable tetragonal phase of zirconia can only exist if the average crystallite size is > 300Å[135]. The average crystallite size of the 10wt% sample is similar to this value. However in this study no attempt has been made to differentiate between the tetragonal and monoclinic average crystallite size contributions and the average crystallite sizes given in Table 6, relates to the contribution of both phases. The reason for this is due to the high degree of amorphous content particularly in the 5wt% sample. Therefore obtaining sufficient reflections of the tetragonal phase with adequate resolution would be difficult with these materials.

It is also evident from the Figure 2, shown above, that there are no reflections relating to molybdenum. This is consistent with literature observations on molybdated or tungstated zirconia materials similarly prepared to those used in this study. Crystalline molybdenum and tungsten oxides generally display high intensity XRD pattern. Afanasiev studied the phenomena known as "solid-solid wetting", where solid molybdate and zirconia were mixed together at different concentrations 8-20wt% molybdenum content, and heated to 800C in a flow of dry air[86,87]. From XRD experiments the author observed an absence of reflections related to molybdenum, however this was found to be dependent upon molybdate content. At low loadings of molybdate ca. 8wt% no reflections were observed. Increasing the molybdate content ca. 20wt%, resulted in a chemical reaction between the molybdate and the zirconia support forming a $Zr(MoO_4)_2$ phase. This phase is clearly not evident in the samples investigated for this study, Figure 2. Further the author suggested that the molybdate spread over the surface of the zirconia to form a monolayer at low molybdate loadings. This monolayer formation was proposed to be a metastable state, which at higher loadings could no longer be maintained due to surface energy considerations. This resulted in a chemical reaction, taking place between the support and the molybdenum.

In summary the 2 and 5wt% samples show some similarities in terms of phase composition. Therefore the composition phase of the zirconia support may not in itself explain the differences in activity observed between the 5wt% and 2wt% sample. The high degree of amorphous content of the 5wt% sample may also relate

to the activity of this sample. The difference in activity between the 2, 5 and 10wt% samples relate to the differences in phase composition of the zirconia support, since the 2 and 5wt% samples are essentially monoclinic and the 10wt% sample has a high proportion of the tetragonal phase. The results of the x-ray diffraction show the significant influence of the molybdate on the zirconia support material.

4.2.3: Temperature Programmed Reduction

TPR experiments were performed on the pre-reactor molybdated zirconia samples and their traces are shown in Figure 4. Blank TPR experiments were performed on two types of zirconia. A zirconia sample prepared from the zirconium hydroxide calcined at 1000C for 24 hours in air, which was shown by x-ray diffraction to be monoclinic zirconia, and the second a 13wt% silica stabilised zirconia calcined at 900C, which was shown to be essentially the tetragonal phase of zirconia. TPR traces of both blank experiments both showed the monoclinic and tetragonal phases of zirconia are not reduced under the conditions employed. Therefore the peaks observed for the molybdated zirconia samples in Figure 4 are due to the presence of the molybdate species. The TPR profiles of the 2 and 5wt% are similar and show two peaks at similar temperatures of reduction, which suggests that the molybdate species in both samples are similar. However, the TPR of the 10wt% sample shows some additional features. An asymmetry is evident at the lower temperature maximum which may consist of two overlapping peaks. An additional high temperature peak is observed at 832C as well as a peak at 700C similar to that of the 2 and 5wt% samples, which suggests the presence of two types of molybdate species. Table 7 summarises the data from the TPR experiments. The K-values given in this table is a parameter which takes into account the hydrogen flow rate, concentration of hydrogen and the number of reducible species and is given by the equation below.

$$K = \delta_o/(V\ L) \qquad \text{Eqn. 8}$$

where, δ_o = moles of reducible species μmol

L= Concentration of hydrogen in μmol/ml

V = Hydrogen flow rate in ml/second

Figure 4: Temperature programmed reduction spectra of molybdated materials

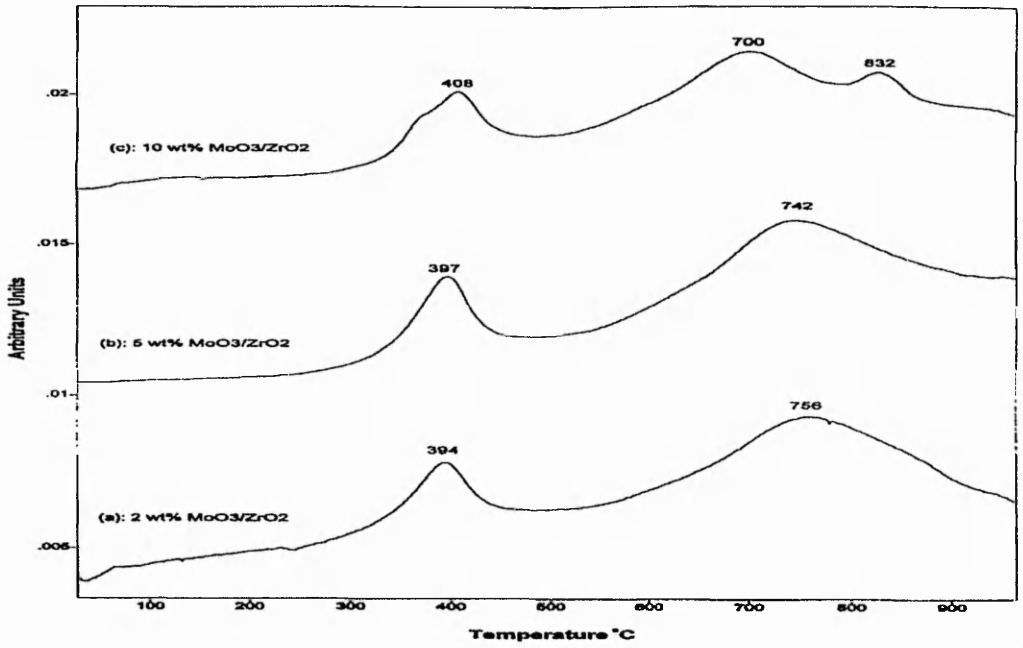

It is known that the above parameters can affect the TPR profiles[194]. Since both the 5 and 10wt% samples have essentially the same K-value and the same mass of reducible species, experimental artefacts, which can alter the positions and number of TPR peaks[194], can be excluded. Therefore the additional peaks observed for the 10wt% sample are due to different molybdate species being reduced. The different species of molybdate on the 10wt% sample may be expected, as the zirconia phase composition of the 10wt% sample is significantly different to those of the 2 and 5wt% samples.

It is interesting to note that in comparison with the bulk molybdate TPR profiles of the molybdated zirconia samples showed peak maxima at lower temperatures. This is consistent with the observations of Parmaliana et al[136]. In comparing the peak maximum for the molybdated samples it is evident that the temperature of the first maximum increases with increasing molybdate loading and for the second peak maximum this trend is reversed. This indicates that the first stage in reduction is less facile at higher loadings of molybdate. The decrease in the second temperature maxima indicates that the intermediate molybdenum oxo species once formed

becomes more readily reduced with increasing molybdate loading. A two-stage reduction of molybdenum (VI) oxide to the molybdenum metal, is the commonly accepted process i.e.

$$MoO_3 + H_2 \longrightarrow MoO_2 + H_2O \xrightarrow{H_2} Mo \qquad \text{Eqn. 9}$$

By measuring the peak areas of all the samples and normalising them to the hydrogen consumed per unit area of a copper (II) oxide standard, the amount of hydrogen consumed at each stage of reduction for each sample was calculated. The use of copper (II) oxide is a standard procedure in TPR analysis. The moles of hydrogen consumed normalised to copper (II) oxide is given in Table 7.

Form this table it is evident that the 5wt% sample has the largest hydrogen consumption than the other two samples, in line with the observed catalytic activity for this material. Taking the ratio of pk_1:pk_2 provides an indication as to the relative ratio of hydrogen consumed at each stage of the reduction, thereby allowing possible reduction routes to be postulated. The peak ratios of both the 2 and 5wt% sample are similar, 0.25, which indicates that the route to molybdate reduction are similar and is consistent with the reduction passing through a +4 and/or +5 oxidation state.

Since the ratio of the 10wt% sample is similar to that of the bulk molybdenum material, 0.48 and 0.55 respectively, this may imply that the route to reduction is similar in both samples. The ratios for both materials are consistent with the reduction of the molybdate passing through a +4 oxidation state only before complete reduction to the metal as given by equations 3 and 5 above. The differences in reducibility between the 2 and 5 with the 10wt% sample may relate specifically to the interaction of the molybdate with the zirconia support where at least the phase composition of the zirconia may be important.

Using equation 9 above to calculate a theoretical maximum hydrogen consumption and by comparing these values to the total amount of hydrogen consumed by each sample, it is possible to calculate the percentage amount of molybdate reduced in each sample. Table 7 shows the percentage amount of molybdate reduced and shows that the bulk molybdate material is completely reduced.

Table 7: A summary of the temperature programmed reduction studies on molybdated zirconia samples

Sample	Peak maxima/C			K-Value /sec.	Hydrogen consumption in (x 10^{-5} mole of H_2 normalised to CuO)				% Amount of MoO_3 Reduced based on Eqn9
	1	2	3		1	2	3	Total	
MoO_3	610	793	-	100	27	13	-	40	100
2wt% MoO_3/ZrO_2	394	756	-	27	1.1	4.0	-	5.1	46
5wt% MoO_3/ZrO_2	397	742	-	65	2.8	8.4	-	11.2	43
10wt% MoO_3/ZrO_2	420	710	842	67	2.4	4.4	0.4	7.2	27-61

First Stage Reduction

$$2MoO_3 + H_2 \longrightarrow Mo_2O_5 + H_2O \quad \text{Eqn. 10}$$

$$MoO_3 + H_2 \longrightarrow MoO_2 + H_2O \quad \text{Eqn. 11}$$

Second Stage Reduction

$$Mo_2O_5 + H_2 \longrightarrow 2Mo + 5H_2O \quad \text{Eqn. 12}$$

$$MoO_2 + 2H_2 \longrightarrow Mo + 2H_2O \quad \text{Eqn. 13}$$

The molybdate samples all show percentage reduction significantly less than the bulk molybdate material with 40-60% reduced. The 2 and 5wt% samples both show similar percentage amounts of molybdate being reduced ca.45 %. The 10wt% sample appears to have the highest percentage loading, 60%, however some care must be taken within this result since the peaks are very broad, several baselines are possible. Therefore the percentage reduction for this sample is in the range 30-60%. Taking an average value produces 45%, which is similar to both the 2 and 5wt% samples. However the values of all the samples showed that >50% of the molybdate is not reduced. This may indicate that molybdate is bound strongly to the surface of the support encapsulated or present in a lower concentration than that used in the

synthesis and that the composition of the zirconia support is unimportant in this respect.

4.2.4: Laser Raman Spectroscopy

Laser Raman spectroscopy has been extensively reported in the literature for molybdated materials due to the high sensitivity of molybdenum oxide species for this technique. Characteristic molybdenum oxide species are observed at wavenumbers, above ca. 650 cm^{-1}. Figure 5 shows the Raman spectra of the pre-reactor molybdated materials in this region, which were kindly obtained by Dr S.H. Taylor at Cardiff University. Some spectra have been affected by cosmic interference, which produces sharp bands such as that at 872cm^{-1} in the 2wt% molybdated zirconia spectrum. From Figure 5, bands at ca. 878 and ca. 915 cm^{-1} are present in all samples. Assignment of Raman bands observed in Figure 5, comes from the analysis of the relevant literature. Smith et al studied molybdated silica materials with various loadings of molybdenum[137]. The authors observed three types of molybdenum oxo species, which were dependent upon molybdate content. Raman bands at ca.850-900 cm^{-1} were assigned to Mo-O-Mo bridging oxygen sites found in surface coordinated polymolybdate species and bands at ca. 818 and 995 cm^{-1} were assigned to bulk molybdate oxo species Mo=O. Bands related to the silicomolybdate species occur at 930-977 cm^{-1}. Therefore the bands observed at 878 and 915 cm^{-1} in Figure 5 may be related to coordinated surface species, which appear to be present in all the molybdated zirconia samples. As molybdenum loadings increase bands at ca. 989 and 816 cm^{-1} are apparent and increase in intensity with increasing molybdenum loading. The positions of these bands are in similar positions as those assigned by Smith et al for bulk molybdenum oxo species[137]. Therefore, these bands observed for the 5 and 10wt% samples are assigned to bulk molybdenum oxo species. However Zhao et al in their comparative studies of molybdate doped on hydrous and crystalline zirconia materials, using a preparation method similar to that used in this study, observed a band at 814 cm^{-1} and a band at 960 cm^{-1}[88].

The authors assigned the band at 814 cm^{-1} to the formation of a new molybdate surface state, denoted by Mo-O-Zr, similar to that found in the studies by Smith et al and the band at ca. 960 cm^{-1} to two dimensional polymolybdate, (TDPM), species. Since this band was only present in the molybdated zirconia samples prepared by impregnation of the hydrous zirconia, Zhao et al concluded that this new surface

species was responsible for superacidity. In this study the presence of both the bands at ~816 and 989 cm^{-1} indicates the presence of bulk molybdate in accordance with the findings of Smith et al and not to any kind of superacidic surface molybdate species.

Figure 5: Raman spectra of pre-reactor molybdated zirconia materials

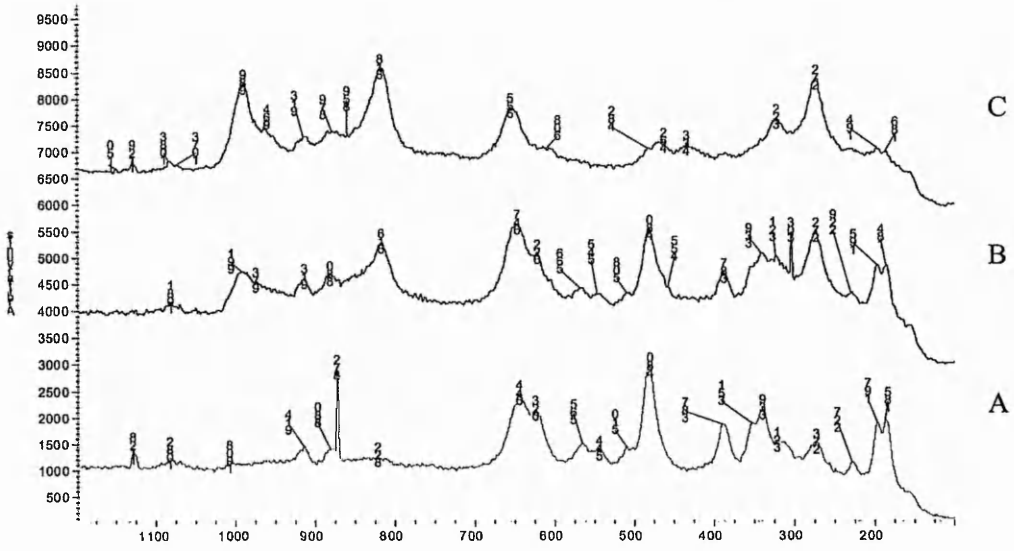

(A) 2wt% MoO_3/ZrO_2, (B) 5wt% MoO_3/ZrO_2 and (C) 10wt% MoO_3/ZrO_2

Therefore it is assumed that the 2wt% contains only polymolybdate species and at higher loadings this species is still present. On increasing the molybdate loading bulk molybdate species become more evident on the surface of the support material.

Raman spectra below 650 cm^{-1} are consistent with the x-ray diffraction observations and show the zirconia support of the 2 and 5wt% sample to be similar. This is in contrast to the observations discussed previously, for the molybdate spectral region, which showed the molybdenum oxo species in 5 and 10wt% samples to be similar. It is observed from Figure 5 that bands at ca.184,195,272,352,387 and 480 $cm^{-1}$are observed in all the samples. However, with the exception of the bands at ca. 272 and 352 cm^{-1}, the intensity of these bands decreased with increasing molybdate loading. Similarly additional bands at 466 and 429 cm^{-1} begin to appear in the 10wt% sample. Phillipi et al in their studies on zirconia polymorphs tabulated values of monoclinic, tetragonal, yittria stabilised cubic and cubic zirconia phases[138]. These authors found

that strong bands at ca. 263 and 418 cm^{-1} related to the tetragonal phase and the bands ca. 272 and 348 cm^{-1} were characteristic of the monoclinic phase, assuming no straining effects were present in the crystals. Therefore, the bands at ca. 184,195,387 and 480 $cm^{-1}$are related to the monoclinic zirconia phase, which correlate with x-ray diffraction studies discussed previously, indicating the percentage of monoclinic phase decreases with increasing molybdate loading. It is apparent that Raman bands relating to the tetragonal phase are weaker than those relating to the monoclinic phase, particularly in the 10wt% sample, which has the greatest percentage of tetragonal content on the basis of the x-ray diffraction studies, discussed previously. It is known that the tetragonal phase is also a weaker Raman scatterer than the monoclinic phase[138].

Therefore it may be concluded from the Raman experiments that there is no unique molybdenum oxo species present in the 5wt% sample. Instead this material appears to be between the 10 and 2wt% samples in terms of its similarity in the molybdate Raman region and zirconia region respectively. However the unique position of the 5wt% sample in terms of the polymolybdates and an amount of bulk molybdate species supported on a monoclinic zirconia phase may explain its enhanced activity over the 2 and 10wt% samples. Taking the TPR and Raman results together, it appears that although the form of molybdenum oxide in the 5 and 10wt% samples is similar, its reducibility is different. It is probable that this relates to the phase composition of the zirconia substrates, with reduction occurring at lower temperatures on the monoclinic form. This correlates with the higher activity of the 5wt% sample, since a relationship between reducibility and oxidation activity has been observed[136]. Although one of the higher temperature maxima occurs at lower temperatures in the 10wt% sample, remaining maxima both occur at higher temperatures compared to the 2 and 5wt% samples.

An important consideration is whether the forms of molybdenum oxide species observed in the Raman studies are representative of those under reaction conditions. Since the Tamman temperature of molybdenum (VI) oxide is only 261C[139], the highly dispersed MoO_3 crystallites will be mobile during reaction. One possibility is that they disperse over the surface of the support, forming a monolayer like species. Afanasiev et al studied the kinetics of sintering of a 7wt% molybdenum zirconia and pure zirconia at 700C[87]. The surface area, of the pure zirconia sample declined

linearly, while the surface area of the molybdated zirconia sample declined rapidly until its surface area stabilised. The point at which the surface area of this sample stabilised was thought to be due to the formation of a metastable state, where the molybdate was thought to form a monolayer. In discussing the thermodynamics of the observed sintering behaviour, the authors stated that sintering of a surface is driven by the surface free energy of the solid. In pure zirconia the chemical composition of the surface is the same as the bulk, and during sintering atoms move from the surface to the bulk to satisfy the cation co-ordination sphere. In a multi-component system the chemical composition of the surface differs from the bulk and a redistribution of the atoms occurs during sintering. However this depends on the interaction between the support and the impregnated metal oxide. In molybdated samples where there is insufficient molybdenum to form a surface monolayer, rapid sintering occurs in the regions where there is no molybdenum covering the surface until the zirconia surface area coincides with a monolayer coverage. At high calcination temperatures this metastable state may be lost due to either molybdenum sublimation or to the formation of a new bulk phase. The proposal by the authors was governed by two constraints, which must be satisfied in order for the formation and retention of the metastable state.

(I) The solid dispersions must contain only one phase

(II) The supported component remains entirely on the surface

If only one of the above constraints are true then the metastable state is not formed. Taking the cross-sectional area of an MoO_3 in the catalysts synthesis mixture to be $15Å^2$ [140] the coverage corresponds to 48, 97 and 131% of a monolayer for the 2,5 and 10wt% samples respectively, based on the surface areas reported in Table 1. An example of the calculation is given below for the 5wt% sample.

e.g: ***Sample calculation for the 5wt% sample***

Mass of molybdenum oxide per gram of zirconia, (5/100) x 1g = 0.05g

Number of moles of molybdenum oxide = 0.05 g/144 g mol^{-1} = 3.47*E10-4 mol.

Molecules of MoO_3 = 3.57*E-4 mol. x 6.022*E23 mol^{-1} = 2.15*E20

Area of MoO_3 per gram of zirconia = 2.15*E20 x 15*E-20m^2= $\underline{32\ m^2\ g^{-1}}$

Monolayer coverage = (32 m^2g^{-1}/ 33 m^2g^{-1}) x 100 = ***$\underline{97\%}$***

If catalytic activity is associated with monolayer like species, an additional possibility is that the presence of excess molybdenum oxide in the 10wt% sample could inhibit activity by blocking active sites. The lower activity observed for the 2wt% sample may be due to the reduced number of sites i.e 0.5 of a monolayer.

4.2.5: Post Reactor Analysis

X-ray diffraction

Post reactor XRD analysis of molybdated samples investigated for methane combustion is given in Figure 6. The figure indicates that all samples have a large degree of amorphous content post reaction, due to the high background observed for these materials.

Figure 6: Powder x-ray diffraction of post reactor molybdated zirconia samples

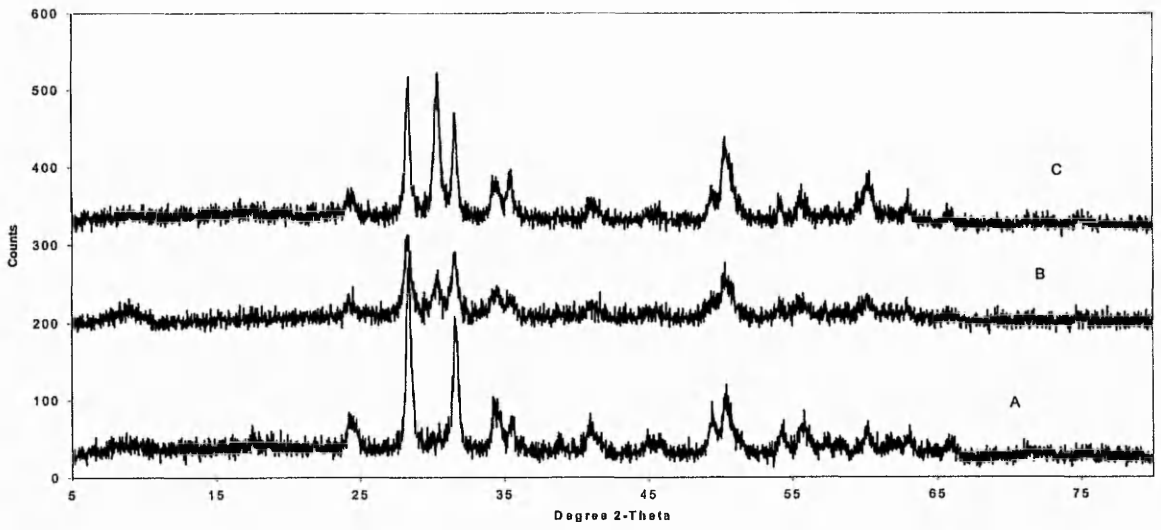

(A) 2wt% MoO_3/ZrO_2, (B) 5wt% MoO_3/ZrO_2 and (C) 10wt% MoO_3/ZrO_2

However, the intensity of the reflections for the 2 and 10wt% samples appear to be similar while the intensity of the 5wt% is slightly higher. This indicates that although all samples are essentially amorphous, the 5wt% sample displays a greater degree of crystallinity. Further in comparison with the post reactor XRD patterns with their

pre-reactor counterparts the 10wt% samples shows the appearance of characteristic reflections associated with the monoclinic phase of zirconia, which was not evident in the pre-reactor sample. The 5wt% post-reactor sample appears to be similar, in terms of the dominating monoclinic phase, as its pre-reactor counterpart. Similarly the 2wt% sample shows a decrease in the intensities of reflections relating to characteristic monoclinic and tetragonal phases, as observed for its corresponding pre-reactor XRD pattern.

Table 8 shows the volume fraction of the monoclinic and tetragonal phases, calculated from Toraya's method as given in equation 8. The volume of the monoclinic phase for zirconia is similar to that of its pre-reactor counterpart. The 10wt% sample shows the greatest difference in comparison with the pre-reactor sample, showing a large increase in the volume of the monoclinic phase, indicating that under the reaction environment a phase transformation occurs. However, it is evident that there is still a large proportion of the tetragonal phase present. Similarly, the 5wt% sample displays an increase in the volume of the monoclinic phase, compared to its pre-reactor sample. The volume of the monoclinic phase for the 2wt% post reactor sample is observed to decrease, by 6%, in comparison to its pre-reactor counterpart. This is unusual since the phase transformation is from the tetragonal to the monoclinic phase, which is stable at higher temperatures. This may be due to a reduction in the specific surface area of this material, which would then imply a greater effective molybdenum coverage.

Table 8: Volume of monoclinic and tetragonal phases for post-reactor molybdate doped and undoped zirconia samples

Material	Volume (%)	
	Monoclinic Phase	Tetragonal Phase
ZrO_2	93	7
2wt% MoO_3/ZrO_2	86	14
5wt% MoO_3/ZrO_2	93	7
10wt% MoO_3/ZrO_2	70	30

The effective increase in molybdenum coverage may give rise to a greater volume of the tetragonal phase over the monoclinic phase being observed in the XRD pattern. Also the amorphous sample may crystallise during reaction.

Laser Raman Spectroscopy

Raman spectra given in Figure 7, for the post reactor combustion molybdated samples show that molybdenum oxo species are evident after the reaction for the 5 and 10wt% samples only. Bands characteristic of bulk molybdenum oxide at ca. 987 evident in the 5wt% sample and Raman bands at ca. 815 and 980cm^{-1} are evident in the 10wt% sample. However for the 2wt% sample there are no Raman bands evident above ca 640 cm^{-1} indicating the absence of any molybdenum oxo species. This may be due to the loss of molybdenum by sublimation under the reaction conditions. Consistent with the post reactor XRD analysis, discussed above, the bands at ca. 190 and 180cm^{-1} are observed to in 10wt% sample shows characteristic bands associated with the monoclinic phase ca. 190 and 180cm^{-1} and these bands are observed to be of a higher intensity

Figure 7: Raman spectra of 2 and 5 wt% post-reactor molybdated zirconia samples

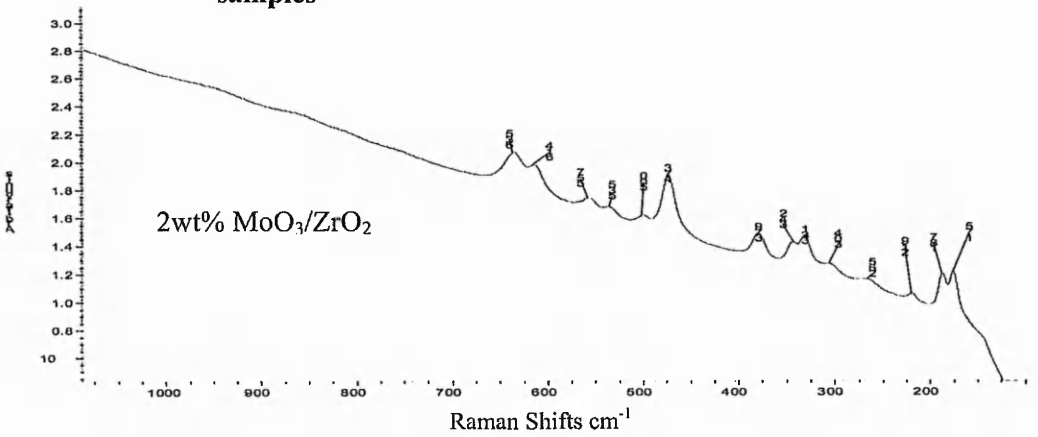

Figure 7 cont. : Raman spectrum of 10 wt% post-reactor molybdated zirconia samples

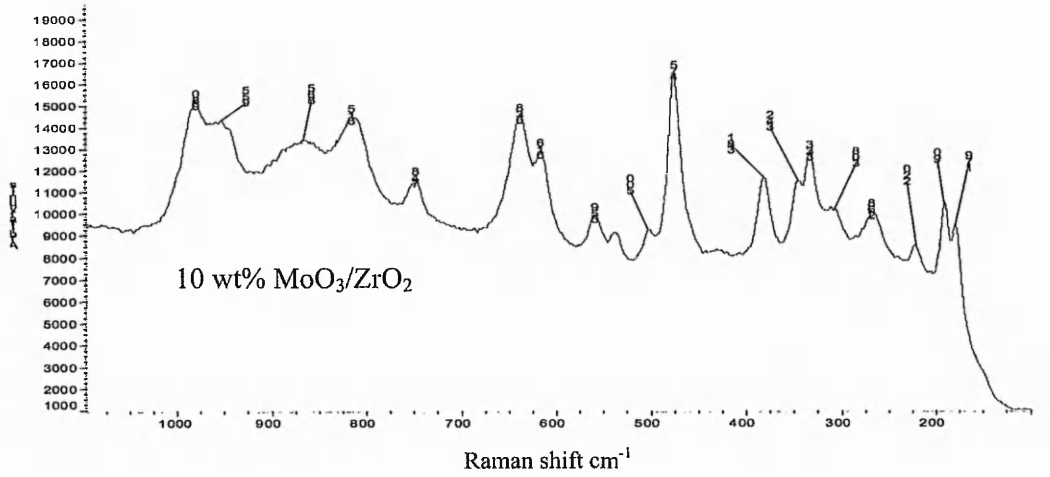

4.3: Conclusions

The 5wt% sample shows an enhanced activity for both the partial oxidation and combustion of methane. Characterisation studies shows that the 5wt% sample follows the general trends in terms of surface area, stability to a degree of the zirconia tetragonal phase and reducibility of the molybdenum species. However the activity of the 5wt% material can be explained in terms of its unique place between the 2 and 10wt% in terms of phase composition and monolayer coverage of the molybdenum. Therefore the question is, is the behaviour of the molybdenum oxide species in the reactions consistent with its behaviour in the ex-situ Raman studies

5.0: CATALYTIC COMBUSTION OF METHANE

5.1: General Introduction

Combustion technology covers an extremely wide field, including systems such as automobiles[141-143], aircraft after burners[144,145], heat extraction systems[146] and "end of pipe" gas abatement technology e.g volatile organic compounds (VOC's)[147,148]. The ideal products of combustion are carbon dioxide and water. However, due to inefficient combustion, carbon monoxide is formed and at the high flame temperatures nitrous oxides may also be formed.

Carbon monoxide formed by the incomplete combustion of fuel is believed to be a " greenhouse" gas. Nitrogen oxides, known as NO_x are formed via several mechanisms, the most important of which is given by the Zeldovich mechanism, for the formation of thermal NO_x[141].

$$O_2 + M \rightleftharpoons 2O + M$$
$$N_2 + O \rightleftharpoons NO + N \quad \text{Rate determining step}$$
$$O_2 + N \rightleftharpoons NO + O$$

Where M=Any molecule which cam act as an energy transfer agent.

Therefore, carbon monoxide and NO_x are considered environmental pollutants and as such have become the subject of stringent environmental control. The automobile industry, one of the first affected by the legislation, attempted to resolve the problems by employing an "end of pipe" solution. This involved the use of a 3-way catalyst based on Pt/Rh/Pd with various additives such as ceria, to improve catalyst performance[143]. Further developments in the automobile industry saw the development of the "lean burn engine" which operates at a lower fuel:air ratio, thereby increasing the combustion efficiency.

Recent research efforts in the area of combustion technology, stimulated by environmental requirements, is the redesigning of combustion systems[149,150]. This is essentially to prevent the formation of carbon and nitrous oxides by using a catalyst to lower the high flame temperatures required for the homogeneous gas phase combustion or at least to initiate the combustion process. The use of a catalyst in a combustion process may offer the following advantages:

1. Catalytic combustion can be carried out over a wide range of fuel concentrations.
2. Suitably active catalytic materials are able to activate fuel at lower temperatures and these temperatures can be more easily controlled.
3. Lower combustion temperatures result in reduced NO_x emissions.

Conveniently, combustion process can be divided into two areas, a high and a low temperature regime. However the potential use of many types of materials for combustion suffer from several disadvantages depending upon the regime used.

Low Temperature Combustion <1000C

- High catalytic activity is required at as lower temperatures as possible, thereby limiting the use of many materials for this reaction.
- The higher toleration of the catalyst towards potential poisons in the fuel such as nitrogen and sulfur containing compounds and steam is necessary.

High Temperature Combustion >1000C

- The catalytic material must be thermally stable i.e low volatility.
- The catalyst support must also be thermally stable and maintain a reasonable surface area.

Higher temperature combustion processes will not be discussed further, however several reviews exist in the literature on this field e.g[149].

Combustion processes generally follow a sigmoidal type curve as a function of temperature; an example is given in Figure 1. In the homogeneous reaction, radicals are formed in the gas phase, which then undergo further oxidation in a complex reaction mechanism. Typical flame temperatures may rise well above 1000C where NO_x may be formed. The use of a catalyst, results in the controlled ignition of the fuel, section A. The activity of the catalyst is crucial in lowering the ignition temperature. As the reaction proceeds, heat is generated and this results in a rapid increase in the reaction rate and "light off" occurs, section B. Section C, indicates an area where the reaction rate is no longer a function of the reaction temperature. The rate of the reaction is dominated by the transport of reactants to the surface. The

reaction at this stage is said to be mass transfer limited. At even higher reaction temperatures the homogeneous reaction rate dominates and the role of the catalyst is to increase the rate of reaction by generating radicals. At these temperatures it is usually the thermal stability of the catalyst support which determines the activity behaviour i.e surface area, as differences in specific activity between catalytic materials are governed by mass transport effects.

Figure 1: A typical rate curve for catalytic combustion process[182]

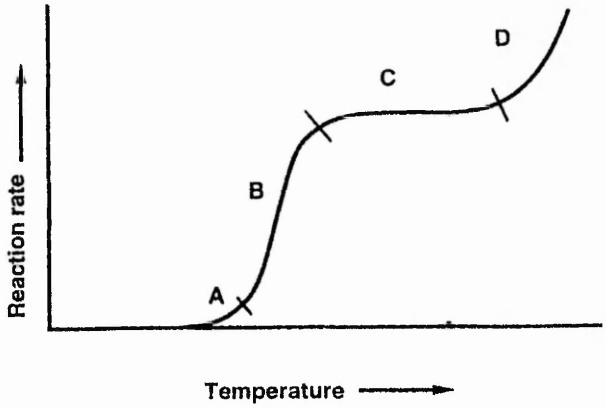

Typical rate curve for catalytic combustion. (A) Ignition, (B) Light-off:mass transfer limitation and (D) Homogeneous gas phase reactions

Trimm et al developed a relationship between the metal-oxygen bond strength and the rate of hydrocarbon oxidation[151]. This may be shown as a volcano type plot, shown below, Figure 2, for the oxidation of propylene over a series of metal oxides and noble metals[152].

From Figure 2, two points are clear. Firstly, noble metals show the highest activity for propylene oxidation and secondly metal oxides also show good activity for the reaction. This is reflected in the literature where a vast majority of studies on combustion use noble metals. More recently studies on metal oxides have appeared with increasing regularity. Generally two classes of compounds have been identified and studied for catalytic combustion, these are noble metals and metal oxides. The latter can be further subdivided into simple oxides e.g copper oxide and iron oxide

and complex metal oxides e.g binary mixed metal oxides and perovskites. In general studies have been performed on VOC's and hydrocarbons.

Figure 2: Volcano type plot for the oxidation of propylene as a function of metal-oxygen bond strength[152]

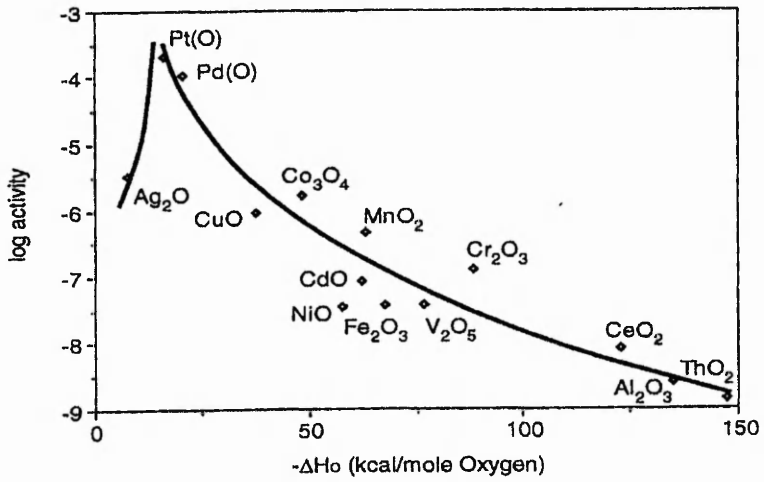

Particular attetion has been paid to methane, since it is the most difficult hydrocarbon to combust, due to the higher C-H bond strength and is present as a major component in many fuels[153].

5.1.2: Noble metals

In the literature noble metals have been employed for the complete combustion of hydrocarbons, carbon monoxide and VOC's [154-157]. However due to problems with the high volatility of some metals e.g iridium, their use has been limited to palladium, platinum and rhodium. However studies involving rhodium are much less than its platinum and palladium counterparts, and these have mainly been limited to exhaust catalysis. Indeed the use of palladium and platinum arises from their higher activity towards hydrocarbons, ease of preparation i.e dispersion of particles on various supports and their apparent resistance to sulfur poisoning. Reported in the literature is a rationale which indicates that the activity of palladium is greater than platinum for the combustion of methane, however platinum is better for hydrocarbons > C_3

[158,159]. This is an apparent anomaly since the difficulty in combusting hydrocarbons should on the basis of the C-H bond strength, decrease with increasing carbon number. Therefore it would be expected that palladium should display greater activity for hydrocarbons $>C_3$[158]. Therefore the superior performance of palladium over platinum is not simply a function of carbon number, but of factors such as preparation, testing conditions and/or the effects due to adsorbed products.

The use of supported noble metals are thought to be structure sensitive[159-161]. Briot et al observed an increase in the turnover frequency (TOF) with increasing palladium particle size from 7 to 16 nm after ageing the sample at 600C[162]. Further the enhanced activity of the aged $Pd/\gamma\text{-}Al_2O_3$ sample was attributed to the higher reactivity of adsorbed oxygen. The same authors made similar observations for platinum, however the enhancement in the activity per platinum surface atom was less marked than that for palladium. Structure sensitivity for platinum and palladium was not observed from several authors. Hicks et al ascribed large variations in TOFs for methane oxidation over supported platinum and palladium catalysts to the difference in the nature of the supported active phase[161,163]. Catalysts with high initial metal dispersions (small crystallites) exhibited oxidation of the metal under operation, in a small excess of oxygen and temperatures below 370C. The resulting catalyst behaved as a noble metal oxide supported on an oxide carrier. The larger metal particles from a catalyst with lower initial dispersion were only partially oxidised. In all cases, the noble metal phase was believed to be covered with oxygen under reaction conditions. The chemisorbed oxygen covering the crystallites was far more reactive toward methane than the noble metal oxide from the highly dispersed supported metal. This is expressed by TOFs that are 1-2 orders of magnitude higher. The reported structure sensitivity is higher for palladium, which also shows complete oxidation and much higher activity than platinum. This theory is supported by the work on supported platinum catalysts, reported by Otto[164]. Baldwin and Burch could not distinguish a clear relationship between the metal particle size and reactivity for the palladium catalysts[161]. However, they noticed an activation of the catalyst when kept under reaction conditions, involving a large excess of oxygen and temperatures between 350-400C. They did not notice this activation upon exposure to air and concluded therefore that the activation was due to interaction of the catalyst with the reducing agents, inducing a change in catalyst morphology.

5.1.2: Metal Oxides

Metal oxides can be preferred over noble metals because of their low cost, ease of availability and their heat resistive nature, particularly for ceramic materials. However in general the catalytic activity of metal oxides are much lower than their noble metal counterparts. However several studies have been performed initially on simple oxides based on iron[165], manganese[166] and copper[167] and more recently on mixed metal oxides e.g: ceria/zirconia[168], hexaluminates[169] and perovskites. While the latter two materials are of interest, their activity is in general much lower than either the simple or mixed metal oxides, however these materials display very good thermal conductivity at high temperatures and therefore makes them of interest as catalyst supports.

Simple and mixed oxides

Simple metal oxides, which show variable oxidation states as well as the properties mentioned above have been investigated for complete combustion. Specifically metal oxides from the first row transition elements, Co, Fe, Mn, Cr and Cu, have all been investigated to varying degrees and display activity for combustion. In general these materials as well as being relatively inexpensive, compared to noble metals, are able to reduce the formation of NO_x and are more tolerant to poisons such as sulfur. However the main problem with simple oxides is their thermal stability particularly at high temperatures, where phase changes often occur.

Normal Spinel $Co_3O_4 \longrightarrow CoO \quad T>450C$

Non-Stoichiometric $\gamma\text{-}Fe_2O_3 \longrightarrow \alpha\text{-}Fe_2O_3 \quad T>650C$

Phase changes usually reduce the specific surface area, but more importantly reduce the number of active sites therefore reducing catalytic activity or at least the specific activity. More recently ceria, a flourite type lanthanide series oxide has been used in the automotive 3-way exhaust catalyst for the removal of hydrocarbons, CO and NO_x. A review on the industrial applications of ceria is given by Trovarelli et al[168]. Materials based on ceria have attracted significant attention for the oxidation of CO and hydrocarbons because of its physiochemical properties[168].

1. Oxygen storage capacity.
2. Redox couple $Ce^{III/IV}$
3. Oxygen mobility i.e. the formation of oxygen vacancies by cation substitution.

Trovarelli et al studied cerium oxide isovalently substituted with hafnium and zirconium oxides for methane combustion at high space velocities[198]. These materials were found to be active for methane combustion with temperatures for 10 and 50% methane conversion to carbon dioxide being 457/542C and 462/557C for ceria/haffnia and ceria/zirconia respectively. From temperature programmed reduction experiments, the author concluded that the improved activity for these materials was due to the enhancement of oxygen mobility of the flourite structure due to cation isovalent substitution, which increased the ability of ceria to shuttle between the two oxidation states of +4 and +3. These materials showed good activity compared to Pt/CeO_2 tested under comparable reaction conditions. However a better comparison may have been with $Pt/\gamma\text{-}Al_2O_3$ since the surface area of this material is much higher than the ceria/haffnia ceria/zirconia samples and the data reported may be affected by the dispersion of platinum particles, produced under low temperature reduction. Similar observations and conclusions were proposed by Keshavanjan et al for the combustion of n-butane using 3d-transition metal oxide stabilised zirconias[170,171]. In their study the materials were compared to a high surface area 48 m^2/g Pt/ZrO_2 material which showed the lowest temperatures for 10 and 50% n-butane conversion to carbon dioxide. The best fluorite sample examined was the high surface area 105 m^2/g $Zr/Mn_{0.2}O_2$ material. The oxidation of CO and methane was investigated using ceria and silver doped copper[172]. The authors found that stabilising the ceria surface area with lanthana, or zirconia decreases sintering while maintaining catalyst activity. The stabilisation of zirconia by the addition of dopants such as lanthana or ceria has been documented in the literature[173,174]. However the authors found a synergistic effect by adding copper or copper and silver to ceria producing a strong interaction between the transition metal(s) and the support which increases the reduction of surface oxygen on ceria as well as the oxygen uptake ability at loadings <5 at%.

The use of fluorite type structures in combustion reactions is not new, Claudell et al[175] in 1969 studied CeO_2-La_2O_3, CeO_2-ThO_2 and UO_2-ThO_2 oxides for methane and CO oxidation. Claudell et al described the fluorite type structures as an "oxygen sponge" forming interstitial superficial oxygen atoms which form during successive oxidation/reduction cycles and are able to form sites able to chemisorb carbon monoxide. Therefore the use of ceria/zirconia and ceria/haffnia mixed oxides show potential use as a combustion catalyst. This is envisaged by the growing volume of publications involving ceria and/or zirconia in oxidation reactions.

Hexaluminates

Substituted hexaluminates are a relatively new class of compound, and have been applied to combustion reactions[176-178]. The activity of these materials and their analogues gallanates, are usually lower than supported noble metal catalysts, with ignition temperatures ca. 100-200C higher than simple or mixed metal oxides. The interest in these materials arises from their thermal stability i.e resistance to sintering, particularly at high temperatures. This enables their potential use for high temperature combustion processes where, as previously stated, mass transport effects limit the rate of the reaction and the preservation of surface area becomes critical in maintaining the reaction rate. Substituted hexaluminates are porous layered anisotropic structures where cations e.g Ba, Co, La, Sr substitute for aluminium ions. Their resistance to sintering is by suppressing crystal growth along the c-axis[179]. Among many of the hexaluminates, those substituted with Ba, Mn and or Sr, using xerogel preparation methods have shown to be the most thermally stable and active materials up to temperatures as high as 1400C. Novel preparation methods using aerogel techniques have increased their thermal stability and surface areas of ca. $10m^2/g$ at 1300C may now be achieved[179]. Hence the use and interest in substituted hexaluminates for combustion reactions is for high temperature operations or as catalyst supports, since the activity of these materials at low temperatures are significantly less than other materials investigated.

Perovskites

Perovskite based materials are of the general structural formula ABO_3, and have received considerable attention as oxidation catalysts[166,180]. Perovskites, as well as

being studied for selective oxidation reactions[181], have also been studied for the combustion of carbon monoxide and light hydrocarbons[182]. However their application for the combustion of methane is limited[183]. The structure of perovskites is based on the named material $CaTiO_3$, where A and B cations are both available for substitution. Cation A is large in comparison to cation B and is situated at the corners of the ccp structure while the smaller cation is situated at the centre of the octahedral hole[180]. Seiyama et al studied a number of perovskite materials based on La- and Sr- for propylene oxidation[182]. They found several interesting features. Firstly the catalytic activity of the unsubstituted perovskites were related to the B cation component oxide and the most active materials were those based on Mn or Co i.e $LaMnO_3$ and $LaCoO_3$. Similar investigations for methane combustion observed the formation of partial oxidation products, particularly carbon monoxide. Seiyama et al presented data for a range of cation B substituted perovskites for methane combustion. It is shown that the temperature for 50% methane conversion ($T_{50\%}$) compared favourably to that of $Pt/\gamma\text{-}Al_2O_3$ even though this material had a much higher surface area. Calculated activation energies for the reaction were in the range 75-117 kJ/mol, indicating similar reaction mechanisms over both perovskite and platinum supported materials. However, simultaneous substitution of A and B cations had both a negative and positive effect on the catalytic activity. The substitution of cations A and B are believed to create lattice defects, which have been attributed to a strong increase in the ability of substituted perovskites to adsorb oxygen[182]. Seiyama and co-workers observed from their temperature programmed desorption studies on Sr substituted $LaCoO_3$ two characteristic desorption peaks. The first peak appeared broad at ca 800C while the second peak appeared sharper at ca. 820C. The two peaks were assigned to two different types of oxygen species. The first peak was attributed to weakly chemisorbed oxygen, bound to the metal cations, and was highly reactive for complete oxidation. The second peak was related to lattice oxygen responsible for selective oxidation.

Kinetic studies by Wise et al produced the following rate expression for methane combustion[166].

$$\text{Rate}=K_1P_{\text{methane}} + K_2P_{\text{oxygen}}{}^{0\text{--}0.5}\,P_{\text{methane}}$$

K_1= Rate constant for the reaction with surface oxygen

K_2= Rate constant for reaction with chemisorbed oxygen

The above expression relates the rate of reaction to both sources of oxygen. The authors further proposed the existence of anion vacancies produced by cation substitution, which affected the amount of oxygen adsorbed/desorbed from each type of perovskite.

In general the most active type of perovskite materials, which display good activity for combustion and are thermally stable are based on lanthanum and strontium oxides where the B cation is manganese, cobalt or iron oxides.

5.2: Summary

In summary it is evident that under low temperature conditions supported noble metal catalysts show a much higher activity than other materials. However novel mixed oxide materials based on ceria and zirconia, highly active for hydrocarbon transformations may display high activity for complete combustion. The use of superacidic materials for combustion reactions is limited. Hua et al compared the activity of platinum sulfated zirconia (PtSZr) with a number of trinary sulfated zirconias, i.e sulfated zirconia doped with Fe-Bi, Fe-Mn, Cr- and Fe-V and platinum gamma alumina (PtAl) for pentane oxidation[184]. The authors found PtSZr to be the most active sample. The addition of chromia, the most active ternary sample, to platinum sulfated zirconia led to a decrease in activity. However this material was still more active than the supported platinum sample. The authors concluded that both strong acidity and metal dispersion plays a role in determining the activity of the materials. In this respect it would be of interest to apply "superacidic" sulfated and molybdated zirconia materials to the complete oxidation of methane. As discussed previously in Chapter 1, liquid superacids are able to activate hydrocarbons, which are weak bases, to form carbocation intermediates. Indeed methane is the weakest base in the hydrocarbon series and therefore the most difficult to activate. Carboaction species were also found adsorbed onto the surface of the ternary sulfated zirconia materials, examined by Hua et al, discussed above, at the same time oxygen was dissociatively adsorbed[184]. To date no previous studies on molybdated "superacids" for methane combustion have been reported in the literature. However both Lin et al and Rezgui et al reported that sulfated iron manganese zirconia catalyst is effective for the conversion of methane to ethane in

the absence of oxidant[61,185]. Murata et al observed that lithium doped sulfated zirconia is an effective catalyst for the oxidative coupling of methane at 800C[100]. To this end it is of interest to study the behaviour of molybdated and sulfated materials for methane combustion which to date have not been applied to this reaction. Particularly as the results from Chapters three and four show the high selectivity of these materials to carbon dioxide under high pressure conditions. The addition of noble metals particularly platinum, may be considered to enhance the activity of the superacidic materials in view of their ability in hydrocarbon combustion reactions.

5.3:Results and Discussion

5.3.1: Reactor Studies

Molybdate doped zirconia materials

Table 1, shows the reaction data for a range of doped and undoped zirconia and ceria materials, screened for the complete oxidation of methane in the temperature range of 600-800C. In all cases the major product formed was carbon dioxide. Only in the case of the 10 wt% MoO_3/ZrO_2 sample was carbon monoxide observed, (as evidence of incomplete combustion). The molybdenum oxide based zirconia samples have been discussed in Chapter 4. As previously observed the 5wt% sample was the most active. In this study carbon dioxide was observed at temperatures ca 650C for the 5wt% MoO_3/ZrO_2 and above while for the 2 and 10wt% samples, activity was only observed at the higher temperatures at ca 700 and ca.800C respectively. However carbon dioxide was only observed at 700C over the 2wt% sample before the activity rapidly decreased. The rapid decrease in activity is followed by a large decrease in the carbon balance ca. 86%. Therefore it may be assumed that the rapid reduction in measurable activity maybe due to the formation of a carbonaceous material inhibiting the reaction. Further post reactor Raman spectroscopy on this sample showed bands associated with fluorescence, which may be due to some kind of aromatic carbon species. It is known that methane may aromatise forming benzene under both oxidative and non-oxidative conditions[95,186]. In comparison, the observed decrease in the carbon balance for the 2wt% sample was not observed for the 5 or 10wt% materials. A volcano type activity diagram can be envisaged where the 5wt% material represents the optimum composition for maximum catalytic activity. To evaluate the activity of the individual components of the molybdated zirconia system, bulk molybdenum trioxide and undoped zirconia were also tested for methane combustion activity. The molybdenum trioxide sample showed activity only at the highest temperature of 800C while the undoped zirconia sample, not given in Table 1 displayed no activity over the entire temperature range. Since the activity of all three of the molybdate doped materials were greater than their individual components a synergistic effect between the molybdate and the zirconia support can be inferred.

Table 1: Methane combustion data for molybdenum doped zirconia materials

Sample	Temperature (C)	Conversion[a] (%)		Selectivity[b] (%)		Carbon Mass Balance[c] (%)	Oxgen Demand[d] (%)
		CH_4	O_2	CO	CO_2		
2 wt% MoO_3/ZrO_2	600	-	-	-	-	96	100
	650	-	-	-	-	100	101
	700	1.0	0.2	-	100	100	101
	750	-	-	-	-	86	96
	800	-	-	-	-	87	95
5 wt% MoO_3/ZrO_2	600	-	-	-	-	106	105
	650	6.3	0.4	-	100	95	104
	700	7.6	0.8	-	100	96	104
	750	8.4	1.3	-	100	97	104
	800	7.4	1.0	-	100	97	100
10 wt% MoO_3/ZrO_2	600	-	-	-	-	96	103
	650	-	-	-	-	95	103
	700	-	-	-	-	95	104
	750	-	-	-	-	100	102
	800	1.2	0.7	29	71	103	103

[a,b,c,d] For definition see appendix 1.

Sulfated materials

Table 3 shows the catalytic data for sulfated zirconia and sulfated zirconia doped with iron and manganese oxides, denoted SO_4^{2-}/ZrO_2 and $Fe/Mn/SO_4^{2-}/ZrO_2$ respectively. Pure zirconia is completely inactive over the entire temperature range examined (500-800C). The addition of sulfate, has a similar promotional effect as the addition of molybdate. The activity of sulfated zirconia is increased and carbon dioxide is the only product observed from 750C onwards. However the promotional effect is more comparable with the 10wt% molybdenum doped zirconia sample than the 5wt% sample. The addition of iron and manganese oxides to sulfated zirconia is reported to strongly increase the acid strength[61]. Indeed $Fe/Mn/SO_4^{2-}/ZrO_2$ is reported to be the strongest solid superacid developed to date[61]. The results in Table 3, for this sample indicates a promotional effect over pure zirconia, with carbon dioxide formed at 800C. However, the activity of sulfated zirconia appears higher than its iron and manganese doped counterpart. Similar observations were made by

Hsu et al in their studies on ternary oxides doped onto sulfated zirconia for pentane oxidation[184].

Table 2: Methane combustion data for sulfated zirconia materials

Sample	Temperature (C)	Conversion[a] (%)		Selectivity[b] (%)		Carbon Mass Balance[c] (%)	Oxygen Demand[d] (%)
		CH_4	O_2	CO	CO_2		
SO_4^{2-}/ZrO_2	600	-	-	-	-	104	103
	650	-	-	-	-	100	105
	700	-	-	-	-	100	100
	750	1.7	0.5	-	100	98	100
	800	1.9	2.7	-	100	101	98
$Fe/Mn/SO_4^{2-}/ZrO_2$	600	-		-	-	99	102
	650	-	-	-	-	99	99
	700	-	-	-	-	100	98
	750	-	-	-	-	99	97
	800	0.9	0.2	-	100	100	102

[a,b,c,d] For definition see appendix 1

The authors found that platinum doped sulfated zirconia was the best sample, while incorporation of the transition metal oxides decreased the combustion activity. This is an interesting observation since the results given in this chapter indicate that both sulfated zirconia and iron oxide are active for methane combustion. Similarly manganese oxide has also been studied for methane oxidation[184]. Therefore the combination of iron and manganese oxides with sulfated zirconia in the form of $Fe/Mn/SO_4^{2-}/ZrO_2$ superacid appears relatively less active than their individual oxides. Hence, it appears that in the case of methane combustion, investigated under the conditions employed in this study, there is no synergistic effect between sulfated zirconia and iron and manganese oxides. Further these results may also imply that $Fe/Mn/SO_4^{2-}/ZrO_2$ is a weaker solid acid than sulfated zirconia if acidity plays a role in activating methane. The activity of sulfated zirconia is reduced by the incorporation of iron and manganese oxides possibly by interacting with the sulfate group and reducing the inductive effect, believed to be responsible for strong acidity as previously discussed in Chapter 1. However, $Fe/Mn/SO_4^{2-}/ZrO_2$ has been shown to be active for n-butane isomerisation[31].

Ceria/zirconia and zirconia/ceria doped materials

As described previously, Trovarelli et al reported the flourite type structure based on CeO_2/ZrO_2 solid solutions, to be highly active for methane combustion[168]. Analogous samples of 10wt% CeO_2/ZrO_2 and 10wt% ZrO_2/CeO_2 were prepared and examined for methane combustion activity as direct comparisons to the molybdenum supported zirconia samples described previously. It is evident from Table 3, that both samples are active for the combustion of methane with the exclusive formation of carbon dioxide at 750-800C. However it is observed that the 10wt% CeO_2/ZrO_2 sample displays a higher methane conversion than the 10wt% ZrO_2/CeO_2 sample. The differences in methane conversions are not a function of surface area, since both samples have similar specific surface areas of ca. 27 m^2/g. Therefore the differences in activity must be due to an intrinsic increase in activity which may be related to the structural nature of the ceria doped zirconia sample. The use of ceria as a dopant in many catalytic material formulations is well documented and has been widely applied to selective and complete oxidation reactions. The general properties of ceria and hence the reasons why ceria has been extensively employed in oxidation reactions was previously summarised.

Therefore it may be deduced that the adsorption of methane takes place on ceria sites and this facilitates the oxidation of the hydrocarbon. In the case of zirconia doped on ceria the incorporation of zirconia may block active sites on the ceria surface thus retarding the combustion reaction. It would have been of interest in this instance to assess the activity of the undoped cerium oxide. It is apparent from Table 1, that the activity of the zirconia doped ceria sample is closely related to the temperature of calcination. The zirconia doped ceria sample calcined at 923C, in agreement with the calcination temperature used in the study by Trovarelli et al, showed activity only at 800C. The formation of carbon dioxide, the only product observed was accompanied by much lower methane and oxygen conversion than the zirconia doped ceria sample calcined at 800C. Ceria/zirconia materials are often termed solid solutions. Therefore the difference in activity between these samples may be as a result of a different surface zirconia, which may diffuse to the surface of this solid solution under increased calcination temperature.

However it may also be possible that a phase change was induced by the calcination of this sample at higher temperatures, section 5.4.3. In comparison with the

molybdate doped materials it is observed that all the ceria/zirconia samples tested for the complete combustion of methane were active.

Table 3: Methane combustion data for ceria/zirconia zirconia/ceria doped samples

Sample	Temperature (C)	Conversion[a] (%)		Selectivity[b] (%)		Carbon Mass Balance[c] (%)	Oxygen Demand[d] (%)
		CH_4	O_2	CO	CO_2		
10 wt% CeO_2/ZrO_2	600	-	-	-	-	93	102
	650	-	-	-	-	91	102
	700	-	-	-	-	102	104
	750	4.2	0.4	-	100	98	105
	800	4.1	0.5	-	100	98	97
10 wt% ZrO_2/CeO_2	600	-	-	-	-	94	97
	650	-	-	-	-	96	96
	700	-	-	-	-	97	96
	750	1.6	0.3	-	100	98	96
	800	1.7	0.3	-	100	99	96
10 wt% ZrO_2/CeO_2*	600	-	-	-	-	99	99
	650	-	-	-	-	101	100
	700	-	-	-	-	102	99
	750	-	-	-	-	93	98
	800	0.7	0.1	-	100	92	97

*Calcined at 923C. [a,b,c,d] For definition see appendix 1.

As previously stated in Chapter 4, the addition of dopants to zirconia enhances the stability of the tetragonal phase. Further from the pre- reactor characterisation of the molybdated materials, discussed in Chapter 4 it was observed that activity of these materials was related to the degree of molybdenum surface coverage. The 5wt% sample forming a complete molybdate monolayer and displaying maximum activity. In the case of ceria/zirconia materials it may be tentatively proposed that the incorporation of a metal oxide dopant to zirconia, in order to achieve optimal activity, may be more related to the tetragonal/monoclinic ratio and not to monolayer formation. In comparison with the zirconia doped ceria sample it was generally observed that the doped zirconia samples out performed the doped ceria samples.

Simple oxide materials

To compare the activity of the doped zirconia and ceria materials, simple oxides suitable for methane combustion were tested as well as molybdenum (VI) oxide as a background. Table 4, shows the activity data for iron (III) and copper (II) oxides as well as molybdenum (VI) oxide.

Table 4: Methane combustion data for some simple oxides

Sample	Temperature (C)	Conversion[a] (%)		Selectivity[b] (%)		Carbon Mass Balance[c] (%)	Oxygen Demand[d] (%)
		CH_4	O_2	CO	CO_2		
Fe_2O_3	600	-	-	-	-	97	98
	650	0.9	0.2	-	100	95	99
	700	1.0	0.2	-	100	94	100
	750	1.1	0.2	-	100	100	97
	800	4.7	0.2	-	100	96	98
CuO	600	-		-	-	-	-
	650	0.9	0.2	-	100	108	98
	700	1.0	0.2	-	100	99	97
	750*	-	-	-	-	97	99
	800	1.5	0.3	-	100	94	96
MoO_3	600	-	-	-	-	99	101
	650	-	-	-	-	97	100
	700	-		-	-	98	97
	750	-	-	-	-	98	96
	800	0.8	0.2	-	100	94	96

[a,b,c,d] For definition see appendix 1.

As expected both the copper and iron oxides showed activity for the low temperature combustion of methane at temperatures in the range 650-800C, with the exclusive formation of carbon dioxide. It was observed that both methane and oxygen conversions for the iron and copper oxide samples were similar until 800C where the iron oxide material shows a fourfold increase in methane conversion. Therefore it appears that iron oxide is more active than copper oxide at temperatures above ca. 750C. Indeed the surface areas for these metal two metal oxides are similar, indicating that the differences in activity observed in Table 4 are not a function of differences in surface area. In comparison to the molybdenum trioxide sample it is

evident that both the copper and iron oxide samples showed a higher activity. Indeed the activity of the molybdenum trioxide sample is also much lower than the molybdated samples discussed previously. This further adds to the argument of a synergistic effect between the zirconia support and the molybdate dopant.

In comparison with the activities of the materials described above i.e ceria/zirconia and molybdated zirconia materials, both the iron and copper oxides show an increased activity. Only the 5wt% molybdated sample is comparable in activity to the simple oxides of copper and iron with combustion products being observed from 650C onwards.

This also reiterates the discussions presented in Chapter 4 on the uniqueness of the 5wt% molybdated zirconia sample. However a noticeable feature of this sample was the decrease in methane and oxygen conversion on passing from 750C to 800C, which did not occur with either the ceria/zirconia samples or the iron and copper oxide samples.

Platinum doped materials

As indicated in the introduction to this chapter the addition of noble metals particularly platinum and palladium promotes the low temperature combustion of hydrocarbons[154,156,157]. As previously stated, platinum doped sulfated zirconia has been employed in hydrocarbon activation studies and shown an enhancement in both catalytic activity and increased the thermal stability over non-platinum doped sulfated zirconia for pentane isomerisation[184]. Indeed the use of platinum on sulfated zirconia stems from the fact that this material is observed to deactivate rapidly. Deactivation has been proposed to be due to sulfate decomposition or coking, which is believed to block active sites, and is discussed further in Chapter 1 section 1.3.4. Table 5, shows platinum doped samples. It was observed that doping both iron and zirconia oxides with 0.5 wt% platinum increases the activity of these materials with activity observed over ca 600-800C temperature range with the exclusive formation of carbon dioxide. However it is observed that the methane conversion of the platinum doped zirconia is higher than that of the platinum doped iron oxide in the temperature range 650-800C. Once again an anomalous decrease in methane conversion at 750C is evident, while both the oxygen and carbon balances are ca

100%. However the oxygen conversion for the platinum iron oxide sample is higher over the entire temperature range.

The addition of platinum, to both sulfated zirconia and to the 5wt% molybdated zirconia samples, was observed to decrease both the methane and oxygen conversions compared to the non-platinum doped samples. However, the onset of activity for the 0.5wt% Pt/5wt% MoO_3/ZrO_2 sample occurs at 50C lower than the non-platinum doped material at 600C. Therefore it may be implied that the addition of platinum to molybdated and sulfated "superacidic" zirconia materials decreases their activity.

Table 5: Methane combustion data for platinum doped materials

0.5wt% Platinum Doped Sample	Temperature (C)	Conversion[a] (%)		Selectivity[b] (%)		Carbon Mass Balance[c] (%)	Oxygen Demand[d] (%)
		CH_4	O_2	CO	CO_2		
ZrO2	600	-	-	-	-	101	100
	650	3.8	0.2	-	100	97	100
	700	5.3	0.4	-	100	97	100
	750	3.0	0.5	-	100	100	100
	800	11.1	0.7	-	100	93	98
Fe_2O_3	600	2.6	0.5	-	100	101	99
	650	3.7	0.7	-	100	102	99
	700	4.2	0.8	-	100	99	100
	750	4.8	0.9	-	100	103	99
	800	5.1	1.0	-	100	102	98
5wt% MoO_3/ZrO_2	600	1.4	0.2	-	100	101	101
	650	1.6	0.3	-	100	97	101
	700	2.0	0.4	-	100	96	100
	750	2.1	0.4	-	100	99	99
	800	3.4	0.6	-	100	101	104
SO_4^{2-}/ZrO_2	600	-	-	-	100	97	100
	650	-	-	-	100	100	100
	700	-	-	-	100	100	99
	750	-	-	-	100	103	107
	800	0.9	0.2	-	100	101	100

[a,b,c,d] For definition see appendix

This maybe due to platinum inhibiting sites active for methane combustion or by inhibiting the interaction between the zirconia support and the molybdate or sulfate, reducing the effect of the synergistic interactions.

Specific Activity

Figures 3 and 4, shows mass and surface area normalised activity data for a range of materials for the low temperature combustion of methane at 800C. Evident from the Figure 3 is the superior performance of the simple oxides, iron and copper, which show specific activities at least three times higher than the other samples tested. This further confirms the interest in simple metal oxides, which due to their facile redox

*See text below

Figure 3: Surface normalised activity data for the combustion of methane at 800C

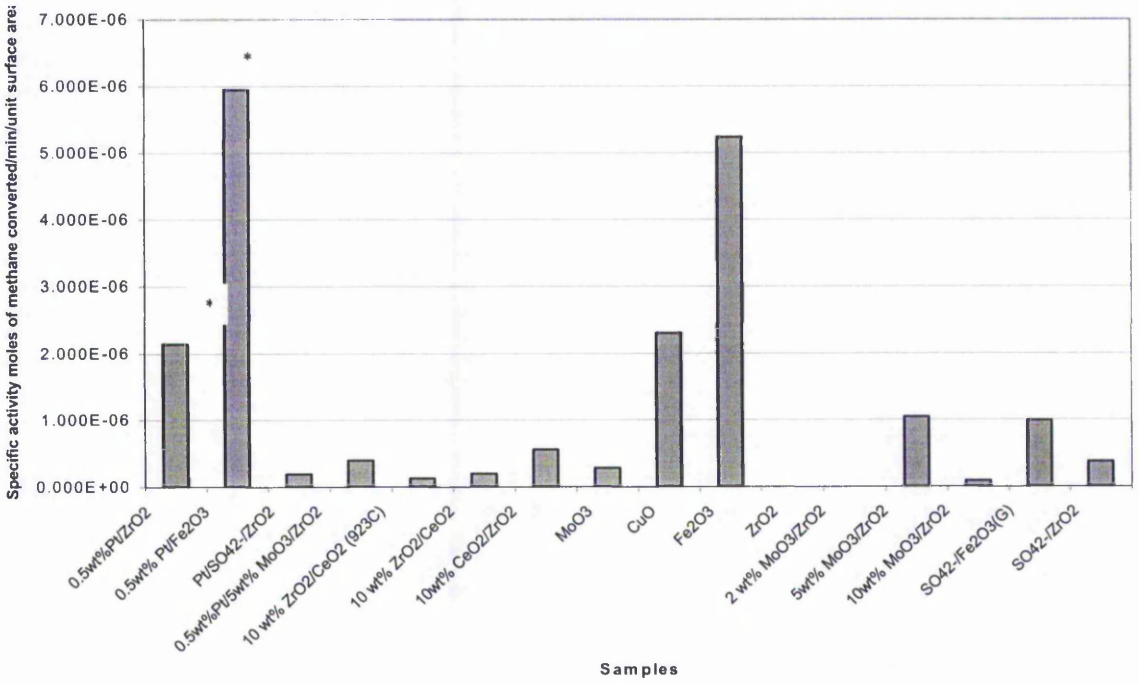

properties, are studied for oxidation reactions. However the activity of bulk molybdenum trioxide and zirconium oxide materials displayed significantly lower activity compared to the iron and copper oxides.

Indeed zirconium oxide displayed no measurable activity over the entire temperature range investigated for this reaction. Considering the specific activity of the molybdated zirconia samples, it is observed from Figures 3 and 4, that the activity of the 5wt% sample is greater than both the bulk molybdenum and the zirconium oxide materials. Since the specific activity of this material is greater than both the bulk molybdate and the base zirconia, a synergistic effect between the molybdate and the zirconia can be inferred. However this possibly suggests a synergism between molybdenum and zirconia which is dependent upon molybdate loading or the surface coverage, since the specific activity of the 10 and 2wt% samples are similar to the bulk molybdenum and zirconium oxide materials. Indeed the 2wt% molybdated zirconia sample showed no measurable activity at 800C, and from this point appears to be comparable to the base zirconia.

Figure 4: Mass Normalised Methane Combustion Data for a Range of Samples

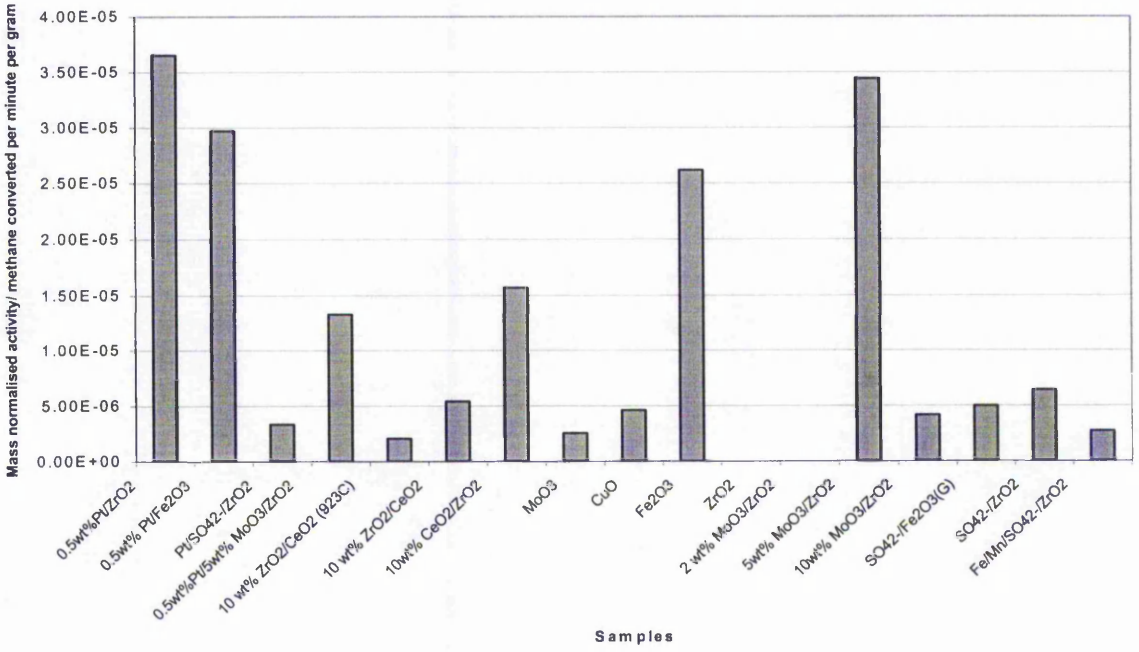

However observed from Table 1, is that this sample does indeed display activity at 700C while at higher temperatures the carbon balance and oxygen demands are well below 100% and no measurable reaction products are observed. This may indicate

that this material is more active than both the base zirconia and bulk molybdate at 700C, implying a synergistic effect, and that by increasing the reaction temperature beyond 700C a carbonaceous material is deposited on the surface.

The carbonaceous material so formed appears to inhibit any increase in catalytic activity for this sample, probably by blocking sites active for oxidation. Evidence for a carbonaceous material on the surface of the 2wt% molybdate sample comes from Raman spectroscopy investigations, performed by Dr.S.H Taylor at the University of Cardiff. However in proposing a synergistic effect between the molybdate and the base zirconia it must be appreciated that the phase of the base zirconia may not be the same as the doped zirconia material. Pure zirconia, is expected to show a 100% monoclinic phase, whereas for doped zirconia a metastable tetragonal phase is often encountered. X-ray diffraction patterns of the 2,5 and 10wt% molybdated samples were given in the previous chapter and confirm the decrease in monoclinic phase and an increase in the metastable tetragonal phase with increasing molybdate content. However, it is evident from Figures 3 and 4 that the activity of the 5wt% sample is the most active material tested with the exception of the simple oxides of iron and copper, which is as a direct result of the specific interaction between the molybdate and the zirconia support

Similarly the ceria doped zirconia sample shows specific activity greater than that of pure zirconia at 800C. However again it maybe expected that the phase of the pure zirconia is <100% of the monoclinic phase. From this point of view it would be of interest to test a pure ceria material for catalytic activity. In comparison with the zirconia/ceria, the specific activity for this sample is ca. 50% lower than the ceria/zirconia counterpart similarly prepared and calcined. Since the specific surface area of both the ceria/zirconia and zirconia/ceria are similar there appears to be an intrinsic difference in activity between the two samples, which maybe related to the differences in the surface composition of the solid solutions, so formed. The differences in specific activity between the two samples may also relate to the content and/or phase of the zirconia, since the samples with higher zirconia content (90%), show the highest specific activity at 800C. However pure zirconia itself shows no measurable activity at this temperature, which further implies that the differences in the calculated specific activities are as a consequence of the differences in surface composition. The effect of surface composition differences

between the two samples may further relate to the decreased number of sites active for the low temperature combustion of methane for the zirconia/ceria sample. From Figure 3, it is also evident that increasing the temperature of calcination of the zirconia/ceria sample from 800C to 923C decreases slightly the specific activity of this material. This is interesting since 923C is the temperature of activation used in the work by Trovarelli et al in their studies on methane combustion over zirconia/ceria materials[168]. However the increase in calcination temperature may produce a change in the phase ratio of the monoclinic: tetragonal form of zirconia. The increase in the proportion of the monoclinic phase may bring about a change in the surface composition of the zirconia/ceria materials, which may ultimately reduce the number of active sites. Therefore it maybe tentatively proposed that the activity of these materials come directly from the phase of the zirconia or at least the phase of the zirconia with ceria at the surface.

The addition of platinum to a selection of the above materials is observed to have two general effects. Firstly doping the simple oxides with platinum increases their specific activities, particularly in the case of zirconia. Secondly, doping platinum on an already doped zirconia such as sulfated or molybdated zirconia decreases the specific activity of these materials. This may imply that doping a superacidic material with another dopant, e.g transition metal oxide or noble metal, may affect the acidity in some way, as to reduce the acid strength. However, Lambert et al observed a promotional effect of adding sulfur trioxide to platinum for propane oxidation[187]. Therefore it may be the sequence of addition of promoters, which affect the resultant activity of the material. It may be envisaged that the addition of dopants to sulfated zirconia for example may create a sandwich effect where the sulfate is interacting with both the support, i.e. zirconia and the dopant e.g iron and manganese oxides. This would therefore imply that one must first add the dopants to the support before sulfating, thereby leaving the sulfate bound to only one surface and the retention of symmetry which implies its inductive nature, which gives rise to the strong acidity, should remain. The enhanced activity of the platinum doped metal oxides i.e zirconium and iron oxides shown in Figure 3 is related solely to the incorporation of platinum. As such it is acknowledged that the activity observed for these materials should be normalised to platinum content or to platinum dispersion, determined by hydrogen chemisorption. Further the inclusion of the platinum doped

metal oxides in Figure 3, serves as a useful comparison with the other materials investigated for this reaction, particularly since the methane and oxygen conversions were low <5%.

5.3.2: X-Ray diffraction studies

X-ray diffraction (XRD) patterns have been compared on the basis of the support material.

Zirconia supported oxides

Pre-reactor x-ray diffraction patterns of the molybdated zirconia samples were presented and discussed in the previous chapter. In summary it was found that the addition of molybdate stabilised the metastable tetragonal phase of the zirconia, and the content of which was found to depend on the molybdate loading. The 5wt% sample followed this trend of increasing the content of the tetragonal phase. Therefore the activity differences observed for the molybdated samples not due to any unique features.

The x-ray diffraction pattern of pure zirconia shows the phase to be that of monoclinic zirconia JCPDS (37-1484), as expected, Figure 5. As shown in Figure 3 and 4, the specific activity for this sample was negligible, therefore it is evident that pure zirconia in the monoclinic phase is inactive for this reaction. However Figure 5 shows XRD patters of ceria/zirconia and iron/manganese/sulfated zirconia, which were observed to stabilise the metastable tetragonal phase of zirconia. The addition of dopants is known to stabilise the metastable phase of zirconia, and this coincides with the observed increase in specific activity for these doped zirconia samples over pure monoclinic zirconia. The addition of ceria to zirconia stabilises completely the metastable tetragonal phase, which coincides with the highest activity shown for any sample in this group, and is only inferior in specific activity to that of the simple oxides and to the 5wt% MoO_3/ZrO_2 sample. It is interesting to compare this sample with the zirconia/ceria samples discussed above. The ceria/zirconia sample shows a higher specific activity and a higher degree of crystallinity than the zirconia/ceria counterparts.

Figure 5: Powder x-ray diffraction patterns of zirconia supported materials

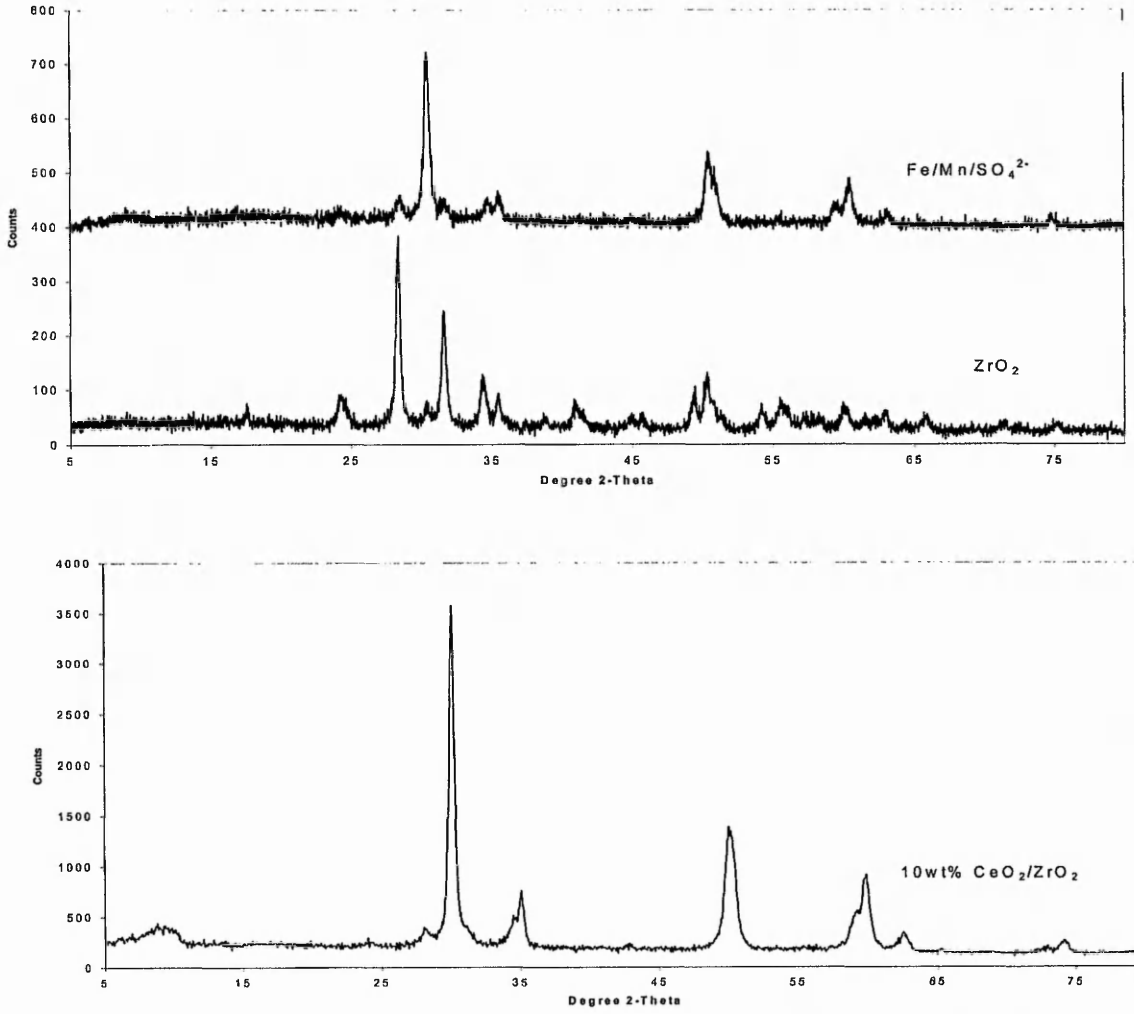

This may then imply that the degree of crystallinity as well as the phase of the zirconia may be important for this reaction. However the $Fe/Mn/SO_4^{2-}/ZrO_2$ sample also shows approximately 100% metastable zirconia phase as well as a degree of amorphous content shown by the high background of the diffraction pattern, with prominent reflections associated with those of iron and manganese oxide.

The specific activity for this sample was observed to be much lower than the other doped zirconia samples. Therefore it is evident that the presence of the metastable phase of zirconia alone is insufficient to explain the differences in activity between the samples however differences in crystallinity may be important.

Ceria supported materials

Figure 6 shows XRD patterns of zirconia/ceria samples calcined at 800 and 923C. It is observed that the sample calcined at 923C is more crystalline i.e the line widths are narrower and their intensities are approximately twice that of the sample calcined at 800C. However both samples contain a degree of amorphous content.

The pattern for the 800C sample also contains some extra reflections at ca. 37 and 45 2θ, which cannot be related to the ceria but may be related to the monoclinic phase of zirconia (JCPDS 37-1484). Hence the observed differences in activity between these two samples may relate to the presence of monoclinic zirconia, present in the 800C sample, due the effects of temperature allowing a greater degree of diffusion of the monoclinic phase zirconia into bulk the ceria at the higher temperature of 923C. This implies that it is the presence of this monoclinic phase, which produces the observed activity, or at least it is a combination of the monoclinic zirconia phase with the cubic ceria phase producing the enhanced activity, since pure zirconia calcined at 800C showing a monoclinic phase, appears inactive. However, the greater degree of amorphous material in the 800C sample may also relate to the observed increase in activity for this sample.

Figure 6: X-ray diffraction patterns of pre-reactor ZrO_2/CeO_2 materials for methane combustion

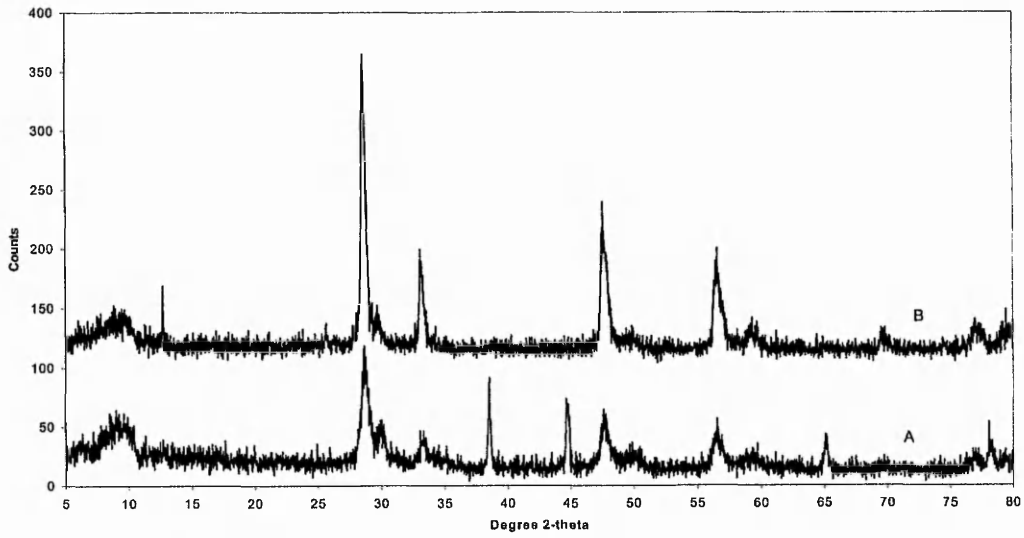

A sample calcined at 800C, B sample calcined at 923C

Simple oxide materials

From Figures 4 and 5, it is observed that the simple oxides, with the exception of molybdenum oxide, display the highest specific activities for methane combustion. Figure 7 shows the XRD patterns of copper and molybdenum oxides. These samples are observed to be much more crystalline i.e. narrow line widths and high intensity, than any of the other samples tested for methane combustion. However, since molybdenum oxide shows a higher degree of crystallinity but a significantly lower specific activity at 800C, much lower than that of either the copper or iron oxides, and indeed a similar value to that of ceria/zirconia (800C), crystallinity alone cannot account for the observed differences in catalytic activity. However the copper oxide sample shows a degree of amorphous content, which may imply that the amorphous content of samples investigated for methane combustion maybe significant in terms of catalytic activity.

Figure 7: X-ray diffraction patterns for pre-reactor copper and molybdenum oxides for the combustion of methane

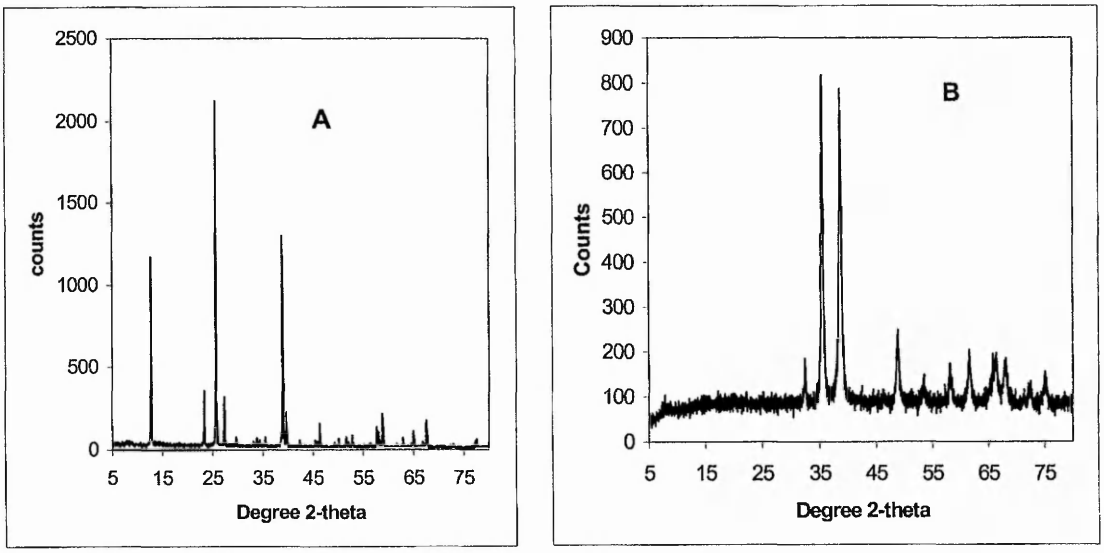

A= MoO_3 and B= CuO

However the copper oxide sample shows a degree of amorphous content, which may imply that the amorphous content of samples investigated for methane combustion maybe significant in terms of catalytic activity. Due to the problems associated with

fluorescence with the copper K_α source, the iron oxide samples derived from goethite were unable to be characterised by x-ray diffraction. However on the basis of previous experimental work it may be expected that the iron oxide x-ray diffraction pattern to be that of a crystalline α-Fe_2O_3 .

Platinum doped materials

The addition of platinum to pure zirconia was shown in Tables 3 and 4 to increase significantly the specific activity of this sample at 800C. Similar observations with Pt/Fe_2O_3 were also observed but the increase in activity was not so marked. X-ray diffraction of Pt/ZrO_2 shown in Figure 8 shows only reflections belonging to monoclinic zirconia and no reflections of platinum were observed. However the addition of platinum to zirconia was observed to increase the background of the XRD pattern, indicating the significant presence of an amorphous phase. This may explain the enhanced activity due to the formation of highly dispersed platinum metal particles over the zirconia support.

Figure 8: X-ray diffraction patterns of pre-reactor platinum doped samples for the combustion of methane

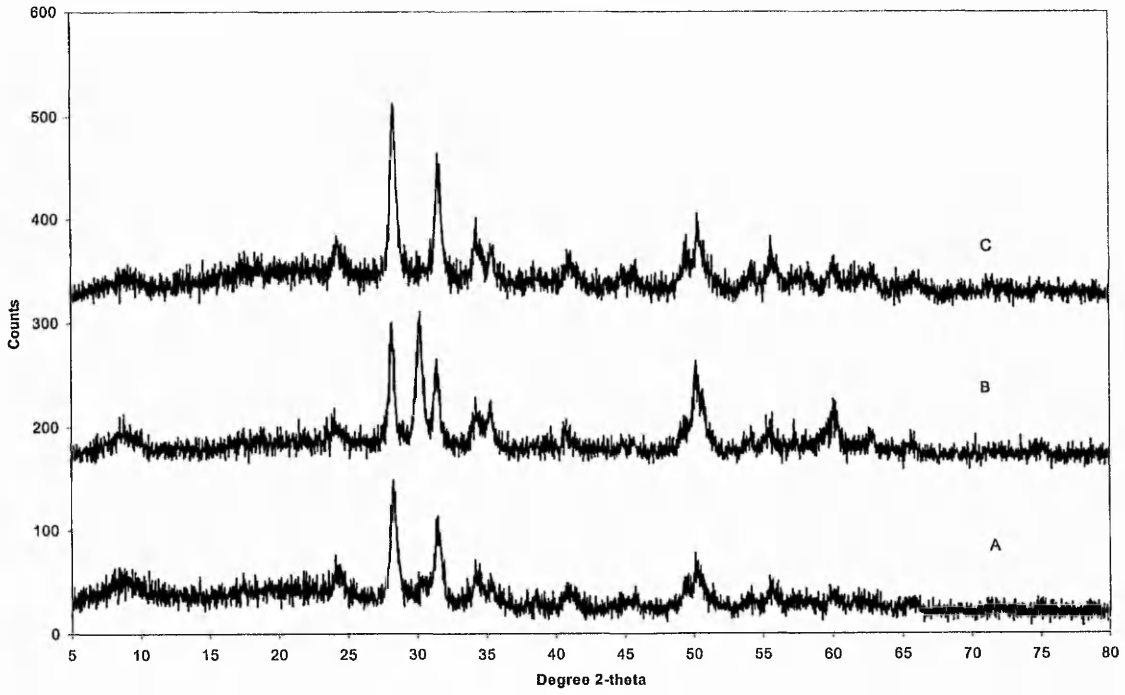

(A) Pt/ZrO_2, (B) 0.5wt%Pt5wt%MoO_3/ZrO_2 and (C) 0.5wt%Pt SO_4^{2-}/ZrO_2

Therefore, it appears that monoclinic zirconia is a suitable support for platinum metal for the low temperature combustion of methane.An interesting observation is that the addition of platinum to both the 5wt% MoO_3/ZrO_2 and to the SO_4^{2-}/ZrO_2, was observed from Table 5, to inhibit the low temperature combustion of methane by approximately 50%. This inhibitory effect may be a general phenomenon of "superacids" when impregnated with platinum under the procedure outlined in chapter two, and may not be specifically related to the presence of sulfate or molybdenum oxide. Figure 8 shows the XRD pattern of Pt/5wt% MoO_3/ZrO_2 material, and is shown to be similar to that of non-platinum doped 5wt% MoO_3/ZrO_2. However a prominent reflection at ca. 30.5° 2θ indicates the presence of a meta-stable tetragonal zirconia phase occurring in the pre-reactor sample. It is clear that this reflection is not associated with platinum. After calcination of the 5wt% MoO_3/ZrO_2 at 800C for 12 hours in static air, the material contained only 13% of the meta-stable tetragonal phase, as calculated using the Toraya's method, this is in comparison to a 31% meta-stable tetragonal phase content when impregnated with platinum. It is known that the transition of the meta-stable tetragonal phase to the more thermodynamically stable monoclinic phase occurs to varying degrees at elevated temperatures depending on the dopent material. Therefore, it appears that the reduction of the platinum precursor to platinum metal effects the phase of the zirconia support promoting the formation of the meta-stable tetragonal phase. Further it is observed that this effect is related to the presence of molybdenum oxide since no phase change occurred for the non-molybdenum doped platinum zirconia material. Hence, the observed change in phase of the zirconia to an increased metastable tetragonal content is due to the interaction of molybdenum, with the platinum metal or precursor. This change in the phase during the reduction stage may cause encapsulation of the platinum metal particles, which may explain the reduction in the specific activity measured at 800C. However the observed reduction in activity may be due to the interaction of the platinum with the molybdenum oxide. This interaction may reduce the activity of sites active for methane combustion on both the support material and the metal.

5.4.2: Post reactor Analysis: X-Ray Diffraction

Zirconia supported materials

Figure 9 shows the CeO_2/ZrO_2 post reactor XRD pattern. It is evident that the zirconia is in the metastable tetragonal phase with a characteristic reflection at 30.5° 2θ. In comparison with the pre-reactor XRD pattern Figure 5, it is observed the degree of crystallinity is significantly reduced after the reaction, while the proportion of the metastable tetragonal phase remains the same ca. 30%.

This implies that under the reaction conditions the zirconia support forms smaller crystallites but maintains the proportion of metastable tetragonal: monoclinic phase.

Therefore it is evident that the thermal stability of CeO_2/ZrO_2 type materials depends both upon the content of ceria, or at least the ratio of ceria:zirconia and also calcination temperature. It may be suggested that a 10wt% ZrO_2/CeO_2 calcined at temperatures >900C offers suitable thermal stability at reaction temperatures ca. 800C and may be considered as a suitable support for low temperature combustion reactions. In this respect it is interesting to study the XRD pattern of the pure zirconia material before and after the reaction, Figure 5.

Figure 9: Powder x-ray diffraction pattern of ceria/zirconia sample

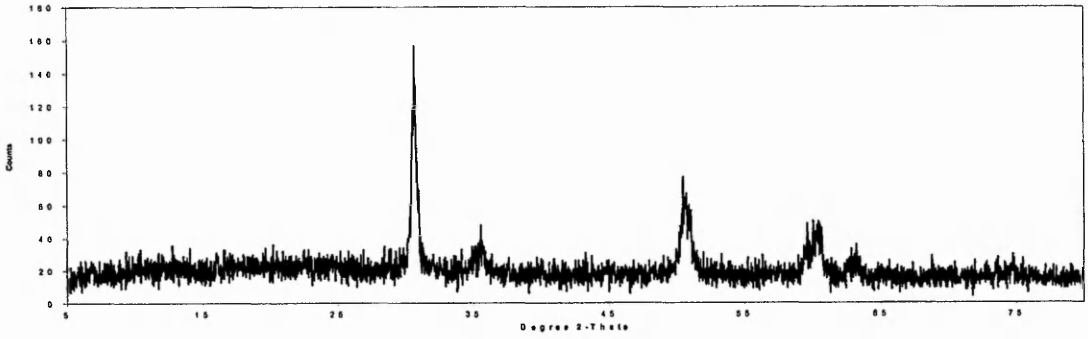

It is observed that monoclinic zirconia appears thermally i.e. little or no significant sintering and retention of phase, under the reaction conditions employed.

A qualitative representation is given below. The Figure demonstrates the effect of ceria content on the thermal stability of the materials investigated. As the thermal stability increases the activity of the material is found to decrease. Thermal stability as well as being a function of ceria content is also a function of calcination temperature. Indeed to imply thermal stability, of these materials, without measuring

surface areas after the reaction may be speculative, however since the XRD patterns relate to the particle size and therefore indication of surface area it may serve as a qualitative discussion.

Ceria supported materials

Figure 10 shows post reactor XRD patterns of ZrO_2/CeO_2 materials calcined at 800C and 923C respectively. In comparison, the XRD pattern of the material calcined at 923C is similar in phase to that of the same material calcined at 800C with a twofold increase in crystallinity of the latter material. Both patterns are associated with a large degree of amorphous material similar to that observed in the XRD patterns for their pre-reactor counterparts. However in further comparing the pre- and post XRD patterns it is observed that the phase of the ZrO_2/CeO_2 material calcined at 923C is unchanged after the reaction, while the sample calcined at 800C has three prominent reflections at 38.5°, 44.6° and 65.1° 2θ absent after the reaction. These missing reflections, were assigned previously to the monoclinic phase of zirconia the reflections being (120), (211) and (032) respectively. A possible explanation may be that the actual temperatures reached in the catalyst bed would be greater than the set temperature of 800C.

Figure 10: Powder x-ray diffraction patterns of zirconia/ceria samples

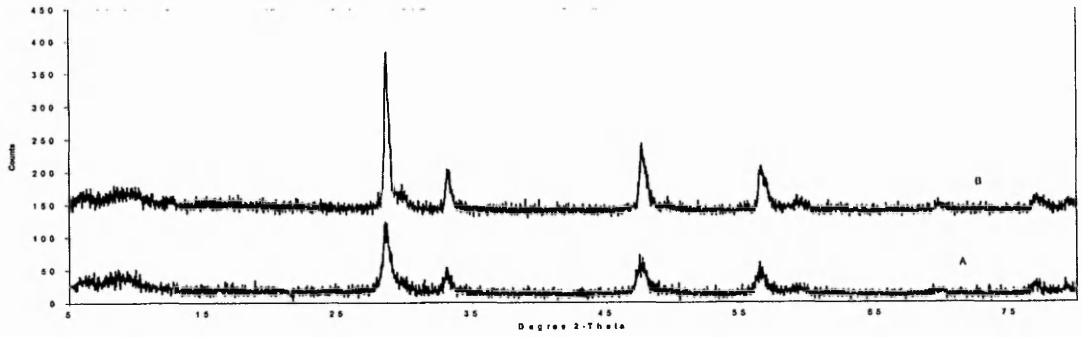

ZrO_2/CeO_2 (800C) and (B) ZrO_2/CeO_2 (923C)

These conditions may produce a more dispersed monoclinic phase in the bulk ceria material. Therefore the reflections relating to the monoclinic phase would not be observed in the post reactor XRD pattern.

Simple oxide materials

Figure 11 presents XRD patterns of the copper oxide and molybdenum (VI) oxide after exposure to the reaction environment. In comparison with their pre-reactor XRD patterns it is observed that the crystallinity for copper oxide is increased, whereas for the inactive molybdenum oxide sample crystallinity is severely decreased.

This may indicate that the molybdenum oxide structure collapses and forms smaller particles during the reaction, whereas copper oxide particles may aggregate to from larger particles, giving rise to an XRD pattern of higher intensity. The increased crystallinity is observed from the extra reflection at 36.5° 2θ.

However, the phases of both materials are unchanged after exposure to reaction conditions. The change in the MoO_3 pattern is consistent with the expected sublimation

Figure 11: Powder x-ray diffraction patterns of copper and molybdenum oxide

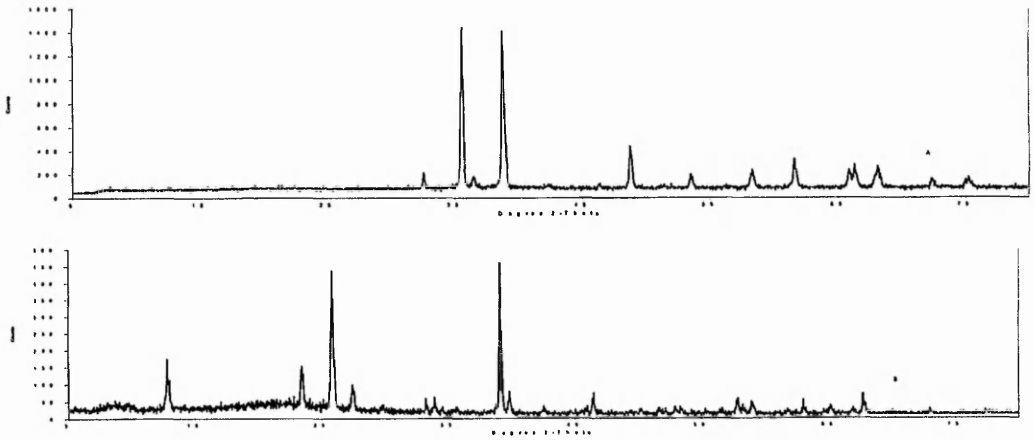

(A) CuO and (B) MoO_3

Platinum doped materials

Figure 12 shows the post reactor XRD patterns of platinum doped zirconia and 5wt% MoO_3/ZrO_2. In comparison with their pre-reactor XRD patterns, Figure 8, it is evident that there is only a slight difference between the pre and post reactor XRD patterns. The Pt/ZrO_2 material shows only a slight decrease in crystallinity and a large amorphous phase is still present. This indicates, possibly, that the degree of platinum metal dispersed is essentially the same after reaction as that before. Indeed no reflections pertaining to platinum were observed in the post reactor XRD pattern.

Figure 12: Powder x-ray diffraction pattern of platinum doped materials

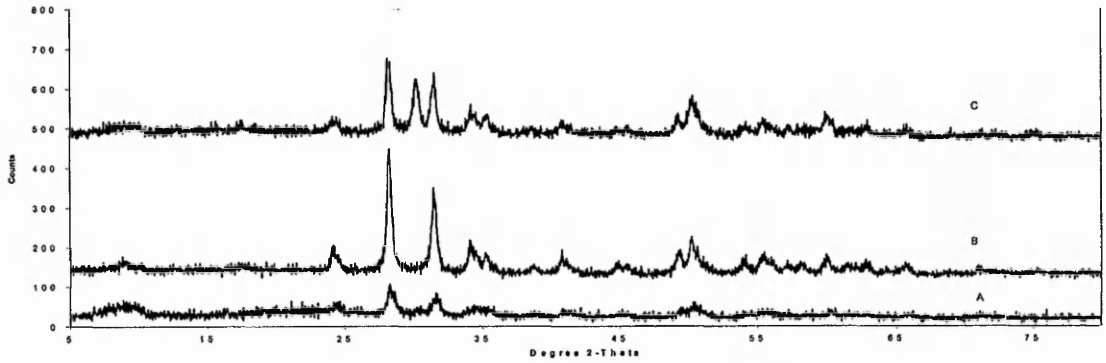

(A) 0.5wt% Pt/ZrO_2, (B) 0.5wt%Pt/ SO_4^{2-}/ZrO_2 and (C) 0.5wt% $Pt/5wt\%MoO_3/ZrO_2$

Similarly, the post-reactor XRD pattern of the 5wt% MoO_3/ZrO_2 material shows a slight decrease in crystallinity with a possible decrease of the tetragonal content from 31 to 30%, as calculated using Toraya's method. Therefore the volume fraction of the metastable tetragonal phase in this material is essentially constant before and after exposure to the reaction environment.

It may be proposed that the enhanced activity observed from doping zirconia with platinum originates from both the high dispersion of platinum metal and the thermal stability of the zirconia support. However for the 5wt% MoO_3/ZrO_2 material, the addition of platinum promotes the formation of the meta-stable tetragonal phase after the reduction of the platinum precursor, Figure 12. Once this mixed phase is formed this then becomes thermally stable after exposure to the reaction environment.

5.5: Conclusions

This brief study shows the potential use of 5wt% MoO_3/ZrO_2 as a low temperature combustion material. The specific activity of this material is third only to that of the expected simple copper and iron oxides and to the platinum doped zirconia sample. Surprisingly the activity of this material is much higher than that of the ceria/zirconia materials, which have attracted much attention in the literature for their use in oxidation reactions due to the oxygen storage ability of ceria. Unusually, the addition of platinum post calcination to the 5wt% MoO_3/ZrO_2 material facilitates the formation of the meta-stable tetragonal phase.

For the low temperature combustion of methane it may appear that superacidity is not a requirement since the strongest superacidic material $Fe/Mn/SO_4^{2-}/ZrO_2$ displayed lower activity than either SO_4^{2-}/ZrO_2 or the 5wt% MoO_3/ZrO_2 materials. However it must be noted that the measurements of acid strength and/or the number of acid sites for these materials was not performed, therefore it may be that the 5wt% MoO_3/ZrO_2 material contains either the greater number or stronger acid sites, and these are involved in activating methane.

Chapter 6:

CONCLUSIONS

In conclusion, it is evident that solid superacids are able to activate methane under both selective and non-selective reaction conditions. In this respect both the sulfated iron oxides and molybdated materials convert methane to carbon oxides at elevated pressures with only traces of partial oxidation and coupling products, formed at the higher reaction temperatures. However there are differences in the product distributions between the two types of solid acids, which may indicate differences in acid strength but more appropriately differences in their oxidising capabilities. This is not surprising since molybdenum is generally regarded as a selective oxidation material and is included in many partial oxidation catalyst formulations, and iron oxide may be regarded as a complete oxidation material. However, despite this selective products are predominately associated with the modification of iron oxide catalysts

The addition of sulfate to a range of iron oxide precursors was, in general, shown to stabilise specific surface area and to suppress complete oxidation of methane at low reaction temperatures. However at increased temperatures, the activity of the sulfated iron oxides increased and surpassed that of their non-sulfated counterparts. This has been explained as a site blocking phenomenon by the sulfate, which appears to affect the catalytic activity of the iron oxide material. It also, particularly in the case of sulfated iron oxide derived from goethite, produces structural changes, which are related to the original morphology of the precursor. Sulfated iron oxide derived from goethite was shown to display a pitted surface, and an anomalous anisotropic powder x-ray diffraction line broadening effect, which was explained in part by Mossbauer studies as due to cationically disordered environment. Most of the anomalous effect could be attributed to the formation of axial mesoporosity or voids, which modified the crystal Scherrer dimensions. These voids traversed the length of the needle shaped haematite crystals, leading to the possibility of the formation of nanotube type materials via an analogous synthesis procedure. The x-ray line broadening effect was also shown to be calcination temperature dependent, in agreement with literature observations. It was observed that at high calcination temperatures both the relic morphology and the x-ray line broadening effect were lost.

Molybdated materials were observed to produce carbon oxides throughout the temperature range investigated for the partial oxidation of methane. The activity of these materials depended markedly upon the content of molybdate. Optimum catalytic performance was produced by the 5wt% molybdate sample, displaying a non-linear increase in catalytic activity relative to the 2 and 10wt% samples. The enhanced activity of this sample, as well as the general trends between all the molybdated samples, was again demonstrated under ambient pressure and high space velocity conditions for the complete oxidation of methane. Detailed pre- and post-reactor characterisation of these materials indicated no significant structural variations with which the enhanced activity could be associated. Powder x-ray diffraction studies showed an expected increase in the proportion of the metasatble tetragonal phase of the zirconia support with increasing molybdate content. Similarly Raman spectroscopy studies also indicated the presence of poly and bulk molybdate species with increasing molybdate content. However temperature programmed reduction of molybdate materials indicated partial similarities between the 5wt% sample with the 10wt% and 12wt% molybdated zirconia materials. Therefore it was proposed that the enhanced activity observed for the 5wt% sample be attributed to its unique position between the other two samples. In calculating the theoretical coverage of molybdate over the surface of the zirconia it was evident that the 5wt% sample formed monolayer coverage while the other samples formed 50 and 150% monolayer coverage. This model was proposed to account for the enhanced activity observed for this material.

Solid superacids displayed only a degree of catalytic activity when applied to the complete combustion of methane reaction performed at atmospheric pressure and at high space velocities. These materials generally compared less favourably with the traditional iron and copper oxide materials. However, it was observed that the 5wt% sample displayed the highest specific activity among the solid superacids examined, further the activity of this material was also greater than that of the ceria/zirconia materials reported to be active for this reaction. In view of the statement above concerning the oxidising capabilities between the sulfated and molybdated materials this result is unexpected, particularly at the high temperatures employed where the sulfate loss may occur. This clearly demonstrates the enhanced oxidising abilities

which molybdated zirconia materials possess and which is not to date appreciated in the literature, unlike their sulfated metal oxide counterparts.

In conclusion, therefore, it appears that solid acids such as molybdated zirconias and sulfated iron oxides posses oxidising abilities as well as their acknowledged acidic character. However, it is unclear from this study of the role of their apparent strong acidity since it appears that the redox behaviour of these materials is more apparent. Further work is necessary to establish quantitatively the strength and number of acid sites present on both types of solid acids. In this study it is apparent that as well as the unusual catalytic properties of the "superacidic" materials their structural characteristics are also very interesting.

References

1)Gillespie, R.; Peel, T. *Advances in Physical Organic Chemistry* **1972**, *9*, 1.

2)Gilliespie, R. *Accounts in Chemical Research* **1968**, *1*, 202.

3)Olah, G.; Prakash, G.; Sommer, J. *Superacids*; John Wiley and Sons Interscience: New York, 1995.

4)Hino, M.; Arata, K. *Chemistry Letters* **1979**, 1259-1260.

5)Holm, V.; Bailey, G. : US Patent No. 3 032 599, 1962.

6)Arata, K.; Hino, M. *Materials Chemistry and Physics* **1990**, *26*, 213-237.

7)Arata, K. *Applied Catalysis A-General* **1996**, *146*, 3-32.

8)Farcasiu, D. : US, 1983.

9)Hollstein, E.; Wei, J.; Hsu, C. ; Sun Refining Oil Company: US Patent No. 4 918 041, 1990.

10)Hollstein, E.; Wei, J.; Hsu, C.-Y. ; Sun Refining and Marketing Company: US Patent No. 4 956 519, 1990.

11)Yamaguchi, T. *Applied Catalysis* **1990**, *61*, 1-25.

12)Song, X.; Sayari, A. *Catalysis reviews-science and engineering* **1996**, *38*, 329-412.

13)Hino, M.; Arata, K. *Journal of the Chemical Society-Chemical Communications* **1980**, 851.

14)Scurrell, M. S. *Applied Catalysis* **1987**, *34*, 109-117.

15)Srinivasan, R.; Davis, B. H. *Catalysis Letters* **1992**, *14*, 165-170.

16)Bensitel, M.; Saur, O.; Lavalley, J. C.; Morrow, B. A. *Materials Chemistry and Physics* **1988**, *19*, 147-156.

17)Parvulescu, V.; Coman, S.; Grange, P.; Parvelescu, V. I. *Applied Catalysis A-General* **1999**, *176*, 27-43.

18)Jin, T.; Yamaguchi, T.; Tanabe, K. *Journal of Physical Chemistry* **1986**, *90*, 4794-4796.

19)Matsuhashi, H.; Hino, M.; Arata, K. *Applied Catalysis* **1990**, *59*, 205-212.

20)Wang, G. W.; Hattori, H.; Tanabe, K. *Chemistry Letters* **1983**, 277-280.

21)Davis, B. H.; Keogh, R. A.; Srinivasan, R. *Catalysis Today* **1994**, *20*, 219-256.

22)Bensitel, M.; Saur, O.; Lavalley, J. C.; Mabilon, G. *Materials Chemistry and Physics* **1987**, *17*, 249-258.

23)Chen, F. R.; Coudurier, G.; Joly, J. F.; Vedrine, J. C. *Journal of Catalysis* **1993**, *143*, 616-626.

24)Parera, J. M. *Catalysis Today* **1992**, *15*, 481-490.

25)Tatsumi, T.; Matsuhashi, H.; Arata, K. *Bulletin of the Chemical Society of Japan* **1996**, *69*, 1191-1194.

26)Brown, A. S. C.; Hargreaves, J. S. J.; Rijniersce, B. *Catalysis Today* **1998**, *45*, 47-54.

27)Hino, M.; Arata, K. *Journal of the Chemical Society Chemical Communications* **1979**, 1148.

28)Hino, M.; Arata, K. *Catalysis Letters* **1995**, *30*, 25-30.

29)Kousaka, K.; Minato, Y.; Yokoyama, N.; Lida, K.; Imai, T. : EP Patent No. 174 836, 1986.

30)Sohn, J. R.; Kim, H. W. *Journal of Molecular Catalysis* **1989**, *52*, 361-374.

31)Jatia, A.; Chang, C.; Macleod, J. D.; Okubo, T.; Davis, M. E. *Catalysis Letters* **1994**, *25*, 21-28.

32)Tanabe, K.; Yamaguchi, T.; Akiyama, K.; Mitho, A.; Iwabuchi, K.; Isogai, K. *Proceedings on the 8th International Congress on Catalysis* **1984**, *5*, 601.

33)Hammett, P.; Deyrup, A. *Journal of the American Chemical Society* **1932**, *54*, 271.

34)Bensi, H. *Journal of the American Chemical Society* **1956**, *78*, 5490.

35)Corma, A. *Chemical Reviews* **1995**, *95*, 559-614.

36)Hino, M.; Arata, K.; Kobayashi, S. *Journal of the American Chemical society* **1979**, *101*, 6439.

37)Umansky, B.; Engelhardt, J.; Hall, W. K. *Journal of Catalysis* **1991**, *127*, 128-140.

38)Umansky, B. S.; Hall, W. K. *Journal of Catalysis* **1990**, *124*, 97-108.

39)Karge, H. G.; Dondur, V.; Weitkamp, J. *Journal of Physical Chemistry* **1991**, *95*, 283-288.

40)Haller, G. T. *Catalysis Reviews-Science and Engineering* **1981**, *23*, 477-504.

41)Anderson, M. W.; Klinowski, J. *Zeolites* **1986**, *6*, 455-466.

42)Anderson, M. W.; Klinowski, J. *Zeolites* **1986**, *6*, 150-153.

43)Lee, J.; Park, D. *Journal of Catalysis* **1989**, *120*, 46-54.

44)Kustov, L. M.; Kazansky, V. B.; Figueras, F.; Tichit, D. *Journal of Catalysis* **1994**, *150*, 143-149.

45)Lee, J. S.; Yeom, M. H.; Park, D. S. *Journal of Catalysis* **1990**, *126*, 361-369.

46)Adeeva, V.; Dehaan, J. W.; Janchen, J.; Lei, G. D.; Schunemann, V.; Vandeven, L. J. M.; Sachtler, W. M. H.; Vansanten, R. A. *Journal of Catalysis* **1995**, *151*, 364-372.

47)Adeeva, V.; Sachtler, W. M. H. *Applied Catalysis A-General* **1997**, *163*, 237-243.

48)Srinivasan, R.; Keogh, R. A.; Ghenciu, A.; Farcasiu, D.; Davis, B. H. *Journal of Catalysis* **1996**, *158*, 502-510.

49)Tran, M. T.; Gnep, N. S.; Szabo, G.; Guisnet, M. *Applied Catalysis A-General* **1998**, *171*, 207-217.

50)Gao, Z.; Xia, Y. D.; Hua, W. M.; Miao, C. X. *Topics in Catalysis* **1998**, *6*, 101-106.

51)Vera, C. R.; Yori, J. C.; Parera, J. M. *Applied Catalysis A-General* **1998**, *167*, 75-84.

52)Gao, Z.; Chen, J. M.; Hua, W. M.; Tang, Y. *Studies in Surface Science and Catalysis* **1994**, *90*, 507-518.

53)Coelho, M. A.; Resasco, D. E.; Sikabwe, E. C.; White, R. L. *Catalysis Letters* **1995**, *32*, 253-262.

54)Fogash, K. B.; Yaluris, G.; Gonzalez, M. R.; Ouraipryvan, P.; Ward, D. A.; Ko, E. I.; Dumesic, J. A. *Catalysis Letters* **1995**, *32*, 241-251.

55)Gonzalez, M. R.; Kobe, J. M.; Fogash, K. B.; Dumesic, J. A. *Journal of Catalysis* **1996**, *160*, 290-298.

56)Drago, R. S.; Kob, N. *Journal of Physical Chemistry B* **1997**, *101*, 3360-3364.

57)Farcasiu, D.; Ghenciu, A.; Li, J. Q. *Journal of Catalysis* **1996**, *158*, 116-127.

58)Ghenciu, A.; Farcasiu, D. *Journal of Molecular Catalysis A-Chemical* **1996**, *109*, 273-283.

59)Corma, A.; Fornes, V.; Juanrajadell, M. I.; Nieto, J. M. L. *Applied Catalysis A-General* **1994**, *116*, 151-163.

60)Matsuhashi, H.; Motoi, H.; Arata, K. *Catalysis Letters* **1994**, *26*, 325-328.

61)Lin, C. H.; Hsu, C. Y. *Journal of the Chemical Society-Chemical Communications* **1992**, 1479-1480.

62)Hsu, C. Y.; Heimbuch, C. R.; Armes, C. T.; Gates, B. C. *Journal of the Chemical Society-Chemical Communications* **1992**, 1645-1646.

63)Vedrine, J.; Auroux, A.; Bolis, V.; Dejaifve, P.; Naccache, C.; Wierzchowski, P.; Derouane, E.; Hagy, J.; Gilson, J.; Van Hooff, J.; Van den Berge, J.; Wolthuizen, J. *Journal of Catalysis* **1979**, *59*.

64)Coster, D. J.; Bendada, A.; Chen, F. R.; Fripiat, J. J. *Journal of Catalysis* **1993**, *140*, 497-509.

65)Pfeifer, H. *Journal of the Chemical Society-Faraday Transactions I* **1988**, *84*, 3777-3783.

66)Semmer, V.; Batamack, P.; DoremieuxMorin, C.; Fraissard, J. *Topics in Catalysis* **1998**, *6*, 119-125.

67)Haw, J. F.; Chuang, I. S.; Hawkins, B. L.; Maciel, G. E. *Journal of the American Chemical Society* **1983**, *105*, 7206-7207.

68)Lunsford, J. H.; Tutunjian, P. N.; Chu, P. J.; Yeh, E. B.; Zalewski, D. J. *Journal of Physical Chemistry* **1989**, *93*, 2590-2595.

69)Lunsford, J. H.; Sang, H.; Campbell, S. M.; Liang, C. H.; Anthony, R. G. *Catalysis Letters* **1994**, *27*, 305-314.

70)Clearfield, A.; Serrette, G. P. D.; Khazisyed, A. H. *Catalysis Today* **1994**, *20*, 295-312.

71)Riemer, T.; Knozinger, H. *Journal of Physical Chemistry* **1996**, *100*, 6739-6742.

72)Riemer, T.; Spielbauer, D.; Hunger, M.; Mekhemer, G. A. H.; Knozinger, H. *Journal of the Chemical Society-Chemical Communications* **1994**, 1181-1182.

73)Maskikhin, V.; Mudrakovsky, I.; Nosov, A. *Progress In Nuclear Magnetic Resonance Spectrospy* **1991**, *23*, 259.

74)Kayo, A.; Yamaguchi, T.; Tanabe, K. *Journal of Catalysis* **1983**, *83*, 99-106.

75)Babou, F.; Coudurier, G.; Vedrine, J. C. *Journal of Catalysis* **1995**, *152*, 341-349.

76)Nascimento, P.; Akratopoulou, C.; Oszagyan, M.; Coudurier, G.; Travers, C.; Joly, J. F.; Vedrine, J. C.; Hall, W. K.; Wender, I.; Fripat, J. J.; Morterra, C.; Conner, W. C.; Pinna, F.; Hightower, J. W.; Dejong, K. P. *Studies in Surface Science and Catalysis* **1993**, *75*, 1185-1197.

77)Hino, M.; Arata, K. *Journal of the Chemical Society-Chemical Communications* **1988**, 1259-1260.

78)Hino, M.; Arata, K. *Chemistry Letters* **1989**, 971-972.

79)Hino, M.; Arata, K. *Bulletin of the Chemical Society of Japan* **1994**, *67*, 1472-1473.

80)Arata, K.; Nakamura, H.; Nakamura, Y. *Bulletin of the Chemical Society of Japan* **1994**, *67*, 2351-2353.

81)Arena, F.; Giordano, N.; Parmaliana, A. *Journal of Catalysis* **1997**, *167*, 66-76.

82)Cheng, W. H. *Catalysis Letters* **1996**, *36*, 87-93.

83)Banares, M. A.; Alemany, L. J.; Granados, M. L.; Faraldos, M.; Fierro, J. L. G. *Catalysis Today* **1997**, *33*, 73-83.

84)Williams, C. C.; Ekerdt, J. G.; Jehng, J. M.; Hardcastle, F. D.; Wachs, I. E. *Journal of Physical Chemistry* **1991**, *95*, 8791-8797.

85)Machej, T.; Haber, J.; Turek, A. M.; Wachs, I. E. *Applied Catalysis* **1991**, *70*, 115-128.

86)Afanasiev, P.; Geantet, C.; Breysse, M.; Coudurier, G.; Vedrine, J. C. *Journal of the Chemical Society-Faraday Transactions* **1994**, *90*, 193-202.

87)Afanasiev, P. *Materials Chemistry and Physics* **1997**, *47*, 231-238.

88)Zhao, B. Y.; Wang, X. Y.; Ma, H. R.; Tang, Y. Q. *Journal of Molecular Catalysis A-Chemical* **1996**, *108*, 167-174.

89)Schwertmann, U.; Cornell, R. *The Preparation of Iron oxides in the Laboratory*; VCH Weinheim:1991

90)Keenan, M. ; PhD thesis, The Nottingham Trent University: Nottingham, 1997.

91)Twigg, M. *ICI Catalyst Handbook*; 2nd Edition ed.; Wolf Publishing Ltd:.

92)Kotanigawa, T.; Yamamoto, M.; Sasaki, M.; Wang, N.; Nagaishi, H.; Yoshida, T. *Energy & Fuels* **1997**, *11*, 190-193.

93)Yamada, H.; Niwa, M.; Murakami, Y. *Applied Catalysis A-General* **1993**, *96*, 113-123.

94)Anderson, J. R.; Tsai, P. *Journal of the Chemical Society-Chemical Communications* **1987**, 1435-1436.

95)Weckhuysen, B. M.; Wang, D. J.; Rosynek, M. P.; Lunsford, J. H. *Angewandte Chemie-International Edition in English* **1997**, *36*, 2374-2376.

96)Sojka, Z.; Herman, R. G.; Klier, K. *Journal of the Chemical Society-Chemical Communications* **1991**, 185-186.

97)Dowden, D.; Schnell, C.; Walker, G. *Proceedings of the 4th International Congress on Catalysis*, 1968, pp 201-215.

98)Kobayashi, T.; Nakagawa, K.; Tabata, K.; Haruta, M. *Journal of the Chemical Society-Chemical Communications* **1994**, 1609-1610.

99)Otsuka, T.; Komatsu, T.; Jinno, K.; Uragami, Y. *Proceedings of the 9th International Congress on Catalysis*: Calgary, USA, 1988, pp 915-922.

100)Murata, K.; Hayakawa, T.; Fujita, K. I. *Chemical Communications* **1997**, 221-222.

101)Cheung, T. K.; Gates, B. C. *Topics in Catalysis* **1998**, *6*, 41-47.

102)Baldwin, T. R.; Burch, R.; Squire, G. D.; Tsang, S. C. *Applied Catalysis* **1991**, *74*, 137-152.

103)Farcasiu, D.; Li, J. Q. *Applied Catalysis A-General* **1995**, *128*, 97-105.

104)Farcasiu, D.; Li, J. Q.; Cameron, S. *Applied Catalysis A-General* **1997**, *154*, 173-184.

105)Chukhrov, F.; Zvyagin, B. *International Geological Reviews* **1977**, *19*, 873-890.

106)Giovanoli, R.; Brutsch, R. *Chimica* **1974**, *28*, 188-191.

107)Nakajima, K.; Hirotsu, Y.; Okamoto, S. *Journal of the American Ceramic Society* **1987**, *70*, 321-322.

108)Duvigngaud, P.; Derie, R. *Journal of Solid State Chemistry* **1980**, *34*, 323-333.

109)Francombe, M.; Rooksby, H. *Clay and Minerals Bulletin* **1959**, *4*, 1-15.

110)Lima-de-Faria, J. *Zeitschrift Fur Kristallographie* **1963**, *119*, 176-203.

111)Naono, H.; Fujiwara, R. *Journal of Colloid Interface Science* **1980**, *73*, 406-415.

112)Yamaguchi, T.; Takahashi, T. *Journal of the American Ceramic Society* **1982**, *65*, C83.

113)Baker, A. ; BSc Project, Nottingham Trent University: Nottingham, UK, 1997.

114)Nakamoto, K. *Infrared and Raman Spectra of Inorganic and Coordinated Compounds*; Wiley: New York, 1986.

115)Parfitt, R.; Smart, R. S. C. *Soil Science* **1978**, *42*, 48-.

116)Parfitt, R.; Russell, J.; Farmer, V. *Journal of the Chemical Society-Faraday Transactions* **1976**, *72*, 1082.

117)Claridge, J. B.; York, A. P. E.; Brungs, A. J.; MarquezAlvarez, C.; Sloan, J.; Tsang, S. C.; Green, M. L. H. *Journal of Catalysis* **1998**, *180*, 85-100.

118)Ueda, W.; Chen, N. F.; Oshihara, K. *Kinetics and Catalysis* **1999**, *40*, 401-404.

119)Stroud, H. *Improvement In or Relating to the Oxidation of Gases Which Consist Principally of Hydrocarbons*: UK Patent No. 1 398 385, 1975.

120)Liu, R. S.; Iwamoto, M.; Lunsford, J. H. *Journal of the Chemical Society-Chemical Communications* **1982**, 78-79.

121)Liu, H. F.; Liu, R. S.; Liew, K. Y.; Johnson, R. E.; Lunsford, J. H. *Journal of the American Chemical Society* **1984**, *106*, 4117-4121.

122)Khan, M. M.; Somorjai, G. A. *Journal of Catalysis* **1985**, *91*, 263-271.

123)Spencer, N. D.; Pereira, C. J.; Grasselli, R. K. *Journal of Catalysis* **1990**, *126*, 546-554.

124)Coda, E.; Mulhall, E.; Hodnett, B. *Catalysis Today* **1990**, *6*, 559-566.

125)Coda, M. E.; Mulhall, E.; Hodnett, B. *Catalysis Today* **1989**, *4*, 383-387.

126)Banares, M. A.; Pawelec, B.; Fierro, J. L. G. *Zeolites* **1992**, *12*, 882-888.

127)Wada, K.; Yoshida, K.; Watanabe, Y.; Suzuki, T. *Journal of the Chemical Society-Chemical Communications* **1991**, 726-727.

128)Banares, M. A.; Fierro, J. L. G.; Moffat, J. B. *Journal of Catalysis* **1993**, *142*, 406-417.

129)Barbaux, Y.; Elamrani, A. R.; Payen, E.; Gengembre, L.; Bonnelle, J. P.; Grzybowska, B. *Applied Catalysis* **1988**, *44*, 117-132.

130)Hu, H. C.; Wachs, I. E.; Bare, S. R. *Journal of Physical Chemistry* **1995**, *99*, 10897-10910.

131)Conrac, M.; Janin, A.; Lavelly, J. *Infrared Physics* **1984**, *24*, 143.

132)Toraya, H.; Yoshimura, M.; Somiya, S. *Journal of the American Ceramic Society* **1984**, *67*, C183-C184.

133)Toraya, H.; Yoshimura, M.; Somiya, S. *Journal of the American Ceramic Society* **1984**, *67*, C119-C121.

134)Li, P.; Chen, I.; Penner-Hahn, J. *Journal of the American Ceramic Society* **1994**, *77*, 118-128.

135)Garvie, R. *Journal of Physical Chemistry* **1965**, *69*, 1238-1243.

136)Parmaliana, A.; Arena, F.; Frusteri, F.; Martra, G.; Coluccia, S.; Sokolovskii, V. *Studies in Surface Science and Catalysis* **1997**, *110*, 347-356.

137)Smith, M. R.; Zhang, L.; Driscoll, S. A.; Ozkan, U. S. *Catalysis Letters* **1993**, *19*, 1-15.

138)Phillipi, C.; Mazdiyasni, K. *Journal of the American Ceramic Society* **1971**, *54*, 254-258.

139)Chen, Y.; Zhang, L. F. *Catalysis Letters* **1992**, *12*, 51-62.

140)Delarco, M.; Sanfelipe, M. F. M.; Rives, V.; Malet, P.; Ulibarri, M. A. *Journal of Materials Science* **1992**, *27*, 2960-2966.

141)Ismagilov, Z. R.; Kerzhentsev, M. A. *Catalysis Reviews-Science and Engineering* **1990**, *32*, 51-103.

142)Arai, H.; Fukuzawa, H. *Catalysis Today* **1995**, *26*, 217-221.

143)Zwinkels, M. F. M.; Jaras, S. G.; Menon, P. G.; Griffin, T. A. *Catalysis Reviews-Science and Engineering* **1993**, *35*, 319-358.

144)Heland, J.; Schafer, K. *Atmospheric Environment* **1998**, *32*, 3067-3072.

145)Blazowski, W. *Combustion science and Technology* **1975**, *10*, 233-244.

146)Nishind, A. *Catalysis Today* **1991**, *10*, 107-118.

147)Spivey, J. J.; Butt, J. B. *Catalysis Today* **1992**, *11*, 465-500.

148)Butt, J. B.; Spivey, J. J.; Agrawal, S. K. *Studies in Surface Science and Catalysis* **1994**, *88*, 19-31.

149)Pfefferle, L. D.; Pfefferle, W. C. *Catalysis Reviews-Science and Engineering* **1987**, *29*, 219-267.

150)Arai, H.; Machida, M. *Catalysis Today* **1991**, *10*, 81-94.

151)Trimm, D. L. *Applied Catalysis* **1983**, *7*, 249-282.

152)Moro-oka, Y.; Morikawa, Y.; Ozaki, A. *Journal of Catalysis* **1967**, 23-32.

153)Crabtree, R. H. *Chemical Reviews* **1995**, *95*, 2599.

154)Widjaja, H.; Sekizawa, K.; Eguchi, K. *Chemistry Letters* **1998**, 481-482.

155)Omalley, A.; Hodnett, B. K. *Catalysis Today* **1999**, *54*, 31-38.

156)Omalley, A.; Hodnett, B. K. *Studies in Surface Science and Catalysis* **1997**, *110*, 1137-1144.

157)Thormahlen, P.; Skoglundh, M.; Fridell, E.; Andersson, B. *Journal of Catalysis* **1999**, *188*, 300-310.

158)Burch, R.; Urbano, F. J. *Applied Catalysis A-General* **1995**, *124*, 121-138.

159)Baldwin, T. R.; Burch, R. *Applied Catalysis* **1990**, *66*, 359-381.

160)Briot, P.; Auroux, A.; Jones, D.; Primet, M. *Applied Catalysis* **1990**, *59*, 141-152.

161)Hicks, R. F.; Qi, H. H.; Young, M. L.; Lee, R. G. *Journal of Catalysis* **1990**, *122*, 280-294.

162)Briot, P.; Primet, M. *Applied Catalysis* **1991**, *68*, 301-314.

163)Hicks, R. F.; Qi, H. H.; Young, M. L.; Lee, R. G. *Journal of Catalysis* **1990**, *122*, 295-306.

164)Otto, K. *Langmuir* **1989**, *5*, 1364-1369.

165)Baldi, M.; Escribano, V. S.; Amores, J. M. G.; Milella, F.; Busca, G. *Applied Catalysis B-Environmental* **1998**, *17*, L175-L182.

166)McCarty, J.; Wise, H. *Catalysis Today* **1990**, *8*, 231-248.

167)Marion, M. C.; Garbowski, E.; Primet, M. *Journal of the Chemical Society-Faraday Transactions* **1991**, *87*, 1795-1800.

168)Trovarelli, A.; deLeitenburg, C.; Boaro, M.; Dolcetti, G. *Catalysis Today* **1999**, *50*, 353-367.

169)Jang, B. W. L.; Nelson, R. M.; Spivey, J. J.; Ocal, M.; Oukaci, R.; Marcelin, G. *Catalysis Today* **1999**, *47*, 103-113.

170)Keshavaraja, A.; Ramaswamy, A. V. *Chemical Communications* **1996**, 397-398.

171)Keshavaraja, A.; Ramaswamy, A. V. *Applied Catalysis B-Environmental* **1996**, *8*, L1-L7.

172)Liu, W.; Flytzanistephanopoulos, M. *Journal of Catalysis* **1995**, *153*, 304-316.

173)Li, P.; Chen, I. W.; Pennerhahn, J. E. *Journal of the American Ceramic Society* **1994**, *77*, 118-128.

174)Li, P.; Chen, I. W. *Journal of the American Ceramic Society* **1994**, *77*, 1281-1288.

175)Claudell, B.; Brau, G. *Journal of Catalysis* **1969**, *14*, 322-331.

176)Groppi, G.; Bellotto, M.; Cristiani, C.; Forzatti, P.; Villa, P. L. *Applied Catalysis A-General* **1993**, *104*, 101-108.

177)Machida, M.; Eguchi, K.; Arai, H. *Journal of Catalysis* **1989**, *120*, 377-386.

178)Machida, M.; Eguchi, K.; Arai, H. *Journal of Catalysis* **1990**, *123*, 477-485.

179)Yan, L. C.; Thompson, L. T. *Applied Catalysis A-General* **1998**, *171*, 219-228.

180)Shimizu, T. *Catalysis Reviews-Science and Engineering* **1992**, *34*, 355-371.

181)Nagamoto, H.; Amanuma, K.; Nobutomo, H.; Inoue, H. *Chemistry Letters* **1988**, 237-240.

182)Seiyama, T. *Catalysis Reviews-Science and Engineering* **1992**, *34*, 281-300.

183)Arai, H.; Yamada, T.; Eguchi, K.; Seiyama, T. *Applied Catalysis* **1986**, *26*, 265-276.

184)Hua, W. M.; Gao, Z. *Applied Catalysis B-Environmental* **1998**, *17*, 37-42.

185)Rezgui, S.; Liang, A.; Cheung, T. K.; Gates, B. C. *Catalysis Letters* **1998**, *53*, 1-2.

186)Weckhuysen, B. M.; Wang, D. J.; Rosynek, M. P.; Lunsford, J. H. *Journal of Catalysis* **1998**, *175*, 347-351.

187)Wilson, K.; Hardacre, C.; Lambert, R. M. *Journal of Physical Chemistry* **1995**, *99*, 13755-13758.

188)Brown, A.S.C.; Hargreaves, J.S.J. *Green Chemistry* **1999**, 1 17-20

189)Lin, C.H.; Wan, B.Z., *Journal of the Chinese Chemical Society*, **1993**, 24, 71-78.

190)Akoi, K.; Ohmae, M.; Nanba, T; Takeishi, K.; Azuma, N.; Ueno, A.; Ohfune, H.; Hayashi, H,; and Udagawa, Y. *Catalysis Letters*, **1998**, 45, 29-33.

191)Herman, R.G.; Sun, Q.; Shi, C.L.; Klier, K.; Wang, C.B.; Hu, H.C; Wachs, I.E.; and Bhasin, M.M. *Catalysis Today*, **1997**, 37, 1-14.

192) Suzuki, K.; Hayakawa, T.; Shimizu, M.; and Takehira, K. *Catalysis Letters*, 1995, 30, 159-169.

193)Matsumura, Y and Moffat, J. B. *Journal of Catalysis*, **1994**, 148, 232-333.

194)Figrro, G.; Jalono, M.L.; Inversi, M.; Moretti, G.; Porta, P. and Lavecchita, R. *Proceedings of the 10th International Congress on Catalysis*, 1992, 1847-1850.

Appendix 1: Equations for the calculation of activity data

$$\% \text{ Methane Conversion} = \frac{\sum_n C_n}{CH_{4(IN)}} \times 100$$

$$\% \text{ Oxygen Conversion} = \frac{O_{2(IN)} - O_{2(OUT)}}{O_{2(IN)}} \times 100$$

$$\% \text{ Selectivity} = \frac{nC_n}{\sum_n C_n} \times 100$$

$$\% \text{ Carbon Balance} = \frac{\sum_n C_n + CH_{4(OUT)}}{CH_{4(IN)}} \times 100$$

$$\% \text{ Oxygen demand} = \frac{O_{2(OUT)} + \sum_i O_i}{O_{2(IN)}} \times 100$$

$$\text{Specific} = \frac{(\text{Total flow rate} \times \%CH_{4(IN)}) \times (\%CH_4 \text{ conversion})}{(2.24 \times 10^4) \times (\text{mass of sample in the reactor/g}) \times (\text{surface area } m^2/g)}$$

$$\text{Per Pass Yield} = \frac{(\% \text{ Selectivity to selected product}) \times (\% \text{ methane conversion})}{100}$$

Where, n = Number of carbon molecules in the product molecule,

C = Carbon containing products.

(IN) = mole % of methane, or oxygen entering reactor.

(OUT) = mole % of methane, or oxygen exiting reactor.

I = mole % of oxygen molecules consumed for the formation of the desired oxygen containing product according to its stoichiometric equations.

Appendix 2: HRTEM of goethite precursor prior to sulfation and calcination at 350C

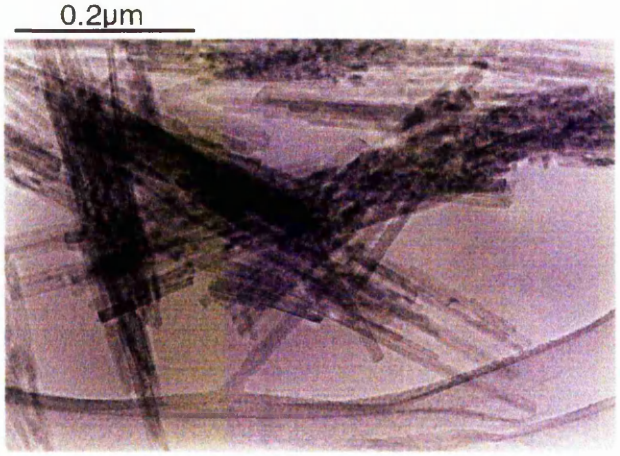

Appendix 3: STEM EDX compositional mapping of goethite derived iron oxides calcined at 350C

Sulfated iron oxide

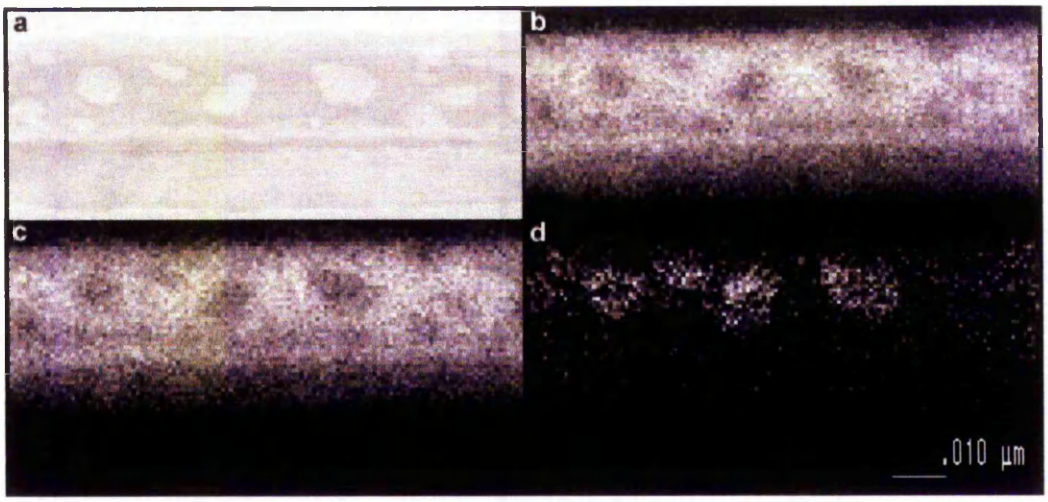

a) STEM image of sulfated iron oxide derived from goethite, b) Elemental mapping of iron, c) Elemental mapping of oxygen and d) Elemental mapping of sulfur associated with pores.

Non-sulfated iron oxide

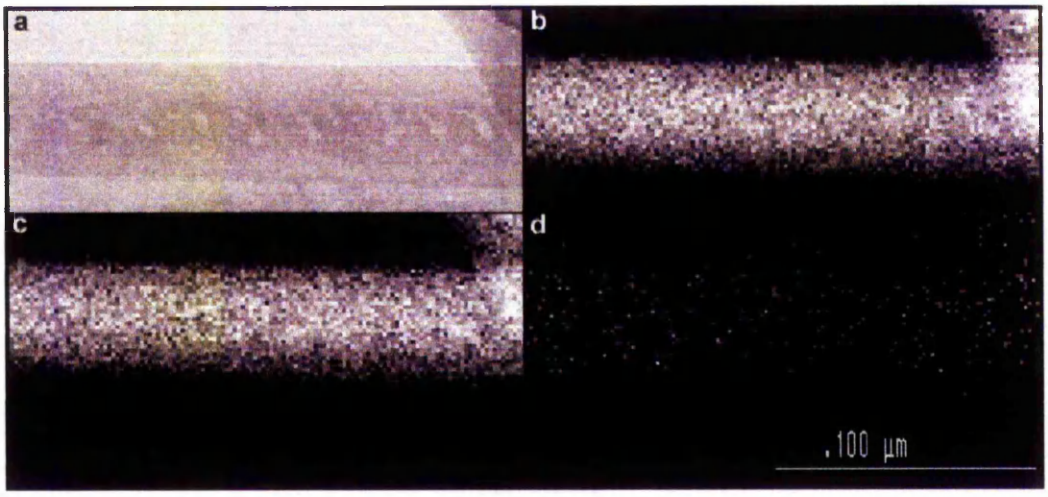

a) STEM image of non-sulfated iron oxide derived from goethite, b) Elemental mapping of iron, c) Elemental mapping of oxygen and d) Elemental mapping of sulfur

Last Page